Geomechanical modelling of CO_2 injection in deep aquifers

THÈSE N^{O} 6979 (2016)

PRÉSENTÉE LE 2 MAI 2016

À LA FACULTÉ DE L'ENVIRONNEMENT NATUREL, ARCHITECTURAL ET CONSTRUIT
LABORATOIRE DE MÉCANIQUE DES SOLS - CHAIRE GAZ NATUREL PETROSVIBRI
PROGRAMME DOCTORAL EN MÉCANIQUE

ÉCOLE POLYTECHNIQUE FÉDÉRALE DE LAUSANNE

POUR L'OBTENTION DU GRADE DE DOCTEUR ÈS SCIENCES

PAR

Chao LI

acceptée sur proposition du jury:

Prof. C. Ancey, président du jury
Prof. L. Laloui, directeur de thèse
Dr G. Siddiqi, rapporteur
Prof. A. Bonneville, rapporteur
Prof. B. Lecampion, rapporteur

ÉCOLE POLYTECHNIQUE
FÉDÉRALE DE LAUSANNE

Suisse
2016

致父母

ACKNOWLEDGEMENTS

I would like to express my sincere gratitude to my thesis supervisor, Prof. Lyesse Laloui, for his unconditional support and guidance during my PhD. His affirmative professional attitude and dedication to science were an inspiration and an encouragement for me to accomplish my thesis. Beyond all his contribution to my work, I am very grateful for the numerous opportunities that he provided me to be active in international research events and various professional activities. Experience gained from those activities are invaluable to me. Un grand merci, Lyesse!

I would like to thank the other members of my PhD committee, Prof. Alain Bonneville, Dr. Gunter Siddiqui, Prof. Brice Lecampion and Prof. Christophe Ancey for accepting to review this thesis.

I would like to acknowledge the LAGAMINE team from the University of Liège, in particular, Prof. Frederic Collin and Jean-Pol Radu for their great support on the code. My very special thanks to Anne-Catherine Dieudonné for sharing her knowledge on the implementation and utilisation of the code. I always enjoy fruitful discussions with her and her big smile. Thanks also go to Benjamin Cerfontaine and Prof. Pierre Gerard for the exchange of ideas.

I am deeply thankful to Prof. A.P.S. Selvadurai from McGill University, Prof. David Andrew Barry at EPFL and Dr. Laurent Tacher at LMS for their comments and suggestions on the analytical development. I am also grateful to Dr. Bahman Bohloli from NGI to provide me several resources related to the In Salah Project.

A number of people have also direct or indirect contributions on my thesis. Many thanks go to the master students for their excellent diploma works: Paul Barès for his exceptional mathematic contribution on the analytical solutions, De Oliveira Frederico Caldas and Abdelhak Nicolas for the hard work on thermo-hydro-mechanical modelling, and Guillaume Robert for his intelligence in the chemo-hydro-mechanical development. I am very grateful to Yafei Qiao who helped me a lot at the end of my thesis.

I would like to thank a lot former and current members at the formidable LMS for all the happiness that we shared together during this wonderful four years: Grazie ad Alice for her essential support. Grazie di cuore a Alberto for his great heart. Grazie ad Francesco for his enthusiasm in Asian culture and talks about life. Grazie a Valentina for the trips that we shared together and for running with me. Grazie ad Donatella to encourage me to drink, Grazie ab Alessandro for his help at several occasions. Merci mille fois à Fabrice pour m'avoir donné beaucoup de conseils au début de la thèse. Merci à très-cool Timur pour les moments ensemble dans le bureau. Grazie ad Alessio for the co-authorship with his great attention to detail. Un grand merci à Samuel pour ses excellents fromages qui m'a ajouté la force de rédaction. A big thank-you to: Suzanne, John, Dimitrios, Etienne, Eleonora, Giovanni, Samila, Maria, Sergio, Ali, Abdusalam, Thomas, Qazim, Gilbert, Georg, Danila, Roman and Victor. I would like to thank as well all LMR people, in particular, Zou Yang, Zhang Qianbing, Laurent, Erica, Andrea and Prof. Jian Zhao. Thanks go to Felipe and Prof. Marie Violay at LEMR and Fatima and Prof. Brice Lecampion at GEL.

Un remerciement particulier est adressé à Patrick pour son aide et ses conseils pour ma vie quotidienne. Je voudrai aussi remercier à Rosa-Ana, Barbara, Jessica et Michela pour m'avoir facilité beaucoup les procédures administratives. Merci également Nicolas et Stefano pour leur support informatique.

I would like to thank Qiao Yafei, Wang Deqi, Zou Yang, Zhang Qianbing, Jiang Lingqing, Kong Gangqiang, Chen Liang, Chen Zhongheng, Nancy, Scout, Dandan, Wang Zexi, Zhenzhu, Chen Jun and many others who made my life easier and happier in Lausanne and Zurich.

My deep indebtedness is given to my parents, grandparents and the family of my uncle, especially my little cousin, for the encouragement and unconditional support.

Last but not least, a heartfelt thanks goes out to Fei for supporting this work along this four years with your patience and endless love.

ABSTRACT

CO_2 sequestration in deep geological formations is considered as a promising technology to reduce the impact of CO_2 on the greenhouse effect. Practically, large-volume of CO_2 could be injected into a system that consists of a highly porous host reservoir covered by a low permeable sealing caprock. High rate injection could result in an abrupt fluid pressures build-up, deforming the aquifer and compromising the integrity of the caprock. The interaction between the high-pressure injected CO_2 and the host reservoir as well as the cap rock gives rise to a complex engineering system. A good understanding of this coupled interaction is a crucial issue to secure the underground CO_2 injection. This thesis is primarily motivated by such need, and the objectives of the present manuscript are to understand and predict the multiphase flow and thermo-hydro-mechanical processes arising from CO_2 injection into deep aquifers and to develop and evaluate both analytical and numerical modelling concepts as reliable prediction and risk assessment tools.

For the analysis of CO_2 injection-induced deformation of the aquifer, a hydromechanical continuum modelling approach is proposed together with a generalised effective stress concept and an elastoplastic description of mechanical rock behaviour. A deep conceptual aquifer is built, and numerical simulations are run to analyses the effects of hydromechanical couplings and injection strategies on the mechanical stability of the aquifer. The results reveal that upon injection geomechanical instabilities originate from the fluid pressure accumulation within the aquifer, and the most important hydromechanical processes occur in the vicinity of the injection well, compromising the caprock integrity. Low-rate injection significantly reduces the fluid pressure accumulation within the aquifer. However, progressively increasing the injection rate to the target value cannot limit the overpressure development significantly.

The temperature of injected CO_2 is usually lower than the in-situ temperature, providing additional complexity to the hydromechanical coupling. The hydromechanical framework is extended to include multiphase thermo-hydro-mechanical effects. Numerical simulations are carried out with a finite element reservoir model that is built upon available experimental data and real log data for the CO_2 storage site at In Salah, Algeria over an injection period of four and a half years. The blind prediction performed by the fully coupled simulation is in excellent accordance with the real-time monitoring of the surface uplift at In Salah.

With an investigation into the experimental evidence, the present work that formulates an extensive parametric fully coupled thermo-hydro-mechanical study complement previous studies. It extends them in a range of conditions where the coupled parameters and heat transfer parameters are substantially valid in practice. A ratio of coupled parameters set

(Young's modulus, Poisson's ratio and thermal expansion coefficient) between caprock and aquifer is defined and devoted to an indication of the caprock failure potential. The results show in particular that the consideration of the aquifer's Biot coefficient is essential to properly estimate the expansion of the aquifer.

A coupled analytical approach is also developed to determine the temporal and spatial evolution of caprock deformation and surface uplift when subjected to CO_2 injection. Analytical resolution of the plate theory with the abrupt interface theory led to two closed-form analytical solutions that are validated against both in-situ monitoring data at In Salah and finite element modelling results. By incorporating elastic properties of the reservoir system and the real thermodynamic properties of CO_2 and brine, the temporal and spatial evolution of caprock deformation and surface uplift can be obtained readily. Furthermore, the use of two solutions allow to efficiently assess uncertainty in key parameters for a CO_2 storage project such as the injection rate, porosity, rock properties and geological structures. This development allows to incorporate any fluid injection-induced pressurisation distribution functions in a straightforward way. Thus, advances in hydrogeology research can be integrated easily, and the current development can be extended to any fluid injection and extraction problem. The proposed approach offers a practical solution for determination of caprock and surface deformation, candidate site evaluation and sensitivity analysis of essential parameters. Two solutions can be considered as one of most efficient and accurate design tool for estimating the influence of high injection rates of CO_2 on surface uplift and caprock deformation, which account for the hydraulic and mechanical properties of the reservoir and real CO_2 properties.

Keywords: CO_2 injection, thermo-hydro-mechanical modelling, reservoir stability, caprock integrity, aquifer expansion, finite element method, analytical development

RÉSUMÉ

La séquestration de CO_2 dans des formations géologiques profondes est une technologie prometteuse afin de réduire les émissions de gaz à effet de serre. En pratique, de larges volumes de CO_2 seraient injectés dans un système composé d'une roche réservoir très poreuse et d'une couverture peu perméable. Cependant, si le débit d'injection est trop élevé, l'injection peut engendrer une importante montée en pression, déformant ainsi l'aquifère et compromettant l'intégrité de la couverture. L'interaction entre le CO_2 injecté à haute pression, le réservoir et la couverture forme un système très complexe. Une bonne compréhension des différents phénomènes couplés est un enjeu majeur afin de garantir le stockage du CO_2. Les objectifs de cette thèse sont ainsi de comprendre et prédire les écoulements multiphasiques et les processus thermo-hydro-mécaniques liés à l'injection de CO_2 dans des aquifères profonds, et de développer et évaluer des outils de modélisation, à la fois analytiques et numériques, pouvant être utilisés comme outils de prédiction et d'évaluation des risques.

Pour l'analyse des déformations de l'aquifère induites par l'injection de CO_2, une approche de modélisation hydromécanique continue est proposée. Le concept de contrainte effective généralisée et une description élastoplastique de la roche sont utilisés. Un modèle idéalisé d'aquifère profond est construit, et des simulations numériques sont réalisées afin d'analyser les effets des couplages hydromécaniques et de différentes stratégies d'injection sur la stabilité mécanique de l'aquifère. Les résultats montrent que, pendant l'injection, les instabilités géomécaniques sont liées à l'accumulation des pressions de fluide dans l'aquifère. Ces processus sont particulièrement importants à proximité du puits d'injection et compromettent l'intégrité de la roche de couverture. Une injection à plus faible débit réduit l'accumulation des pressions de fluide dans l'aquifère. Cependant, l'augmentation progressive du débit d'injection à la valeur cible ne permet pas de limiter de manière significative le développement des surpressions.

La température du CO_2 injecté est généralement inférieure à la température in-situ, augmentant la complexité des couplages hydromécaniques. Le modèle hydromécanique est étendu pour prendre en compte les effets thermo-hydro-mécaniques. Des simulations numériques éléments finis sont réalisées sur un modèle 2D de réservoir. Le réservoir est construit sur base de données expérimentales disponibles et des données de log provenant du site de stockage de CO_2 de In Salah en Algérie. L'injection de CO_2 est modélisée pendant 4 ans. Les prédictions à l'aveugle réalisées montrent une excellence concordance avec le monitoring continu des mouvements de terrain à la surface.

Sur base d'une analyse des observations expérimentales, ce travail propose une large étude paramétrique du comportement couplé thermo-hydro-mécanique d'un site de stockage. Il

complète les études précédentes en étudiant une gamme de paramètres couplés et de transfert de chaleur correspondant à différentes conditions de réservoir rencontrées en pratique. Un rapport de paramètres (module de Young, coefficient de Poisson et coefficient de dilatation thermique) entre la couverture et l'aquifère est défini et utilisé comme un indicateur du potentiel de rupture de la couverture. Les résultats montrent que la prise en compte du coefficient de Biot de l'aquifère est essentielle pour estimer de manière correcte les déformations de l'aquifère.

Une approche analytique couplée est également développée pour déterminer l'évolution temporelle est spatiale des déformations de la roche de couverture et des mouvements à la surface pendant l'injection de CO_2. La résolution de la théorie des plaques avec une interface nette mène à des solutions analytiques qui sont validées sur des données de monitoring in-situ de In Salah et des résultats de modélisations éléments finis. En introduisant les propriétés élastiques du système réservoir et les propriétés thermodynamiques réelle du CO_2 et de la saumure, l'évolution temporelle et spatiale de la déformation de la couverture et des mouvements de surface peuvent être obtenus. Par ailleurs, l'utilisation de deux solutions permet d'évaluer efficacement l'incertitude sur les paramètres clés d'un projet de stockage de CO_2 tels que le débit d'injection, la porosité, les propriétés des roches et les structures géologiques. Ce développement permet d'incorporer différentes fonctions de distribution des pressions induites par l'injection de fluide. Des avancées dans le domaine de l'hydrogéologie peuvent donc être facilement intégrées, et le présent développement peut être étendu à d'autres problèmes d'injection ou d'extraction de fluides. La présente approche offre une solution pratique pour la détermination des déformations de la couverture et de la surface, l'évaluation de sites potentiels et l'étude de sensibilité des paramètres essentiels. Deux solutions peuvent être considérées comme un des outils les plus efficaces et précis pour l'estimation de l'influence de débits d'injections de CO_2 élevés sur les mouvements de surface et la déformation de la couverture, en prenant en compte les propriétés hydrauliques et mécaniques du réservoir et les propriétés réelles du CO_2.

Mots-clés : injection de CO_2, modélisation thermo-hydro-mécanique, stabilité du réservoir, intégrité de la couverture, méthode éléments finis, développement analytique

TABLE OF CONTENTS

LIST OF SYMBOLS

Greek symbols

α	Phase index, c = CO_2 and w = brine
α, κ	Peng and Robinson EOS parameters
α_s	Linear thermal expansion coefficient
β_w	Volumetric thermal expansion coefficient of water
ε_d	Deviatoric strain
ε_v	Volumetric strain
ε_d^e	Elastic deviatoric strain
ε_v^e	Elastic volumetric strain
ε_v^p	Volumetric plastic strain
ε_d^p	Deviatoric plastic strain
$\varepsilon_v^{p,iso}$	Volumetric plastic strain due to the isotropic mechanism
$\boldsymbol{\varepsilon}$	Total strain tensor
$\boldsymbol{\varepsilon}^e$	Elastic strain tensor
$\boldsymbol{\varepsilon}^p$	Plastic strain tensor
ζ	Interface position from the bottom of the aquifer
η	Kozeny-Carman relationship parameter
κ_T	Isothermal water compressibility
λ	Plastic multiplier
λ	Thermal conductivity of porous medium
λ_m	Thermal conductivity of saturated medium

λ_s	Thermal conductivity of solid particle
λ_w	Thermal conductivity of water
λ_c	Thermal conductivity of CO2
μ_c	Dynamic viscosity of CO2
μ_w	Dynamic viscosity of water
μ_{JT}	Joule-Thomson coefficient
v	Poisson's ratio
v_s	Storage unit Poisson's ratio
v_c	Caprock Poisson's ratio
v_o	Overburden unit Poisson's ratio
ξ	Real number-associated Bessel integral used in the Hankel transformation
ρ	Radius used in Green's function
ρ	Mass density of the mixture (solid, water/brine and CO2)
ρ_s	Mass density of the solid particles
ρ_w	Mass density of water/brine
ρ_c	Mass density of CO2
ρ_{dc}	Mass density of dissolved CO_2 in brine
σ_h'	Horizontal effective stress
σ_v'	Vertical effective stress
σ_n'	Normal effective stress
σ_1'	Maximum principal effective stress
σ_3'	Minimum principal effective stress
$\boldsymbol{\sigma}$	Total stress tensor

σ'	Effective stress tensor
τ	Tortuosity of the porous media
τ	Shear stress
τ	inverse reduced temperature
τ_{max}	Current maximum shear stress
$\tau_{threshold}$	Threshold shear stress
ϕ	Porosity
ϕ^0	Dimensionless Helmholtz energy for ideal CO2
ϕ_c	Friction angle
Φ	Material property constant of the medium
Φ	CO_2 fugacity
ψ	Dilatancy angle
Ω	Material property constant of the medium

Roman symbols

a,b	Peng and Robinson EOS parameters
b	Biot coefficient
c	Cohesion
c_p	Specific saturated heat capacity of caprock
$c_{p,c}$	Specific heat capacity of CO2
$c_{p,w}$	Specific heat capacity of water
$c_{p,s}$	Specific heat capacity of solid
$c_{p,ideal}$	Specific heat capacity of an ideal CO2

CKA1	CO_2 relative permeability curve parameter
CKA2	CO_2 relative permeability curve parameter
CKW	Water relative permeability curve parameter
CKC	CO_2 relative permeability curve parameter
d	Depth used in Green's function
D	Flexural rigidity of the embedded caprock
D	Thermal diffusivity of caprock
E	Young's modulus
E_c	Young's modulus of caprock
E_a	Young's modulus of aquifer
$\mathbf{E}$	Elastic compliance tensor of rank 4
f	Yield function of Drücker Prager model
$f_{co2\text{-}w}$	CO_2 dissolution rate in water
$f_{w\text{-}co2}$	CO_2 degassing rate from water
Fs	local failure indicator
$\boldsymbol{g}$	Gravity acceleration
g	Plastic potential
G_s	Storage unit shear modulus
G_c	Caprock shear modulus
G_o	Overburden unit shear modulus
h	Thickness of the caprock
h_c	Specific enthalpy of CO2
H	Enthalpy of system

H_m	Enthalpy of the porous medium
H_{ideal}	Enthalpy of ideal CO_2
I	Unit tensor
$\mathbf{i}_{dc}$	Diffusion velocity
I_σ	First invariants of effective stress tenor
II_σ	Second invariants of deviatoric stress tensor
J_n	Bessel function of the first kind of order *n*
k	Intrinsic isotropic permeability tensor
k	Isotropic intrinsic permeability
k_0	Initial isotropic intrinsic permeability
k_{rc}	Relative permeability of the water phase
k_{rw}	Relative permeability of the water phase
$K_{eq,g-l}^{CO_2}$	Henry's coefficient
K	Drücker Prager model constant
K_s	Bulk modulus of the solid particles
K_0	Initial effective stress factor
l	Distance from the caprock to the middle of the injection zone
m	Aquifer (injection zone) thickness
m	Van Genuchten water retention curve parameter
M, M'	Drücker Prager model constant
M_c	Molar mass of CO_2
M_w	Molar mass of water
n	Porosity

n_0	Initial porosity
p'	Mean effective stress
p_c	CO_2 pressure
P_c	Critical pressure of CO2
p_w	Water pressure
p_f	Averaged fluid pressure
P_r	Van Genuchten water retention curve parameter
q	Deviatoric stress
$q^{(s)}$	Contact stress between the caprock and storage unit
$q^{(o)}$	Contact stress between the caprock and overburden unit
$\mathbf{q}_w$	Relative water phase velocity with respect to the solid phase
$\mathbf{q}_c$	Relative CO_2 phase velocity with respect to the solid phase
Q_m	CO_2 mass flow rate
Q_0	CO_2 volumetric flow rate
w	Deflection
Δp	Fluid overpressure
$\overline{\Delta p}$	Fluid overpressure density after the Hankel transformation
r	Radial distance in the polar coordinate
r_0	CO_2 plume radius at the top of the aquifer
r_b	CO_2 plume radius at the base of the aquifer
r_w	Injection well radius
R	Radius of influence
R	Universal gas constant

R	Elastic properties ratio between caprock and aquifer
s	Suction/capillary pressure
S	Entropy of system
S_s	Specific storage coefficient
S_w	Water saturation
t	Time
T	Temperature
T_0	Temperature
T_c	Critical temperature of CO2
T_{int}	Temperature at the interface aquifer-caprock
U	Internal energy of system
$u_z^{(s)p}$	Displacement solely due to an overpressure generation
$u_z^{(s)q}$	Displacement solely due to contact stress between the caprock and storage unit
$u_z^{(o)q}$	Displacement solely due to contact stress between the caprock and overburden unit
u_r	Radial displacement at the caprock-storage interface
u	Displacement vector
$V(t)$	CO_2 plume volume
V	Elementary volume
X_{dc}	Mass fraction of dissolved CO2 in water
Z	Compressibility factor
z	Vertical coordinate
NB	Nordbotten et al. [16] approach

DZ	Dentz and Tartakovsky [17] approach
LI-SN	developed Li-Selvadurai-Nordbotten solution
LI-SD	developed Li-Selvadurai-Dentz solution

Operators

d (.)	Increment
div (.)	Divergence
$\bar{f}$	Zeroth-order Hankel transform of function f
erfc (.)	Complementary error function
sh (.)	Hyperbolic sinus
δij	Kronecker delta
∂	Partial derivative
d	Total derivative
Δ	Variation
∇	Gradient
∇^2	Laplace operator
exp	Natural exponent
Σ	Sum
tr	Trace of a tensor
ln	Natural logarithm
log	Logarithm base 10

1 Introduction

1.1 Carbon capture and storage

In the last two centuries, human activities have released a large amount of CO_2 (carbon dioxide) into the atmosphere. Even though the public awareness and the investments from numerous countries have been increasing concerning renewable energies, fossil fuels are and still be in a near future the main source of energy due to its cheapness, abundance and global distribution. Furthermore, since the Fukushima accident in 2011, several governments around the world, including the Swiss Federal Government, have decided to make a progressive move out of nuclear energy that presents 40% of electricity production in Switzerland over the last decade (Office fédéral de L'énergie, 2015). Switzerland has decided to close all the Nuclear Power Plants in the next 20 to 30 years. To compensate this decrease of energy production, the Swiss Federal government has decided to develop alternative environmental friendly energy. However, Rome was not built in one day. It will take time to be able to produce as much energy as needed for the 'green energy'. In the meantime, the energy supply would still highly rely on the combustion of traditional energy material. Due to this, there will be a period where natural gas combustion will contribute a vital share of Swiss electric production. The increase in the emission of greenhouse effect gases (composed mainly of CO_2) might have severe economic consequences due to the international protocol ascribed by the Swiss Government. In this context, the need for mitigation technologies to reduce CO_2 emissions becomes urgent and necessary.

Among the several measures for reduction of carbon dioxide emissions, Carbon Capture and Storage (CCS) is one of the latest solutions available to reduce the CO_2 in the atmosphere (IEA/OECD, 1994). CCS briefly consists in the separation and capture of CO_2 from point sources by the diffuse removal from the atmosphere or stationary sources (e.g. power plants, cement factory). Then CO_2 is transported and sequestered away from the atmosphere for long periods of time, in the order of centuries to millennia and up to millions of years (Metz et al., 2005). Geological sequestration of CO_2 is currently and probably the best and only option in the short-medium term for significantly reducing CO_2 concentrations. The reason is that fluid storage in geological formations is common phenomena such as natural accumulation of oil, gas and even CO_2. This natural process provides confidence in long-term storage of CO_2 (Bradshaw and Dance, 2005). The CCS has the advantage of rapid implementation due to extensive experience developed over the years by the oil and gas industries.

1.2 Principles of CO_2 geological sequestration

Sedimentary basins that host oil or gas reservoirs, abandoned coal seams and deep saline aquifers are proven appropriate for CO_2 sequestration (Benson and Cole, 2008; Kharaka et al., 2006; Michael et al., 2010). Regarding the high rate supply of CO_2 from power generators, a large storage capacity and a reasonable injectivity are crucial to ensure the need at the industrial level. Deep saline aquifers among the three potential geological formations represent the most voluminous geological formation for hosting CO_2 (Bachu and Adams, 2003; Bachu, 2000). A recent study also demonstrates that saline aquifers are the only geological formation where CO_2 could be conceivably and viably stored in Switzerland, and the storage capacity of saline aquifers allows to accept the intended volume at industrial scale (Chevalier et al., 2010).

Deep saline aquifers are the most common fluid reservoirs in the subsurface of the world, of which the saline formation water (also called *brine*) is no longer potable to humans due to its high salinity. Aquifers of interest are those around 800 to 1000 meters underground, where the pre-injection pore pressure is usually higher than 10MPa, and the corresponding in-situ temperature is greater than 40°C (considering a hydrostatic pressure gradient of 10MPa per km depth and a geothermal gradient of 30°C with a surface temperature of 10°C). Under such environmental condition, CO_2 is at supercritical state with a liquid-like density of about 700kg/m^3 and a gas-like viscosity of 0.5×10^{-4} Pa.s. Both attributes make the injection in deep aquifers more advantageous such that more mass can be injected for a given volume and high "mobility" of CO_2 to aid rapid migration away from injection wells. Despite its high density, CO_2 at supercritical state is still less dense than the brine in the aquifer. This density difference creates a buoyancy effect which is the reason that the injected CO_2 conceptually accumulates on top of the brine and forms a plume-like migration pattern as illustrated in Figure 1.1.

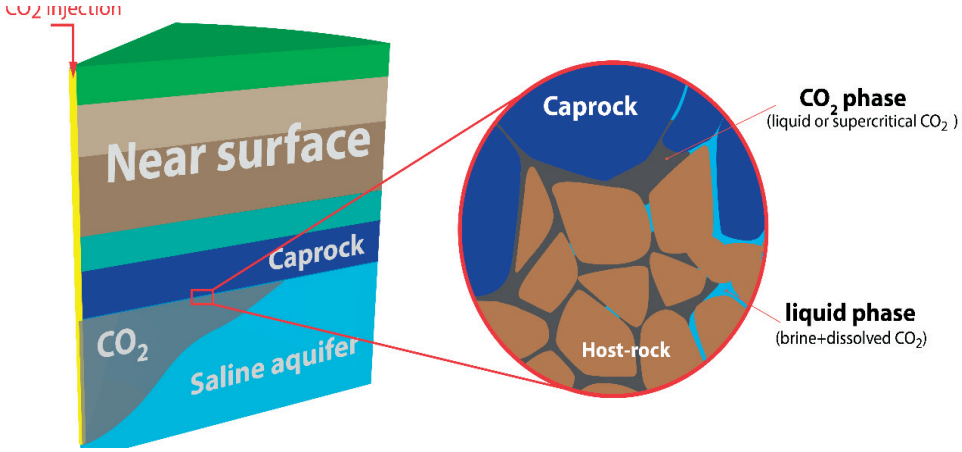

Figure 1.1 Schematic illustration of CO_2 injection into a deep saline aquifer

Figure 1.1 also shows a must-have aquifer-seal pair as a viable and secure CCS geological site. The aquifer is a highly permeable reservoir rock to permit rapid CO_2 inflow, together with large porosity to offer enough storage capacity, and is overlain by a sufficiently low permeable sealing caprock. The caprock provides a primary physical barrier to prevent the migration and leakage of the buoyant and low viscosity CO_2 from the storage location to other places in the subsurface or even to shallow potable groundwater levels. From a conceptual point, permeable fault zones and seismogenic zones are to be avoided to minimise the leakage risk and to reduce injection inducing seismic events.

1.3 Trapping mechanisms and associated coupling effects

The storage of CO_2 in deep saline aquifers occurs through a combination of various trapping mechanisms. These entrapment phenomena can be of a chemical or physical nature and depend on the storage site in question, are illustrated together in Figure 1.2 with associated coupling effects over time.

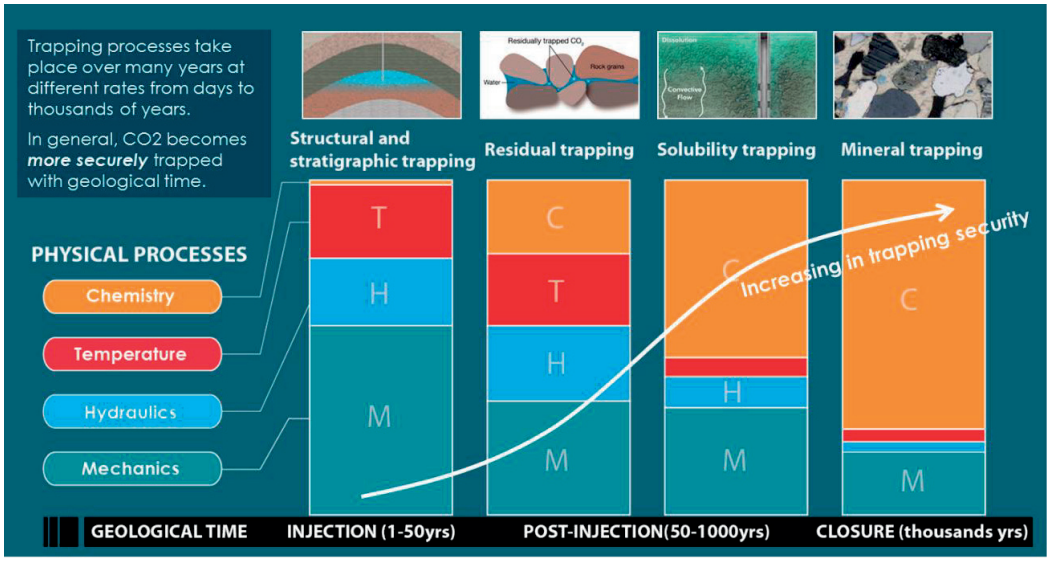

Figure 1.2 Temporal evolution of trapping mechanisms and associated coupling effects

In oil reservoirs and saline aquifers, the operating mechanisms are very similar, the main trapping mechanism being the structural/stratigraphic confinement where CO_2 is prevented from leaking by physical barriers (less permeable caprock and impermeable faults) during the injection stage. During this period, CO_2 displaces the formation water (hydraulic two-phase flow), pressurises the reservoir and induces expansion of aquifer and surface uplift (hydro-mechanical coupling). Also, injection temperature is usually lower than the in-situ temperature. Cooling leads to contraction (thermo-mechanical coupling) in the near-well field, being an additional complexity (Birkholzer et al., 2015). The dominant process in the first years of injection is thus two-phase flow coupled with pressurised expansion and cooling contraction, constituting a thermo-hydro-mechanical (THM) processes .

During the two-phase flow, CO_2 as a non-wetting phase fluid is trapped in the rock pores due to capillary forces formed between CO_2 and the formation brine (residual trapping) and even if a pathway exists, it will not flow. At the meantime, CO_2 starts to dissolve in the resident fluid while the dissolved CO_2 migrates in the formation brine mainly by diffusion. CO2-saturated formation brine is thus transported by convection of the flowing brine away from the injection well (termed solubility trapping). This hydro-chemical process is optimised for cases where underground flows exist to be more effective for very long periods. Not only CO_2 dissolves in the brine, but the brine also dissolves into CO_2 as illustrated in Figure 1.1, like vapourisation of ground surface water into the atmosphere. The loss of water mass thereby increases the salinity to its maximum level and results in

precipitation of salt in the pore throats (Giorgis et al., 2007; Grude et al., 2013). The salt precipitation in return restricts fluid flows, redistributes stress (Osselin et al., 2015) and causes eventually an additional pressure build-up (Espinoza et al., 2011; White et al., 2015). This chemo-mechanical interaction adds a complementary coupling mechanism.

In the long term, for the post-injection period, reactions within the CO2-brine mixture may cause the production of the carbonate minerals of the aquifer that is composed mostly of dolomite and calcite (termed mineral trapping). These geochemical reactions are very slow processes (Andreani et al., 2008; Bacci et al., 2011; Xu et al., 2004). In this period, no overpressure occurs, the mechanical influence is minor compared to the geochemical effect.

The focus of this work is to analyse the injection period of CO_2 storage in deep aquifers, where structural/stratigraphic trapping mechanisms are to be investigated. Special attention is placed on the caprock stability that undergoes the complex thermo-hydro-mechanical processes.

1.4 Objectives and outline of the thesis

This thesis is devoted to risk assessment of CO_2 geological sequestration, which opts for deep aquifers because of its large capacity to host large quantities of CO_2 and caprock integrity to prevent CO_2 leakage. Geological sequestration of CO_2 represents the latest solution available to reduce the CO_2 in the atmosphere. The capacity-integrity double role implies that a correct evaluation of CO_2 storage in deep aquifers must consider the reservoir integrity and the storage capacity aspects at the same time. Many efforts in the last decades were spent to evaluate the performance of the aquifers around the world (Birkholzer et al., 2015). Most of them are devoted to site selection for storage capacity evaluation, but recent advances have also been achieved in understanding the reservoir behaviour through numerical analysis and in-situ monitoring of real scale cases. Most numerical studies focus on a detailed representation of hydraulic and geochemical two-phase flow processes, considering an indeformable reservoir. These modelling approaches omit progressive mechanical mechanisms, in particular, the pressurisation induced expansion and influence of the cooling, which simultaneously mobilises the flow behaviour. The main objectives of this thesis are to understand and model CO_2 injection induced geomechanical instabilities in deep saline aquifers through a general framework of multiphase thermo-hydro-mechanical processes, and to evaluate the application of proposed solutions for the accurate and efficient assessment of geomechanical issues arising from the injection.

The content of the thesis is presented in six chapters, of which Chapter two to Chapter five comprise the main contribution to the objectives. The four main chapters are each free standing with its introduction and conclusion such that each can be read and understood independently.

Chapter two deals with the numerical modelling of hydromechanically coupled processes of CO_2 injection into deep deformable aquifers. After an up-to-date of knowledge about current modelling approaches, the chapter presents a theoretical formulation of the two-phase hydromechanical coupling process. A finite element model is built that is similar to a deep conceptual aquifer to gauge the coupled processes involved during the injection. Numerical simulations are run to analyses the effects of hydromechanical couplings and injection strategies on the mechanical stabilities of the aquifer. The sealing efficiency of the caprock is also evaluated using a local failure indicator on the occurrence of potential failures. Reservoir properties that affect the caprock integrity are also considered to understand further their influence in response to the pressure evolution within the aquifer through a parameter sensitivity analysis.

Based on the understanding of hydromechanical coupling processes in Chapter two, *Chapter three* presents a novel hydro-mechanical approach for the evaluation of surface uplift and caprock deflection induced by underground injection of CO_2. The adopted methodology includes the development of a mathematical model that incorporates the deformable behaviour of the storage reservoir and the flow of two immiscible fluids (CO_2 and brine) within the aquifer while the surface rock or the caprock layer is modelled as a thin plate. Two closed-form analytical solutions are derived and validated with respect to the finite element method as well as to the monitoring measurements of real CO_2 storage site In Salah. Caprock stabilities are assessed by the new approach with a parametric study in parameters such as the injection rate, porosity, rock properties and geological structures. Two solutions can be considered as one of most efficient and accurate design tool for estimating the influence of high injection rates of CO_2 on surface uplift and caprock deformation, which account for the hydraulic and mechanical properties of the reservoir and real CO2 properties.

Chapter four is devoted to the development of multiphase thermo-hydro-mechanical coupled finite element model for the analysis of low-temperature injection of supercritical CO_2 induced instability problems in a deep aquifer. Thermodynamic properties of CO_2 are

analysed after an up-to-date of knowledge about current THM modelling frameworks. A numerical simulation of the In Salah CO_2 storage site in Algeria is thus carried out with a two-dimensional thermo-hydro-mechanical finite element model. Experimental data in the literature and real log data measured on the field are further used for the calibration of the constitutive model. Simulation results allow the fluid and thermal flow processes to be anticipated and geomechanical instabilities to be analysed in a storage system with a horizontal injection well. The model response shows a good agreement with the measured surface uplift at In Salah and also reveals that the combination of overpressure and cooling has a crucial influence on the potential development of shear failure in the caprock and the aquifer.

Chapter five presents an examination of caprock stability in a storage system with a vertical injection well, with a focus on coupled parameters and thermal properties. Based on the framework proposed in Chapter four, a 2D thermo-hydro-mechanical coupled finite element is built, and numerical simulations are carried out to investigate the caprock stability. The simulation results reveal that for a given geometrical configuration and a given temperature difference between injected CO_2 and reservoir, the caprock failure potential may increase or decrease, depending on the combination of thermal-hydro-mechanical parameters: thermal expansion coefficient, stiffness and the Biot coefficient. Therefore, the effects of material properties on the caprock stability should be addressed in a combined way for low-temperature CO_2 injection problems.

Chapter five summarises general conclusions and achievements of this thesis. Finally, outlooks for future research are highlighted.

2 Pressure management in a CO_2 reservoir and its impact on geomechanical stability

2.1 Introduction

The storage of CO_2 in geologic reservoirs, particularly those in deep aquifers, has become a mitigation method used to reduce the impact of CO_2 and the greenhouse effect (Bachu and Bennion, 2007; Bryant, 1997). There are currently several ongoing large-scale projects for CO_2 storage in deep aquifers, such as the In Salah CO_2 storage site in Algeria, in which 3.8 Mt of CO_2 have been injected into a 20-m-thick aquifer at a depth of 1,800 m at a rate of up to 1.2 Mt/yr since 2004 to 2011 (Metz et al., 2005). Such a large volume of CO_2 injections could transform a water reservoir into a CO2 reservoir and result in the accumulation of high pressure. An average wellhead pressure of approximately 16 MPa has been measured (Bohloli et al., 2012), and this value would increase if the injection rate increases (Rutqvist and Tsang, 2002). The overpressure perturbs the stress field within the reservoir, which impacts its hydraulic and mechanical properties and in return impact the fluid overpressure. Such overpressure injection is the result of hydromechanically coupled processes and is considered the driving force behind reservoir instability (Rutqvist, 2012). In fact, the injected CO_2 is of lower density than the aquifer water, resulting in a buoyancy effect that drives CO_2 toward to the top of the aquifer. Thus, a low-permeability sealing caprock must be placed over the target aquifer to avoid potential CO_2 leakage. Rutqvist and Tsang (2002) noted that the highest potential failure occurs in the lower portion of the caprock, i.e., at the aquifer-caprock interface, where a combination of the pressure accumulation and upward pressure occurs (due to the buoyancy effect). Due to such overpressure, pre-existing fractures along the interface may further propagate throughout the entire caprock, thus compromising caprock integrity (Alonso et al., 2012; Rutqvist and Tsang, 2002; Rutqvist et al., 2008; Verdon et al., 2011; Vilarrasa et al., 2010b). Thus, pressure management is crucial in securing the CO_2 storage system.

Geomechanical instabilities have been detected near the injection area from the start of the CO_2 injection at the In Salah project. CO_2 injections resulted in more than 1,500 microseismic events from 2009 to 2010 (Oye et al., 2013), which are believed to be generated by the high CO_2 injection pressure. Using monitoring data, Bohloli, et al. (2012) found that a seismic event occurred once the injection pressure exceeded the formation fracture pressure. However, CO_2 injection also induced surface deformation at a rate of up to 7 mm/yr near the three CO_2 injection wells, as detected by satellite technology (Onuma and Ohkawa, 2009). These observations are not favourable to public acceptance of CO_2

storage projects. Therefore, it is crucial to understand the processes involved in CO_2 injection and their impacts on reservoir stability.

The literature has provided analytical and semi-analytical solutions to assess CO_2 storage processes; these solutions are primarily dedicated to evaluating the fluid flow and pressure evolution during CO_2 storage (Dentz and Tartakovsky, 2008; Nordbotten et al., 2005; Vilarrasa et al., 2010) . In addition, Vasco, et al. (Vasco et al., 2008) investigated surface uplift using a semi-analytical approach, and Selvadurai (Selvadurai, 2009) derived a convenient mathematical model to determine the surface uplift. Based on this information, Li et al. (2015) proposed a hydromechanically coupled solution to assess caprock and surface deformation during injection. Although these models do not describe the detailed hydro-mechanical processes within the injected medium, they could be used to examine CO_2 injection projects in the pre-study stage. To follow all stages of the injection process and to gather additional insights on the portions of the process that are not accessible to measurements, numerical models could be applied as a management tool for assessing the impact of injection-induced pressure on geomechanical stability.

More recently, a number of numerical models have been proposed that refer to the hydromechanical processes that occur during CO_2 injection. Ouellet et al. (2011) investigated the hydromechanical behaviour of a pilot storage site by introducing the pore-pressure evolution from conventional reservoir flow calculations into the calculation of the mechanical equilibrium. No rock stability problems were observed in this pilot project due to the small magnitude of CO_2 injection (17 Kt/yr). In fact, Ouellet et al. (2011) noted that the effect of mechanics on the flow properties could be neglected if the pore pressure variation is small. However, the mechanical effects cannot be neglected for large-scale CO_2 injection projects, such as the In Salah project. Using sequentially coupled simulation (Longuemare et al., 2002), Rutqvist et al. (2010) found that surface uplift occurred during this project and may be explained by not only the elastic expansion of the injection zone but also the pressure changes in the caprock. Vilarrasa et al. (2010b) derived a hydromechanical approach to examine the hydromechanical processes involved in injection of large quantities of CO_2 (2.5-3.6 Mt/yr). In that work, the overpressure increased rapidly and led to plastic strains within the caprock after the first 5 days of injection. Over 3 cm of vertical deformation appeared at the top of the caprock after 100 days of injection.

The main purpose of the current work is to understand the hydromechanically coupled processes that occur in response to CO_2 injection and to develop a pressure management framework to assess CO_2 reservoir stability. The methodology applied to address the coupled processes and emphasises the states of stress and strain that occur in the near field of an injection well, where the strongest coupled hydromechanical changes are present. In the following section, a theoretical framework is proposed using a fully coupled approach to address the multiphase fluid flow, retention properties, and elastoplastic stress-strain relationship of geomaterials. In Section 2.3, a finite element model is established for assessing CO_2 injection into a deep aquifer. In Section 2.4, the hydromechanical processes in the CO_2 reservoir are assessed. The pressure accumulation within the aquifer is then used to evaluate its impact on the stability of the most critical zone, i.e., the interface between the caprock and aquifer, as mentioned previously. For this purpose, a local failure indicator Fs is introduced to quantify the fracture/cracking potential along the interface, which depends on the stress state, the properties of the interface, and the hydro-mechanical responses within the aquifer. A sensitivity study of the key parameter effects on the local failure indicator Fs is conducted to illustrate the implications of the potential risk from an engineering perspective and with respect to the pressure accumulation during CO_2 injection.

2.2 Theoretical framework

The aquifer is initially saturated with water. During CO_2 injection, the porous medium is transformed into a partially saturated medium with two fluid phases, namely CO_2 and water. Injected CO_2 may also dissolve in the water, an aspect that is also considered. The representative elementary volume (REV) of the system is composed of the following components, as shown in Figure 2.1:

- The solid phase, denoted by subscript *s*, contains solid material, such as the aquifer material
- The CO_2 phase, denoted by subscript *c*, contains the injected CO_2 fluid
- The water phase, denoted by subscript *w*, contains two components: aquifer water (*w*) and dissolved CO_2 (*dc)*

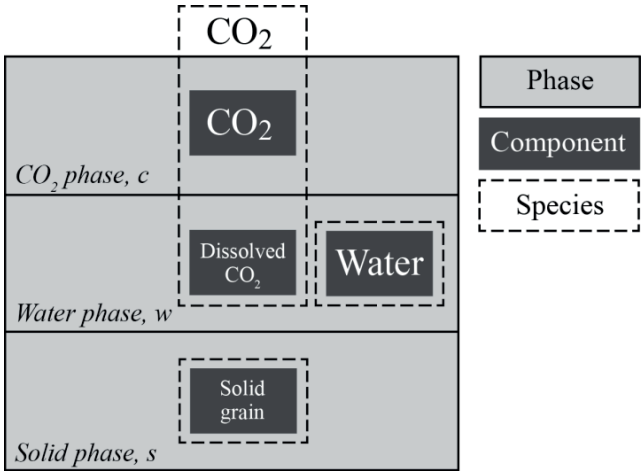

Figure 2.1.Phases, components, and species of the system

The proposed framework allows for the consideration of the most significant hydro-mechanical processes occurring in CO_2 injection, which are summarised as follows: i) the flow of the fluid phases is governed by mechanisms of advective flow and diffusion of dissolved CO_2 in the water phase; ii) the porosity and permeability evolve due to the mechanical stress change; and iii) the retention behaviour depends on porosity. The mechanisms that cover the equilibrium of the mixture include i) the stress-strain relationship and ii) the effective stress changes caused by the changes in fluid pressures.

2.2.1 Mass balance equations

Macroscopic mass balance equations are written following the compositional approach (Charlier et al., 2011) in the context of multiphase flow in deformable porous media, as implemented for water and perfect gas by Collin (2003) in the finite element code *Lagamine*. On this basis, it is extended here to incorporate real fluid properties. This approach describes the mass balances for the species present in the mixture rather than for the phases. Therefore, the conservation of mass of each chemical species (*Water species* and *CO_2 species* indicated in Figure 2.1) is assumed. This approach has an advantage in that the phase exchange terms cancel out, which is particularly interesting when assuming equilibrium between phases.

The mass balance equations as well as the water and CO_2 fluid flows are expressed in the moving current configuration using a Lagrangian updated formulation (Charlier et al.,

2011), through which the solid mass is automatically conserved and large deformations and displacements can be considered.

The following primary state variables are chosen to describe the state of the material: water phase pressure p_w, CO_2 phase pressure p_c, temperature T and solid displacement field $\mathbf{u}$.

Solid

For a given volume V of the REV, the Lagrangian mass balance equation of solid is expressed as

$$\frac{d\left((1-n)\rho_s V\right)}{dt} = 0 \tag{2.1}$$

where n is the porosity of the solid matrix, ρ_s is the solid density, and t is time. The expression of the solid density variation from Lewis and Schrefler (1998) is adapted in this study as follows:

$$\frac{1}{\rho_s}\frac{d\rho_s}{dt} = \frac{1}{1-n}\left[\frac{(b-n)}{K_s}\frac{\partial\left(S_w p_w + (1-S_w)p_c\right)}{\partial t} - (1-b)\,\mathbf{div}\left(\frac{\partial \mathbf{u}}{\partial t}\right)\right] \tag{2.2}$$

with a volumetric deformation rate $\frac{1}{V}\frac{dV}{dt} \approx \mathbf{div}\left(\frac{\partial \mathbf{u}}{\partial t}\right)$ and where b is the Biot coefficient and K_s is the bulk modulus of the solid particles. The water phase saturation S_w is a function of the capillary pressure (suction) s. The suction is defined as the difference between the CO_2 phase and water phase pressures, or $s = p_c - p_w$. The relationship between the saturation and suction will be given hereafter. Introducing Eq. (2.2) into Eq. (2.1), the solid mass conservation equation is expressed by the primary state variables and variation of porosity:

$$\frac{dn}{dt} = (b-n)\left[\frac{1}{K_s}\frac{\partial}{\partial t}\left(S_w p_w + (1-S_w)p_c\right) + \mathbf{div}\left(\frac{\partial \mathbf{u}}{\partial t}\right)\right] \tag{2.3}$$

Water species:

The Eulerian form of the mass balance equation of the *water specie* is written as:

$$\frac{\partial\left(nS_w\rho_w\right)}{\partial t}+\mathbf{div}\left(\rho_w\mathbf{q}_w\right)=0 \tag{2.4}$$

where the last term in Eq. (2.4) corresponds to the advection of the water phase, which is governed by the Darcy law. Combined with Eq. (3), the mass balance equation of the *water specie* in a deformable material is extended to:

$$\begin{aligned}&\left[-n\rho_w\frac{\partial S_w}{\partial s}+nS_w\frac{\partial\rho_w}{\partial p_w}+\frac{b-n}{K_s}S_w\rho_w\left(S_w+\frac{\partial S_w}{\partial s}s\right)\right]\frac{\partial p_w}{\partial t}\\&+\left[n\rho_w\frac{\partial S_w}{\partial s}+\frac{b-n}{K_s}S_w\rho_w\left(1-S_w-\frac{\partial S_w}{\partial s}s\right)\right]\frac{\partial p_c}{\partial t}\\&+bS_w\rho_w\mathbf{div}\left(\frac{\partial\mathbf{u}}{\partial t}\right)\\&+\mathbf{div}\left(-\rho_w\frac{\mathbf{k}k_{rw}}{\mu_w}\left[\mathbf{grad}\left(p_w\right)+\rho_w\mathbf{g}\right]\right)=0\end{aligned} \tag{2.5}$$

in which μ_w is the water phase viscosity, $\mathbf{k}$ is the intrinsic permeability tensor, and k_{rw} is the relative permeability of the water phase.

CO_2 species:

Before writing the mass balance equation for the *CO_2 species*, we present the mass balance equations separately for two *components* of the *species*: the *CO_2 component* in the CO_2 phase and the *dissolved CO_2 component* in the water phase.

CO_2 Component

The mass conservation of the *CO_2 component* is written as

$$\frac{\partial\left(n\left(1-S_w\right)\rho_c\right)}{\partial t}+\mathbf{div}\left(\rho_c\mathbf{q}_c\right)=f_{CO2-w} \tag{2.6}$$

where ρ_c is the CO_2 phase density and f_{CO2-w} is the rate at which the *CO_2 component* transferred from the CO_2 phase to the water phase (dissolution phenomenon). The last term corresponds to the advection of the gas phase, which is governed by Darcy's law.

Similar to the mass equations of water, the mass equations (2.6) can be extended as follows:

$$\begin{aligned}
&\left[-n\rho_c\frac{\partial S_w}{\partial s}+n\left(1-S_w\right)\frac{\partial \rho_c}{\partial p_c}+\frac{b-n}{K_s}\left(1-S_w\right)\rho_c\left(1-S_w-\frac{\partial S_w}{\partial s}s\right)\right]\frac{\partial p_c}{\partial t}\\
&+\left[n\rho_c\frac{\partial S_w}{\partial s}+\frac{b-n}{K_s}\left(1-S_w\right)\rho_c\left(S_w+\frac{\partial S_w}{\partial s}s\right)\right]\frac{\partial p_w}{\partial t}\\
&+\left(1-S_w\right)\rho_c\cdot b\cdot\mathrm{div}\left(\frac{\partial \mathbf{u}}{\partial t}\right)\\
&+\mathrm{div}\left(-\rho_c\frac{\mathbf{k}k_{rc}}{\mu_c}\left[\mathbf{grad}\left(p_c\right)+\rho_c\mathbf{g}\right]\right)=f_{CO2-w}
\end{aligned} \tag{2.7}$$

in which μ_c is the CO2 phase viscosity and k_{rc} is the relative permeability of the CO2 phase. $\partial\rho_c/\partial p_c$ is the change in CO_2 density with the pressure change. Because CO_2 is not considered as an ideal gas, a compressibility factor Z must be used to describe the deviation from the behaviour of an ideal gas. This factor is a pressure- and temperature-dependent parameter and can be derived from different equations of state (EOSs). The relationship between the density, temperature, and pressure is written as

$$\rho_c=\frac{1}{Z}\frac{M_c}{R}\frac{p_c}{T} \tag{2.8}$$

where M_c is the molar mass of CO_2 and R is the universal gas constant. We obtain the following expression by taking the derivative of Eq. (2.8) with respect to the pressure:

$$\frac{\partial \rho_c}{\partial p_c}=\frac{M_c}{RT}\left(\frac{1}{Z}-\frac{p_c}{Z^2}\frac{\partial Z}{\partial p_c}\right) \tag{2.9}$$

The advantage of expressing the density change as a function of Z is that one can express the compressible behaviour of CO_2 without choosing a suitable EOS. In this study, the factor Z is calculated according to Peng and Robinson's EOS (Peng and Robinson, 1976).

Dissolved CO_2 component

The mass conservation of the *dissolved CO_2 component* in water phase is written as

$$\frac{\partial\left(nS_w\rho_{dc}\right)}{\partial t}+\mathbf{div}\left(\mathbf{i}_{dc}\right)+\mathbf{div}\left(\rho_{dc}\mathbf{q}_w\right)=f_{w-CO2} \tag{2.10}$$

where ρ_{dc} is the mass of dissolved CO_2 per unit volume of water and $\mathbf{div}\left(\mathbf{i}_{dc}\right)$ is the diffusion of dissolved CO_2 in the water phase due to different concentrations of dissolved CO_2 in the water phase. $\mathbf{div}\left(\mathbf{i}_{dc}\right)$ is governed by Fick's law, which is shown in the last term on the left-hand side of Eq.(2.11). The mass equation can be obtained as

$$\begin{aligned}
&\left\{n\rho_{dc}\frac{\partial S_w}{\partial s}+nS_w\frac{\partial\rho_{dc}}{\partial p_c}+\frac{b-n}{K_s}S_w\rho_{dc}\left(1-S_w-\frac{\partial S_w}{\partial s}s\right)\right\}\frac{\partial p_c}{\partial t}\\
&+\left\{-n\rho_{dc}\frac{\partial S_w}{\partial s}+\frac{b-n}{K_s}S_w\rho_{dc}\left(S_w+\frac{\partial S_w}{\partial s}s\right)\right\}\frac{\partial p_w}{\partial t}\\
&+S_w\cdot\rho_{dc}\cdot b\cdot\mathrm{div}\left(\frac{\partial\mathbf{u}}{\partial t}\right)\\
&+\mathrm{div}\left(-\rho_{dc}\frac{\mathbf{k}k_{rw}}{\mu_w}\left(\mathbf{grad}\left(p_w\right)+\rho_w\mathbf{g}\right)\right)\\
&-\mathrm{div}\left(nS_w\tau D_c\rho_w\mathbf{grad}\left(\rho_{dc}/\rho_w\right)\right)=f_{w-CO2}
\end{aligned} \tag{2.11}$$

where ρ_{dc} is the density of dissolved CO_2 governed by the extended Henry law (see the section on constitutive equations). The second-to-last term on the left side refers to the advection flow of dissolved CO_2 due to the water phase pressure difference. The last term on the left side expresses the diffusion of dissolved CO_2 in the water phase, where D_c is the diffusion coefficient of the dissolved CO_2 in the water phase, τ is the tortuosity of the porous media, and f_{w-CO2} is the rate at which the dissolved CO_2 transfers from the water phase to the CO_2 phase (degassing phenomenon).

With $f_{CO2-w}=-f_{w-CO2}$, the compositional approach allows for the elimination of the interphase mass exchange term. Adding Eqs. (2.7) and (2.11) to Eq. (2.9), the mass balance equation of the *carbon dioxide specie* is obtained as

$$
\begin{aligned}
&\left\{ \begin{aligned} &n\left(\rho_{dc}-\rho_c\right)\frac{\partial S_w}{\partial s}+nS_w\frac{\partial \rho_{dc}}{\partial p_c}+n\rho_c\left(1-S_w\right)\left(\frac{1}{p_c}-\frac{1}{Z}\frac{dZ}{dp_c}\right) \\ &+\frac{b-n}{K_s}\left[S_w\rho_{dc}+\left(1-S_w\right)\rho_c\right]\left(1-S_w-\frac{\partial S_w}{\partial s}s\right) \end{aligned} \right\}\frac{\partial p_c}{\partial t} \\
&+\left\{-n\left(\rho_{dc}-\rho_c\right)\frac{\partial S_w}{\partial s}+\frac{b-n}{K_s}\left[S_w\rho_{dc}+\left(1-S_w\right)\rho_c\right]\left(S_w+\frac{\partial S_w}{\partial s}s\right)\right\}\frac{\partial p_w}{\partial t} \\
&+\left[S_w\rho_{dc}+\left(1-S_w\right)\rho_c\right]\cdot b\cdot \mathrm{div}\left(\frac{\partial \mathbf{u}}{\partial t}\right) \\
&+\mathrm{div}\left(-\rho_{dc}\frac{\mathbf{k}k_{rw}}{\mu_w}\left[\mathbf{grad}\left(p_w\right)+\rho_w\mathbf{g}\right]\right) \\
&+\mathrm{div}\left(-\rho_c\frac{\mathbf{k}k_{rc}}{\mu_c}\left[\mathbf{grad}\left(p_c\right)+\rho_c\mathbf{g}\right]\right) \\
&-\mathrm{div}\left(nS_w\tau D_c\rho_w\mathbf{grad}\left(\rho_{dc}/\rho_w\right)\right)=0
\end{aligned}
\tag{2.12}
$$

The quantities $\mathbf{k}, k_{rc}, k_{rw}, S_w$ in the mass conservation equations and the fluid properties, such as density and viscosity, will be detailed in the section related to the constitutive equations.

Equations (2.5) and (2.12) lead to a coupled set of mass conservation equations or partial differential equations that govern the studied phenomenon.

2.2.2 Momentum balance equation

The equilibrium equation of the mixture is given by

$$\mathbf{div}\left(\boldsymbol{\sigma}\right)+\rho\mathbf{g}=0 \tag{2.13}$$

where $\boldsymbol{\sigma}$ is the total stress tensor and ρ is the density of the mixture defined as

$$\rho=\left(1-n\right)\rho_s+nS_w\rho_w+n\left(1-S_w\right)\rho_c \tag{2.14}$$

The total stress can be decomposed into effective stress and pore pressures, as shown in Eq. (2.15) (Laloui and Nuth, 2009; Nuth et al., 2010).

$$\boldsymbol{\sigma}'=\boldsymbol{\sigma}-p_c\mathbf{I}+S_w\left(p_c-p_w\right)\mathbf{I} \tag{2.15}$$

An average fluid pressure is defined as follows and is weighted by the saturation of each phase:

$$p_f = S_w p_w + \left(1 - S_w\right) p_c \tag{2.16}$$

The effective stress in Eq. (2.15) thus becomes

$$\boldsymbol{\sigma}' = \boldsymbol{\sigma} - p_f \mathbf{I} \tag{2.17}$$

2.2.3 Constitutive equations

2.2.3.1 CO_2 properties

To consider the real properties of CO_2, the EOS of Peng and Robinson (1976) is employed to calculate the CO_2 density as shown in Appendix 8.1. The Henry law is extended to a high-pressure condition using the CO_2 fugacity (see Appendix 8.1) coefficient according to Pruess and Garcia (2002), which is a key property used to express the potential of a real gas to dissolve into water (Spycher et al., 2003). The CO_2 fugacity coefficient Φ is determined according to Peng and Robinson (1976). In addition, the CO_2 viscosity is calculated according to Fenghour, et al. (1998). As shown in Figure 2.2, the CO_2 density, fugacity, and viscosity vary significantly with pressure for a given temperature.

An extended Henry law is employed to govern the equilibrium between dissolved CO_2 and CO_2 in the gas phase. Using the CO2 fugacity, the extended Henry law characterises the dissolved quantities in the water at a constant temperature (Pruess and García, 2002):

$$\Phi p_c = K_{eq,g-l}^{co_2} X_{dc} \tag{2.18}$$

where $K_{eq,g-l}^{co_2}(T)$ is Henry's coefficient, which depends only on the temperature, and X_{dc} is the mass fraction of dissolved CO_2 in water. Combing Eq. (2.8) yields an explicit expression for dissolved CO2 quantity

$$\rho_{dc} = \frac{\Phi Z \rho_w RT}{K_{eq,g-l}^{co_2} M_w} \rho_c \tag{2.19}$$

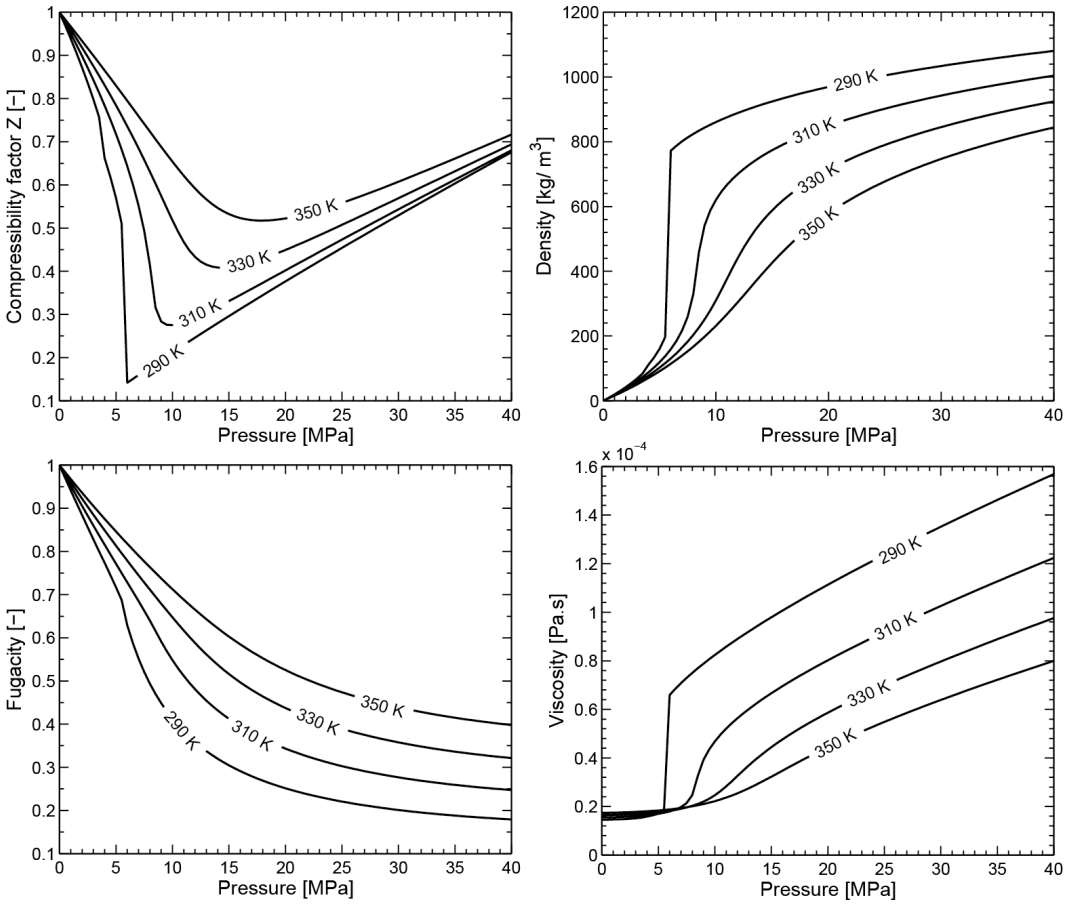

Figure 2.2. Calculated compressibility factor Z, CO_2 density, fugacity, and viscosity

2.2.3.2 Hydraulic properties

The water retention curve is defined as the relationship between the degree of saturation S_w, equal to the volume of liquid water over the volume of voids $\left(S_w + S_{co_2}\right)$, and the suction s. A van Genuchten function (van Genuchten, 1980) is commonly used to describe the retention behaviour of the aquifer, as shown in Eq. (2.20). *m* and P_r are a material parameter and the reference pressure, respectively:

$$S_w = \left(1 + \left(s / P_r\right)^{1/(1-m)}\right)^{-m} \tag{2.20}$$

The equations for the relative permeability of each phase follow a power law as

$$\begin{aligned} k_{rw} &= S_w^{CKW} \\ k_{rc} &= \left(1 - S_w\right)^{CKC} \end{aligned} \tag{2.21}$$

where CKW1 and CKC1 are material parameters.

Another aspect of the coupling between hydraulics and mechanics is the link between the intrinsic permeability and porosity, which is expressed by the Kozeny-Carman relationship (Scheidegger, 1958):

$$k = k_0 \left[\frac{n/n_0}{(1-n)/(1-n_0)} \right]^{\eta} \tag{2.22}$$

where k_0 is the initial isotropic intrinsic permeability, n_0 is the initial porosity, and η is a material parameter. This relationship defines one side of the hydromechanical coupling.

2.2.3.3 Elastoplastic geomechanical model

The Drucker Prager (D-P) elastoplastic model is employed to describe the behaviour of the matrix, which was implemented in the finite element code *Lagamine* (Barnichon and Charlier, 1996). The total strain increment $\mathrm{d}\boldsymbol{\varepsilon}$ is decomposed into linear $\mathrm{d}\boldsymbol{\varepsilon^e}$ and plastic $\mathrm{d}\boldsymbol{\varepsilon^p}$ components. The elastic component of the deformation is calculated according to Hooke's law, which depends on Young's modulus E and the Poisson's ratio ν.

A yield function *f* distinguishes the elastic and plastic domains. The material is elastic when *f<0*, whereas the equality *f* =0 implies that the stress state of the material reaches its yield point, and plasticity is induced when *df>0*. The D-P yield function is written using the first invariant of the effective stress I_σ and second invariant of the deviatoric stress II_σ, which are expressed in terms of the principal effective stresses $\sigma_1', \sigma_2', \sigma_3'$ in the following:

$$\begin{aligned} I_\sigma &= \sigma_1' + \sigma_2' + \sigma_3' = 3p' \\ II_\sigma &= \frac{1}{6}\left[\left(\sigma_1' - \sigma_2'\right)^2 + \left(\sigma_1' - \sigma_3'\right)^2 + \left(\sigma_2' - \sigma_3'\right)^2 \right] = \frac{1}{3} q^2 \end{aligned} \tag{2.23}$$

where *p'* is the mean effective stress and *q* is the deviatoric stress.

The D-P yield function is defined as

$$f = II_\sigma + MI_\sigma - K \tag{2.24}$$

The D-P yield surface is a smooth version of the Mohr-Coulomb (M-C) yield surface. Parameters M and K are expressed in terms of the friction angle ϕ_c, and cohesion c, which are used to characterise the M-C yield surface. If the D-P surface is assumed to be circumscribed onto the M-C surface (i.e., in compression), the parameters are written as

$$M = \frac{2\sin\phi_c}{\sqrt{3}\left(3-\sin\phi_c\right)} \qquad K = \frac{6c\cos\phi_c}{\sqrt{3}\left(3-\sin\phi_c\right)} \tag{2.25}$$

The plastic potential g is defined in a similar manner as the yield surface function:

$$g = II_\sigma + M'I_\sigma \tag{2.26}$$

where the parameter M' is related to the dilatancy angle Ψ as

$$M' = \frac{2\sin\Psi}{\sqrt{3}\left(3-\sin\Psi\right)} \tag{2.27}$$

When the dilatancy angle is equal to the friction angle ($M=M'$), the flow rule is associated. The plastic strain vector is given by

$$d\boldsymbol{\varepsilon}^p = \lambda\frac{\partial g}{\partial \boldsymbol{\sigma}} \tag{2.28}$$

The plastic multiplier λ is determined using the consistency condition.

2.3 Conceptual aquifer

An axisymmetric aquifer is chosen for current investigation, as shown in Figure 2.3. The CO_2 is injected through a vertical well (radius = 0.2 m) along the entire thickness of the aquifer (100 m). The top of the aquifer is located 1,000 m underground. The model is extended to 1 km from the injection well to avoid the influence of boundary conditions on the critical zone of evaluation.

Instead of modelling all of the overburden media, a constant distributed stress is assumed at the top of the aquifer. Horizontal and vertical displacements are fixed at the right and bottom of the boundaries, respectively. An initial water pressure is applied with a gradient of 10 MPa/km. Next, a CO_2 mass flow is applied at a constant rate of 3.5 Mt/yr on the left boundary. The water pressure is held constant at the right boundary, through which fluid flow is allowed. An isothermal condition of 330 K is assumed in this study.

In terms of the initial stress regime, the ratio between the horizontal and vertical stress is controlled by the initial effective stress factor K_0 as follows:

$$\sigma'_h = K_0 \sigma'_v \tag{2.29}$$

As reported by Rutqvist, et al. (2010), if the horizontal stress is greater than the vertical stress $K_0>1$, a compression stress regime is obtained and shallow fractures that will not propagate through the caprock are likely to occur. When the vertical stress is greater than the horizontal stress $K_0<1$, steeply dipping fractures are likely to occur in such a stress regime, and the fractures may penetrate the caprock from the interface. From a risk analysis perspective, we consider the last case, which is unfavourable for the safety of the CO_2 project. In addition, we consider fractures distribute randomly within the aquifer. Thus a zero cohesion may be assumed and a large range for friction angle 17-30° are investigated to assess the likelihood of mechanical failure.

The study represents a general investigation of the response of an aquifer and the influence of input parameters as summarised in Table 2.1 Material parameters used for the finite element model. The properties of the materials are chosen as representative for a sandstone aquifer and after the literature (Rohmer and Seyedi, 2010; Rutqvist et al., 2010; Vilarrasa et al., 2010b). The results and related discussions are therefore considered qualitatively.

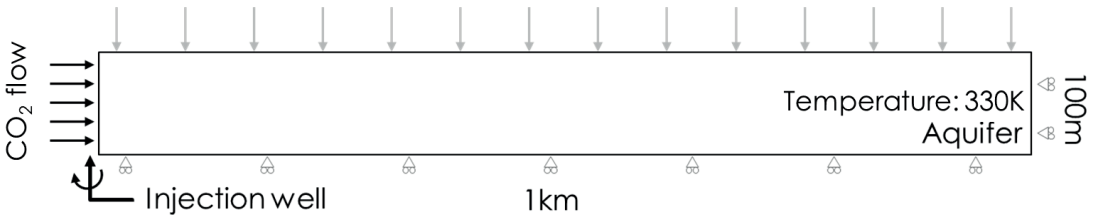

Figure 2.3. Geometry and boundary conditions of the aquifer considered

Table 2.1 Material parameters used for the finite element model

Material properties	Symbol	Unit	Sandstone
Intrinsic permeability	k	m^2	1×10^{-13}
Kozeny-Carman parameter	η	-	5.33
Water relative permeability parameter	CKW	-	4
CO_2 relative permeability parameter	CKC	-	3
Initial porosity	n_0	-	0.125
Van Genuchten parameter	Pr	MPa	0.02
Van Genuchten parameter	m	-	0.5
Tortuosity	τ	-	0.5
Young's Modulus	E	MPa	2.1×10^4
Poisson ratio	ν	-	0.25
Dilatancy angle	Ψ	°	0
Cohesion	c	Pa	0
Friction angle	ϕ_c	°	17-30
Initial stress factor	K_0	-	0.6
Aquifer density	ρ_s	kg/m^3	2600
Biot coefficient	b	-	1

2.4 Hydromechanical process within the aquifer

Figure 2.4 represents (a) the temporal evolution of both fluid pressures and (b) the relationship between the averaged fluid pressure p_f and mean effective stress p' as well as the deviatoric stress q on the top of the aquifer and next to the injection well. As shown in Figure 2.4a, both the water and CO_2 pressures increase rapidly during the first injection stage (near 2.5 days). The CO_2 begins to desaturate the aquifer, resulting in a rapid reduction of the relative permeability of water. The excess pore water pressure does not have sufficient time to dissipate, thus causing the water pressure to increase. However, CO_2 follows the same growing trend in pressure to maintain the injection rate. Thus, the averaged fluid pressure increases until the pores near the injection well are filled with CO_2. Subsequently, CO_2 can flow easily, and water begins to dissipate. As shown in Figure 2.4b, the mean effective stress p' decreases by 2.5 MPa during the first half day due to the generation of fluid overpressure, whereas the deviatoric stress q is only reduced by 0.54 MPa. This situation indicates a risky period during which the medium loses confinement and shearing persists, and thus, the integrity may be compromised. The averaged fluid pressure continues to increase and reaches a maximum after 2.5 days of injection, after which it decreases. In response, the mean effective stress increases, although the deviatoric stress decreases slightly and remains nearly constant after 30 days. From a geomechanical

perspective, confinement is recovered without additional shearing in the medium, which leads to safer CO_2 injection conditions as long as the injection lasts. Our results are consistent with the observations of Vilarrasa et al. (2010b).

The averaged fluid pressure along the top of the aquifer decreases with the distance to the injection well, as shown in Figure 2.5a. Compared to the water saturation profile (Figure 2.5b), a fluid pressure drop appears in the vicinity of the water-CO_2 interface. As the overall permeability is reduced because of desaturation, the overpressure is greater than that in water saturated zone, which leads to a decrease in overpressure at the water-CO_2 interface. The drop propagates with the distance as the CO_2 injection persists and tends to dissipate with injection time (see 30 days in Figure 2.5a). In addition, the pressure in the water saturated zone increases slightly.

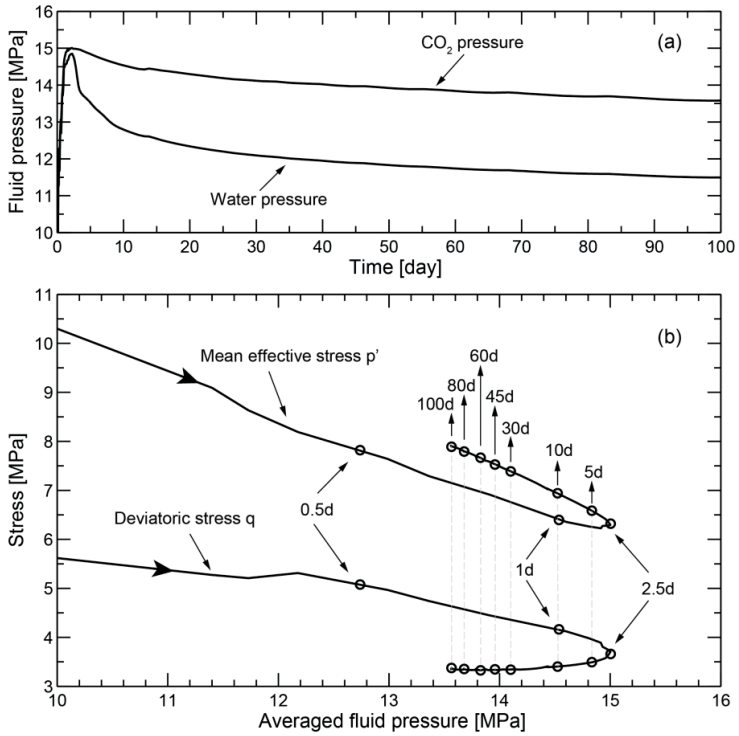

Figure 2.4. (a) Temporal evolution of the water and CO_2 pressures, (b) temporal evolution of the relationship between the stresses and average fluid pressure on the top of the aquifer and next to the injection well

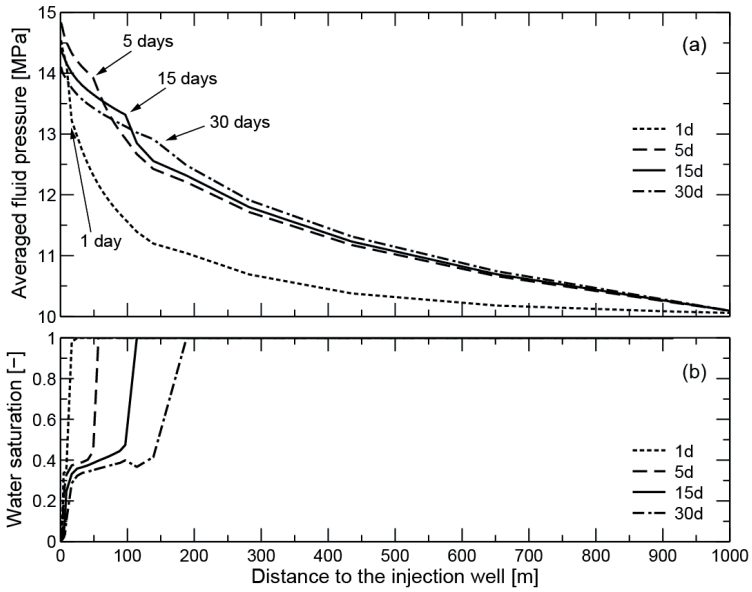

Figure 2.5. Horizontal profile of (a) averaged fluid pressure and (b) water saturation along the top of aquifer for different times

In Figure 2.6, the stress path in the (p', q) plan for a 100-day injection is shown by the point at the top of the aquifer next to the injection well. The initial stress state is represented by point A (initial mean effective stress of 5.6 MPa and an anisotropic state represented by a K_0 of 0.6). As mentioned previously, once the injection begins, the mean effective stress decreases sharply and the deviatoric stress is reduced slightly. Therefore, the stress path moves directly toward the D-P yield envelope (Point B). The plasticity begins from the moment at which the stress path reaches the yield envelope, causing irreversible deformation in 1 day (until Point C). The stress path subsequently follows the D-P yield envelope as the averaged fluid pressure continues to increase. As the overpressure continues to drop, the mean effective stress begins to increase and the stress path returns to a safe condition (Point D) that is located far away from the D-P yield envelope.

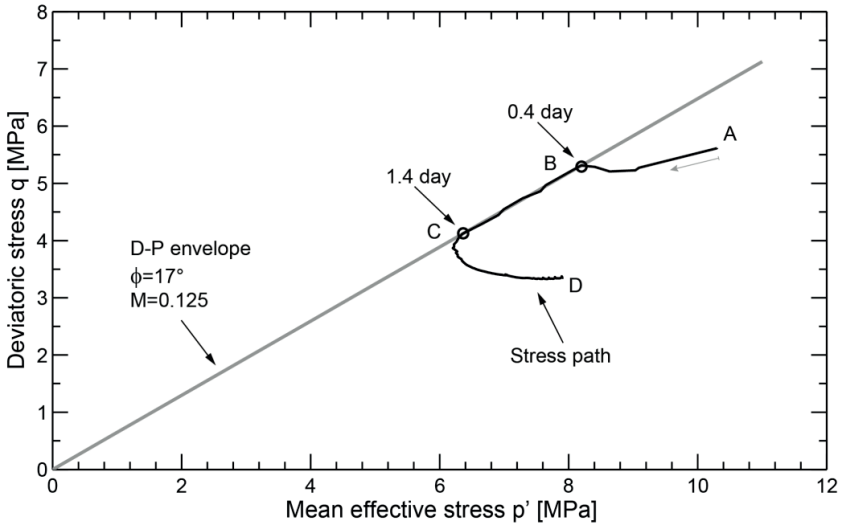

Figure 2.6. Stress path during first 30 days of injection at the top of the aquifer and next to the injection well

Figure 2.7 presents the plastic strain development in a 100×100-m area next to the injection well compared to the water saturation. Once the yielding begins, the plastic strain follows and accumulates at the top of the aquifer and extends along the injection well. The plastic zone expands faster than the desaturation of water. After 1.5 days, when the overpressure begins to decrease, the plastic strain tends to stabilise by extension. After the 5th day, because the overpressure begins to decrease in the entire aquifer, the stress state remains far from the yield envelope, as indicated in the stress path evolution (Point D in Figure 2.7). Thus, the plastic zone remains unchanged as the CO_2 saturation continues to advance. Most of the plastic strain occurs and extends 50 m from the injection well at the top of the aquifer, which may induce damage at the interface between the caprock and aquifer.

The vertical displacement profile along the top of the aquifer is plotted with respect to different injection times, as shown in Figure 2.8. After the CO_2 injection begins, the overpressure Δp_f increases and the effective stress σ_1' decreases (the total stress σ_1 is constant), which produces vertical deformations. After 1 day of injection, the vertical displacement induced by overpressure reaches a maximum next to the injection well and progressively decreases with the distance from the injection well, an observation that is in agreement with the averaged fluid pressure distribution (indicated by 1d in Figure 2.5a). Next to the injection well, the vertical displacement reaches a maximum on the fifth day of injection and subsequently decreases. The displacement decreases with time because the

effective stress σ_1' begins to increase due to dissipation of the overpressure. The location next to the injection well does not always encounter the maximum displacement during injection. In contrast, the point of maximum displacement translates in the advancing direction of the CO_2 front, which is consistent with the observation of fluid pressure drop propagation shown in Figure 2.5a.

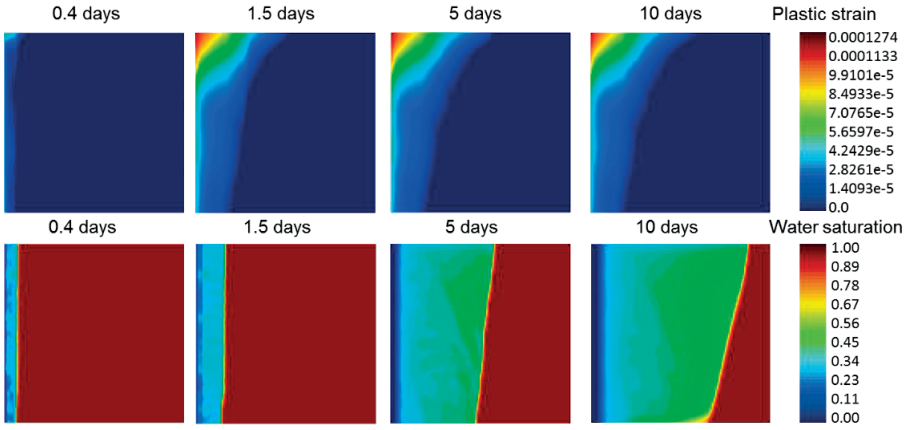

Figure 2.7. Plastic strains and water saturation of the 100×100-m zone next to the injection well for different times.

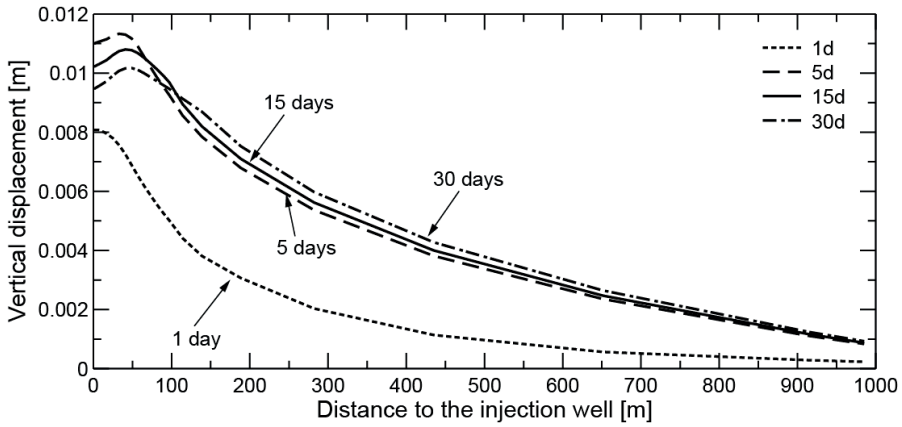

Figure 2.8. Vertical displacement profile along the top of the aquifer as a function of the distance to the injection well for different times

2.4.1 Effect of the friction angle of the aquifer

The friction angle is believed to have a significant effect on the plasticity development because it controls the slope of the D-P envelope. In Figure 2.9, the D-P envelopes are plotted together with the stress paths simulated using four different possible friction angles

of the aquifer. When injection begins, all stress paths move toward the D-P envelope due to the generation of fluid overpressure (decrease in the mean effective stress). Two of the friction angles (17° and 21°) encounter the D-P envelopes at different stress states: the mean effective stress remains higher for a higher friction angle when the stress path encounters the D-P envelope for the same initial state. The stress paths of friction angles 25° and 30° are nearly superposed and do not encounter the yield envelope when the induced fluid overpressure reaches the maximum. Therefore, no plasticity occurs.

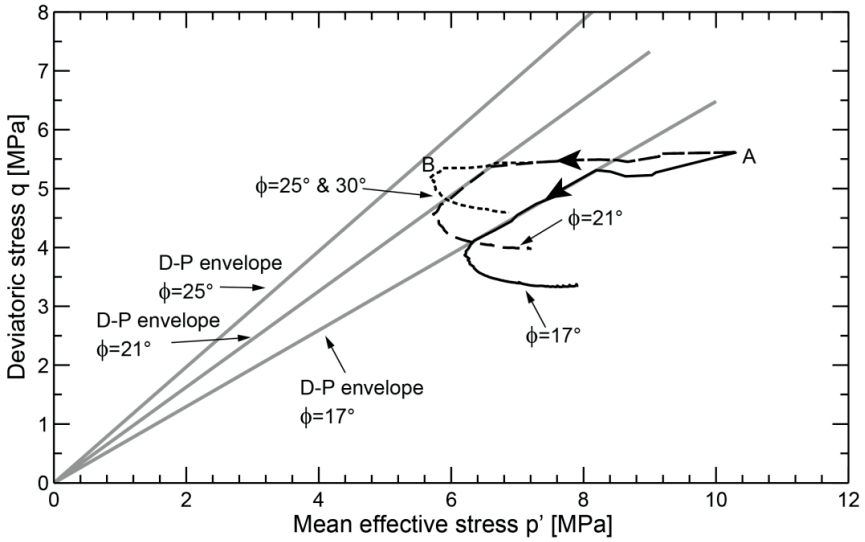

Figure 2.9. Stress paths evolved with four different friction angles of the aquifer during the first 30 days of injection at the top of the aquifer and next to the injection well

2.4.2 Influence of the CO_2 injection strategy

The fluid overpressure is directly linked to the target CO_2 injection rate for a given site. Two scenarios are investigated to determine the impact of constant injection at different target rates on the overpressure response, namely, 1 and 3.5 Mt/yr. Figure 2.10 plots the fluid pressure evolution with respect to the two rates plotted by Curves A and B, respectively. As expected, the magnitude of the fluid overpressure is proportional to the target injection rate. Moreover, both schemas display the same behaviour such that the averaged fluid pressure reaches a maximum value rather quickly and then decreases slightly. This observation illustrates the important role of a target injection rate in limiting the overpressure. However, for a commercial project, a high injection rate must be maintained eventually for economic reasons.

As discussed, constant injection of CO_2 at the target rate causes high overpressure. An increase in the injection rate to a target value may allow more time for pressure dissipation, the efficiency of which remains to be investigated. Three scenarios with increasing injection rates are defined below (with their pressure responses indicated in Figure 2.10).

1. Gradual increase in the injection rate to 3.5 Mt/yr over 10 days (Curve C)
2. Stepwise increase from the maintenance rate of 1 Mt/yr over 10 days (along Curve A), with a subsequent increase to 3.5 Mt/yr over the following 5 days (Curve D)
3. Stepwise increase from the maintenance rate of 1 Mt/yr over 10 days (along Curve A), with a subsequent increase to 3.5 Mt/yr over the following 10 days (Curve E).

As shown, the pressure profiles from the three injection schemas intersect with Curve B (constant injection rate) after reaching the target value, subsequently follow along Curve B, and end with a tendency to converge. The maximum fluid pressure induced by each increasing-rate injection can be approximated by that of the constant-rate injection at the intersection point because the difference between the two cases is minor. As Curve B continues to decrease, a longer duration of increase in the injection rate yields a lower maximum fluid pressure. In other words, an increasing-rate injection will produce a similar overpressure as that induced by a constant-rate injection regardless of whether the duration of increase is short.

Although the injection scenarios with gradual and stepwise increases in injection rates are capable of decreasing the maximum level of overpressure, this approach cannot be employed as a major strategy to limit the overpressure because the increasing time must be sufficiently long. Furthermore, the effect of limitations in overpressure may not be significant or could be quite poor when considering a low-permeability boundary (Vilarrasa et al., 2010b).

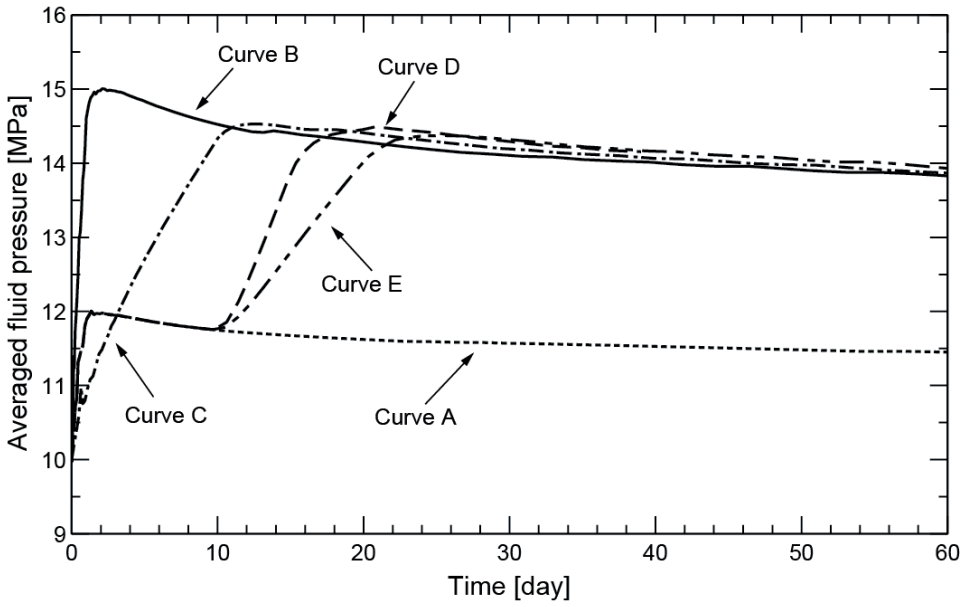

Figure 2.10. Averaged fluid pressure responses to different injection strategies: Curve A: constant injection rate of 1 Mt/yr; Curve B: constant injection rate of 3 Mt/yr; Curve C: increasing injection rate from 0 to 3 Mt/yr over 10 days; Curve D (resp. Curve E): constant injection rate of 1 Mt/yr over 10 days and increasing injection rate from 1 to 3 Mt/yr over the following 5 days (resp. during 10 days).

2.5 Assessment methodology on geomechanical stability

As analysed previously, CO_2 injection rapidly increases the fluid pressure within the aquifer, which reduces the effective stress along the interface between the aquifer and caprock. The failure potential may initiate CO_2 leakage through the CO_2 sealing caprock if pre-existing fractures are presented. Thus, we assume a contact interface overlaid at the top of the aquifer to evaluate the impact of the overpressure on its integrity. For risk management considerations, conservative assumptions can be applied: (1) fractures can pre-exist along the interface with an arbitrary orientation, as noted by Rutqvist, et al. (2007); (2) the injection induced overpressure Δp_f is fully applied on the interface; and (3) the interface is cohesionless ($c = 0$) and without tensile strength. The Mohr-Coulomb failure criterion is employed to assess the failure potential along the interface, which includes the friction angle ϕ_c and cohesion c of the interface:

$$\tau = \sigma_n' \sin\phi_c + c\cos\phi_c \tag{2.30}$$

where τ and σ_n' are the shear stress and normal effective stress, respectively. The above equation represents a failure line in the Mohr diagram, as shown in Figure 2.11.

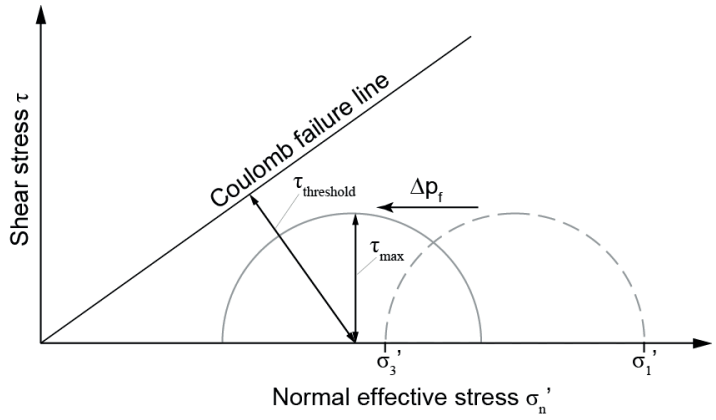

Figure 2.11. Schematic view of the Mohr diagram in which the Mohr circle is displaced due to the increase in fluid pressure (cohesion $c=0$)

Once injection begins, the circle representing the state of stress (Figure 2.11) will move toward the Coulomb failure line due to the increased fluid pressure, which decreases the effective stress. Shear failure is likely to occur when the circle is tangent to the Coulomb failure line such that the distance between the Mohr circle and line becomes null. This fact can be determined with the definition of a failure indicator F_s to achieve a meaningful measurement of the likelihood of mechanical failure:

$$\mathrm{F_s} = \frac{\tau_{threshold}}{\tau_{\max}} \tag{2.31}$$

where $\tau_{\max}$ is the current maximum shear stress (which is the radius of the Mohr circle) and corresponds to a threshold shear stress state where the failure occurs $\tau_{\text{threshold}}$(which is the distance from the centre of the Mohr circle to the failure line), as written as

$$\tau_{\max} = \frac{\left(\sigma_1' - \sigma_3'\right)}{2} \tag{2.32}$$

$$\tau_{threshold} = \frac{\left(\sigma_1' + \sigma_3'\right)}{2}\sin\phi_c + c\cos\phi_c \tag{2.33}$$

where σ_1' and σ_3' are the maximum and minimum principal effective stress components, respectively.

The failure indicator F_s>1, which occurs when the threshold shear stress $\tau_{threshold}$ is higher the current maximum shear stress τ_{max}, indicates that the integrity is not compromised. It is necessary to note that the F_s is a local indicator. The fulfilment of failure criterion at one location does not yield the global failure of the aquifer.

As the fluid pressure increases, the Mohr circle will cross through the Coulomb failure line to the left of the τ-axis; this situation will lead to a negative minimum effective stress σ_3', which signifies a tensile fracture occurrence. The criterion is written as follows:

$$\sigma_3' \leq 0 \tag{2.34}$$

No tensile strength has been considered in this study as a conservative assumption for risk assessment.

2.6 Geomechanical implication for risk potential due to overpressure

Figure 2.12a presents the temporal evolution of the failure indicator F_s with respect to the averaged fluid pressure (Figure 2.12b) on a cohesionless interface at the point just next to the injection site. The failure indicator is inversely proportional to the averaged fluid pressure, as explained previously. As Δp_f increases sharply after starting the injection, $\tau_{threshold}$ is reduced as the Mohr circle translates toward to the failure line while τ_{max} remains constant because of the constant radius of Mohr circle (undrained condition), significantly reducing the failure indicator. Following the minimum value, the indicator begins to increase as the averaged fluid pressure decreases.

The influence of the friction angle on the failure indicator is important, as shown in Figure 2.12a. For a friction angle of 30°, the failure indicator is initially equal to 2.0 and drops to 1.1 after two days of injection. This reduction of 0.9 leads the interface to the threshold of triggering failure. If a friction angle of 20° is considered, the failure indicator decreases from 1.4 to 0.8, whereas it drops by 0.4 for a friction angle of 15°. The magnitude of reduction is clearly proportional to the friction angle, indicating that an aquifer-caprock

interface with a high friction angle may also lose its integrity easily in response to a high overpressure. For these three friction angles, 30° can be considered as a minimum to avoid possible local failures.

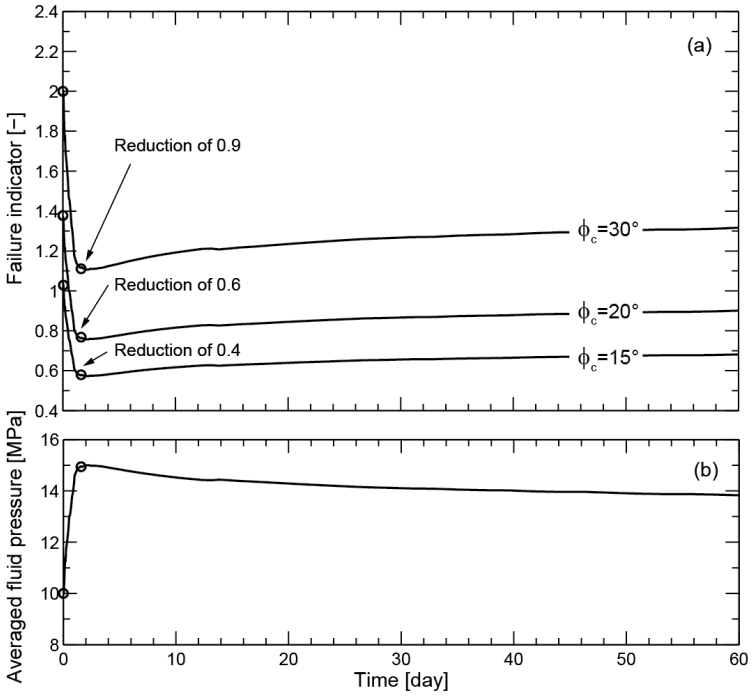

Figure 2.12. Influence of the friction angle on the failure indicator at the point next to the injection well on the interface between the caprock and aquifer

K_0 controls the ratio between the initial effective horizontal and vertical stresses. Thus, this factor defines the radius of the initial Mohr circle and is believed to have an important influence on the failure indicator. As shown in Figure 2.13, three different K_0 values are assumed for the interface of a friction angle of 15°. A high value of K_0 protects the interface from failures because a higher K_0 results in a smaller radius of the Mohr circle, resulting in a reduced $\tau_{\max}$. Additionally, the centre of the Mohr circle moves farther away, and the distance from the centre to the failure line $\tau_{\text{threshold}}$ increases. The failure indicator, defined as the ratio $\tau_{threshold}/\tau_{\max}$, rises significantly.

The effects of the aquifer's intrinsic permeability k on the failure indicator and average fluid pressure are given in Figure 2.14. k is a major factor that limits the fluid pressure accumulation because it controls the velocity of pressure dissipation. The failure indicator is proportional to the intrinsic permeability of the aquifer, as shown in Figure 2.14a. For

the considered low friction angle of 15°, a *k* that is one order of magnitude larger brings the failure indicator curve back from unfavourable conditions.

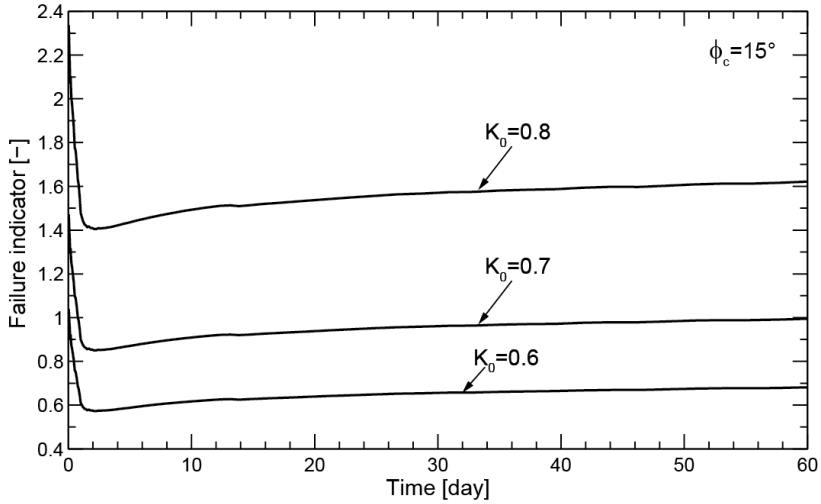

Figure 2.13. Influence of K_0 on the failure indicator at the point next to the injection well at the interface between the caprock and aquifer

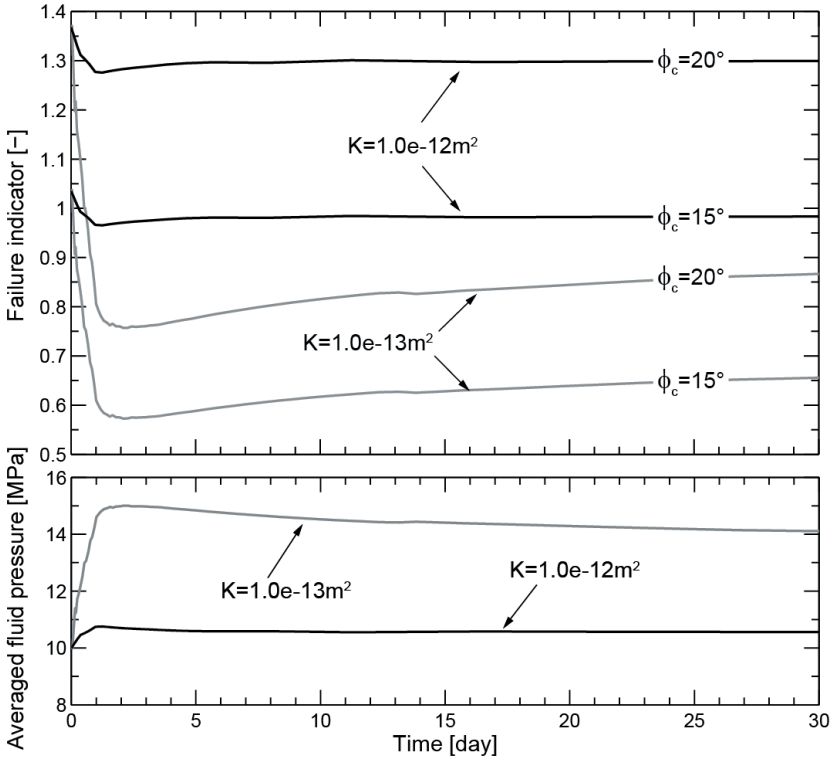

Figure 2.14. (a) Influence of the intrinsic permeability of the aquifer on the failure indicator at the point next to the injection well on the interface between the caprock and aquifer; (b) averaged fluid pressure response to the injection into the aquifer with two different intrinsic permeabilities.

Prior to the high rate of CO_2 injection, a desired value of the failure indicator will be established to avoid compromising the reservoir integrity under overpressure and to ensure the reliability of the project design, which is often mandated by law or regulation. To achieve this factor of safety, the properties of the sealing caprock and aquifer must be evaluated for suitability of the reservoir for CO_2 storage. Figure 2.15 presents the minimum friction angles of the caprock required to attain a given failure indicator F_s along the interface, which is calculated inversely according to Eq. (2.31). The curves in grey denote the spatial distributions of the minimum friction angle needed to attain $F_s = 1.0$ at different times of injection, which have the same behaviour as the averaged fluid pressure indicated in Figure 2.15a. These curves are enveloped by a black curve (Envelope $F_s = 1.0$), which represents the maximum value of the calculated minimum friction angles for the first 30 days after the beginning of injection. A minimum angle of 27° is required next to the injection well to attain $F_s = 1.0$. Moreover, this angle decreases with distance, as expected, toward $\phi = 14°$ at the boundary of the simulated domain. If a higher failure indicator is desired, such as $F_s = 1.2$, the minimum value next to the injection well is 33°, which is 6° higher. The minimum value at the boundary requires 18° instead of 14.5°. The friction angle rises rapidly in response to the increase in the requirement level for the failure indicator. A friction angle greater than 35° can be easily exceeded if $F_s = 1.0$ is employed as an objective failure indicator.

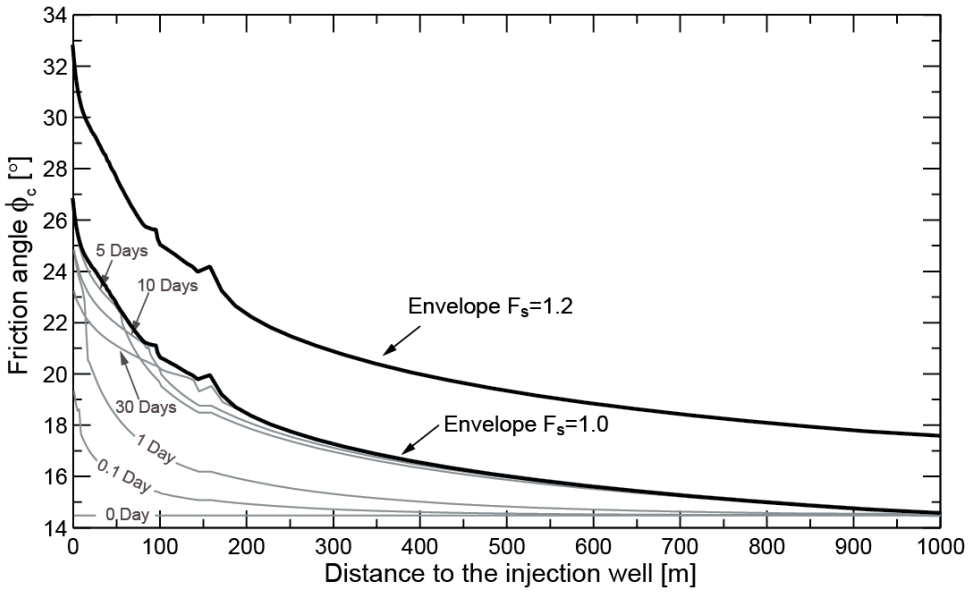

Figure 2.15. Minimum friction angle envelope restricted by the required failure indicator as a function of the distance from the injection well along the interface between the caprock and aquifer for the first 30 days of injection

Both K_0 and intrinsic permeability k have significant effects on the fluid pressure accumulation. Figure 16 presents the envelopes of these two parameters for an objective failure indicator $F_s = 1.0$. A K_0 value of 0.5 requires a friction angle of up to 40° to maintain a minimum safety condition if a permeability of 1×10^{-13} m^2 is considered. Fortunately, a small increase in K_0 results in a strong decrease in the minimum friction angle required. For example, if K_0 increases from 0.5 to 0.7, the minimum friction angle can be 23° less to maintain $F_s = 1.0$. Thus, an investigation of K_0 is important during the design of a CO_2 storage project. A high-permeability aquifer is favourable to avoid the accumulation of fluid pressure. As shown in Figure 2.16, the required minimum friction angle remains in the same range along the entire distance to the injection well for an intrinsic permeability 1×10^{-12} m^2. The angle in the vicinity of the injection well is 1-2° greater than that in other locations.

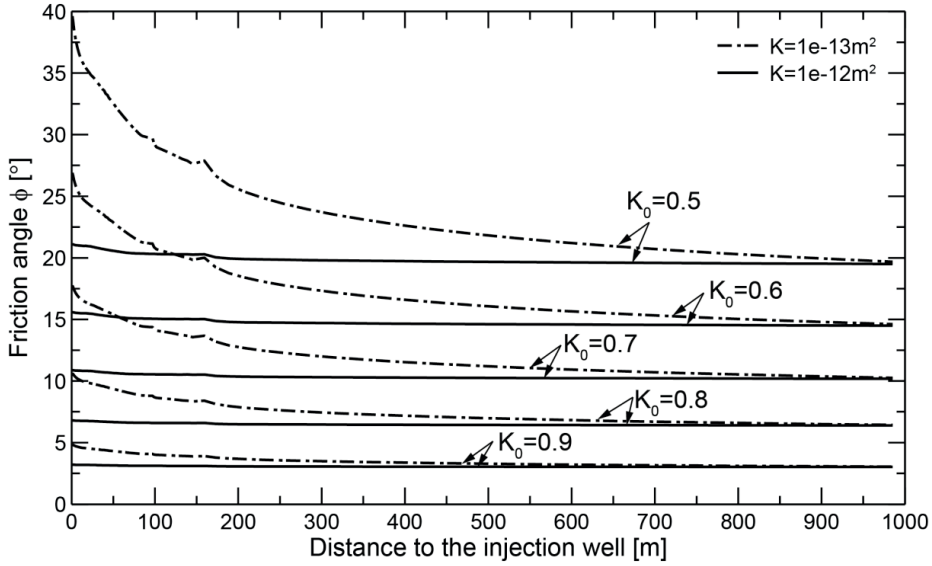

Figure 2.16. Influence of the intrinsic permeability and initial stress factor K_0 on the envelopes of the failure indicator Fs=1 along the interface between the caprock and aquifer for the first 30 days of injection

2.7 Conclusion

To address the hydromechanical processes applicable to CO_2 injection in a reservoir, a theoretical framework has been established and applied to a numerical analysis of a conceptual CO_2 reservoir. It has been shown that geomechanical instabilities originate from the fluid pressure accumulation within the aquifer and occur in the near field of the injection well. Injection-induced overpressure has been evaluated in terms of its impact on the aquifer-caprock interface, where potential failures may be triggered and may compromise sealing efficiency. The following conclusions can be drawn from the analyses:

- When CO_2 injection begins, the fluid pressure increases, which results in important hydromechanical changes in the injection zone. The overpressure decreases as the water becomes desaturated. The pressure accumulation propagates along the aquifer as the injection continues.
- Low-rate injection significantly reduces the fluid pressure accumulation within the aquifer. However, a high target rate is typically defined for a commercial CO_2 injection project. Increasing the injection rate to the target rate over time can limit the overpressure development within the aquifer. However, the effect is minor if the duration of increases in the injection rate is short. Therefore, for a given

reservoir, the target value of the injection rate dominates the maximum magnitude of overpressure.

- The most significant hydromechanical processes occur in the vicinity of the injection well. The plastic zone is located at the top of the aquifer next to the injection well, where material damage may occur.
- Tensile failures are not likely to occur for the case study considered and with the selected parameters. Shear failures along the aquifer-caprock interface are synthesised via a minimum friction angle for a desired local failure indicator. The minimum friction angle increases significantly as a higher failure indicator is required. The zone in the vicinity of the injection well is subjected to a high potential failures if the material is with a low friction. This observation suggests enhancement of the material properties or limitations on the overpressure.
- The permeability of the aquifer and the initial anisotropy stress factor K_0 are key parameters for pressure management, which play crucial role of the impact on the geomechanical instability during injection. An aquifer with a low friction angle can host a high injectivity without a high failure potential if the medium is with a high permeability (which dissipates overpressure rapidly) and a high value of K_0 (which reduces the shearing potential).

3 A hydromechanical approach to assess CO_2 injection-induced surface uplift and caprock deflection

3.1 Introduction

The combustion of oil, natural gas and coal accounts for approximately 80% of the world's energy and releases approximately 30 billion tonnes of carbon dioxide (CO_2) per year into the atmosphere (Reichle et al., 1999). The increased emission of CO_2 and resulting greenhouse effect have been implicated in global warming (Bryant, 1997). Geological sequestration of CO_2 is a technology to mitigate the amount of carbon dioxide, in accordance with the Kyoto Protocol, entering the atmosphere by capturing and storing the CO_2 from industrial emissions. This technology thus enables the continued use of fossil fuels. Deep saline aquifers are considered the most suitable geological formations for CO_2 storage because of their large capacity to trap CO_2 (Bachu, 2000; De Silva and Ranjith, 2012).

High rate (>1 Mt/year) injection of CO_2 into an aquifer results in an abrupt fluid pressure build-up, disturbing the stress state and generating deformations within the injection area. These hydromechanical variations spread both laterally and vertically. Induced deformation may propagate to the surface (Ringrose et al., 2013) and cause surface uplift. Ground deformation of up to 7 mm/year has been measured around each of the three injection wells at the In Salah project, Algeria, the largest onshore CO_2 storage project in the world (Onuma and Ohkawa, 2009; Vasco et al., 2008). These geomechanical issues have become a public concern and a research and industry interest for future reservoir integrity design and risk assessment of CO_2 storage projects.

Relying on representative geometries, many studies use computational approaches (finite difference, finite volume and finite element) to study this hydromechanical coupled behaviour (Preisig and Prévost, 2011; Rohmer and Seyedi, 2010; Rutqvist et al., 2010; Vilarrasa et al., 2010b). Although these approaches can address the problem, significant efforts and costs are required to construct numerical models for each potential candidate site and for uncertainty studies of geometric, geological and material parameters. Analytical solutions or semi-analytical approaches may be more suitable because of their computational efficiency and ability to identify driving mechanisms. Due to the complexity of the hydromechanical coupling effects and multiphase fluid interactions induced by CO_2 injection, most current analytical and semi-analytical approaches study only fluid flow problems in reservoirs (Dentz and Tartakovsky, 2008; Mathias et al., 2008; Nordbotten et al., 2005; Saripalli and McGrail, 2002; Vilarrasa et al., 2010a; Zeidouni et al., 2009; Zhou

et al., 2008) or simplified hydro-mechanical problems that may lose their forecasting capacity and reliability for the geomechanical analysis of CO_2 injection due to certain model assumptions, as described below.

Rutqvist (2012) estimated the surface uplift at In Salah using a simplified analytical solution according to Fjar (2008). The estimate is within the correct order of magnitude but has an overestimation of more than 50%. Various assumptions restrict the applicability of this solution, such as the consideration of a unique layered reservoir, 1-dimensional geometry and a uniformly distributed and constant injection-induced overpressure. Other advanced semi-analytical approaches can consider more complex geometries and additional mechanical mechanisms, such as multi-layered reservoirs and the effect of the bending moment between layers (Geertsma, 1973; Selvadurai, 2009, 2008). Nevertheless, these solutions only consider a flat, constant and fixed pressure as a loading variable. The injection-induced effects on the temporal and spatial evolution of the overpressure and of the reservoir deformation are thus omitted.

To provide a contribution to the pioneer works of Selvadurai (2009, 2008) and Rutqvist (2012), we propose a novel semi-analytical approach to overcome the former limitations. Based on a representative geometry for CO_2 storage, the proposed approach assesses the spatial and temporal surface uplift and caprock deformation caused by CO_2 pressurization and evaluates critical parameters for project design and risk management, including injection rate, permeability of the aquifer, thickness of the caprock, location of the injection zone and mechanical properties of the reservoir. We first derive a mathematical model to calculate the caprock and surface deformation caused by an arbitrary pressurization within the injection zone; this model extends the embedded plate approach proposed by Selvadurai (Selvadurai, 2009, 2008). This is followed by the incorporation of injection-induced overpressure distribution functions originating from two analytical solutions proposed by Nordbotten et al. (Nordbotten et al., 2005) and Dentz and Tartakovsky (Dentz and Tartakovsky, 2008). After mathematical integration, the analytical modelling produces two semi-analytical solutions that can address CO_2 injection-induced effects on the geomechanical behaviour of the reservoir. Such solutions have not been derived previously. A comparison with a finite element approach is then proposed to evaluate the performance of the semi-analytical solutions, followed by a parametric study to illustrate how such solutions can be applied to examine the effects of the geometric and physical parameters

on caprock deformation. Finally, the developed solutions are benchmarked to the surface uplift problem at In Salah.

3.2 Caprock deformation due to pressurization

3.2.1 Model description

As shown in Figure 3.1, an axisymmetric system is proposed for a typical CO_2 storage problem. The system consists of an overburden region and a saturated storage unit with a primary caprock embedded in between. CO_2 is injected into an m-metre-thick target aquifer with a distance l to the primary caprock layer of h metres thick. The injection zone is confined by impermeable strata. Injection of CO_2 through a vertical injection well causes pressurization within the injection zone, resulting in caprock deformation. The pressurization vanishes in the direction radial to the position with a radius of influence R, at which the pressure equals the initial hydrostatic pressure. This radius of influence extends in the radial direction as injection continues and is therefore time-dependent. For caprock deformation, Selvadurai (2009, 2008) proposed an elastic solution in which the caprock is modelled as an embedded plate over a circular region of flat and constant pressurization. Based on his approach, we focus on the extension of the model to account for arbitrary pressurization distributions. The corresponding caprock deflection is derived from this pressure loading.

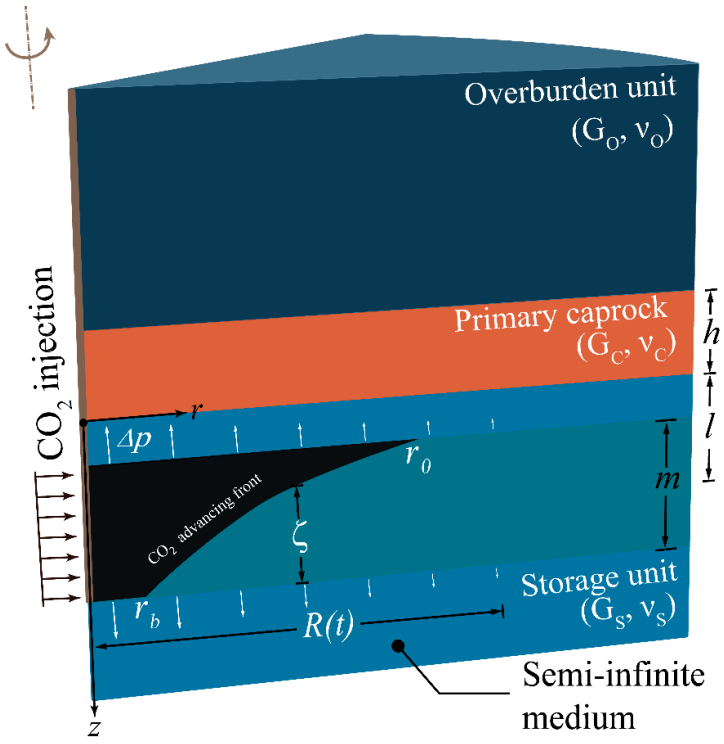

Figure 3.1. Idealized configuration of an embedded caprock layer.

3.2.2 Embedded plate approach

Selvadurai (2009, 2008) considered the caprock layer a thin plate embedded between the overburden region and the storage region. The overburden and storage regions are modelled as half-space regions. The assumption of a thin plate is justified by its thickness in relation to the dimensions (radius) of the pressurized zone. The interaction among the three units is caused by pressurization of a constant magnitude Δp applied over the entire injection zone.

The embedded caprock layer exhibits flexural behaviour that is governed by Germain-Poisson-Kirchhoff thin plate theory (Selvadurai, 2000). The governing equation employs polar coordinates with the Laplace operator $\tilde{\nabla}^2 = \frac{d^2}{dr^2} + \frac{1}{r}\frac{d}{dr}$:

$$D\tilde{\nabla}^2\tilde{\nabla}^2 w(r) + q^{(s)}(r) - q^{(o)}(r) = 0 \tag{3.1}$$

where the deflection *w(r)* is constrained by contact stresses $q^{(s)}(r)$ and $q^{(o)}(r)$, which are applied on the contact faces between the caprock and the respective regions. The flexural rigidity of the embedded caprock layer is expressed by $D\left(=G_c h^3/6(1-\nu_c)\right)$ with thickness

h of the caprock layer, shear modulus G_c and Poisson's ratio of the caprock ν_c. The pressurization of intensity Δp [Pa/m^3] is within the injection zone with a radius of influence R and thickness m located at a distance l from the interface between the caprock and the storage region. The caprock layer is assumed to be in bonded contact with the storage and overburden regions, for which the relevant kinematic interface conditions are as follows:

$$w(r,z=0)=u_z^{(s)q}(r,0)+u_z^{(s)p}(r,0)=u_z^{(o)q}(r,0) \tag{3.2}$$

$$u_r^{(s)}(r,z=0)=u_r^{(s)p}(r,0)=u_r^{(o)}(r,0)=0 \tag{3.3}$$

where u_r and u_z are, respectively, the radial and axial displacement in the polar coordinates, u^p is the displacement due to overpressure Δp, and u^q is the displacement constrained by contact stress q.

3.2.3 Mathematical solution

The Hankel integral transforms are used to for mathematical analysis of the interaction between caprock and surrounding geological layers induced by the CO2 injection. The Hankel transform expresses a given function *f* as the weighted sum of an infinite number of Bessel functions of the first kind J_α of order α. The Hankel transform of order α of a function *f* is defined as follows (with $\alpha \geq 0.5$):

$$\overline{F}_\alpha(k)=\int_0^\infty rf(r)J_\alpha(kr)dr, k\in\mathbb{R}^+ \tag{3.4}$$

and the inverse Hankel transform is given by the following:

$$f(r)=\int_0^\infty k\overline{F}_\alpha(k)J_\alpha(kr)dk, r\in\mathbb{R}^+ \tag{3.5}$$

where the Bessel function J_α denotes the solution of the canonical function solutions of the following equation:

$$x^2\frac{d^2y}{dx^2}+x\frac{dy}{dx}+(x^2-\alpha^2)y=0 \tag{3.6}$$

α is a real or complex number and refers to the order of the Bessel function. The Bessel functions of concern here are those that are finite at the origin (for an integer or positive α) and diverge as *x* approaches zero (for negative non-integer α); thus this solution is called

the Bessel function of the first kind of order α. It can be noted that the Hankel transform of order zero is essentially the two-dimensional Fourier transform in cylindrical coordinates.

3.2.4 Extension to arbitrary pressurization-induced deflection

We consider overpressure Δp not constant but time and space dependent. The caprock displacement due to an overpressure generation Δp of any form of distribution within the injection zone can be obtained with the aid of Green's function (Segall et al., 1994):

$$u_z^{(s)p}(r,0) = \frac{b}{G_s}\int_0^{\infty}\int_0^{\infty} \Delta p(\rho)\cdot g_z(r,z=0;\rho,d)\,\mathrm{d}\rho\,\mathrm{d}d \tag{3.7}$$

where b is the Biot coefficient of the storage unit and G_s is the shear modulus of the storage unit, and

$$g_z(r,z=0;\rho,d) = -(1-2\nu_s)\rho\int_0^{\infty}\xi J_0(\xi r)J_0(\xi\rho)e^{-\xi d}\,\mathrm{d}\xi \tag{3.8}$$

is Green's function, which corresponds to a ring of dilatation at radius $\rho \in [0,+\infty]$ and depth $d \in \left[l - m/2, l + m/2\right]$.

To introduce a pressure distribution, the integral of Eq.(3.7) is expressed as follows:

$$u_z^{(s)p}(r,0) = -\frac{(1-2\nu_s)bm}{G_s}\int_0^{\infty}\xi J_0(\xi r)e^{-\xi l}\int_0^{\infty}\rho\Delta p(\rho)J_0(\xi\rho)\mathrm{d}\rho\,\mathrm{d}\xi \tag{3.9}$$

Eq.(3.9) shows a linear relationship between the displacement and the material properties (i.e., $1/G_s$ and Poisson's ratio of the storage unit ν_s). The displacement induced by pressurization depends on the Bessel integral of the overpressure distribution $\Delta p(\rho)$. Evaluating $u_z^{(s)p}(r,0)$ with the zeroth-order Hankel transform gives the following:

$$\bar{u}_z^{(s)p}(\xi) = -\frac{(1-2\nu_s)bm}{G_s}\overline{\Delta p}(\xi)e^{-\xi l} \tag{3.10}$$

where $\overline{\Delta p}$ is the zeroth-order Hankel transform of Δp. This term yields the coupling term between pressurization and mechanical deflection.

The Green function of Eq. (3.8) used to develop Eq. (3.7) is the conventional solution for pressure increase or decrease in an elastic half-space due to fluid injection or reduction, respectively (Geertsma, 1973). Eq. (3.7) only represents the deformation of the caprock

due to the pressurization while the caprock is considered traction-free. The interactive mechanics between the caprock and adjacent layers are explicitly accounted by the constrains (more specifically, the bonding stresses) at the contact surfaces, that are induced by the plate flexural behaviour of the caprock. Selvadurai (2009) stated the displacement that was constrained by the bonding stresses:

$$\bar{u}_z^{(s)q}(r,0)=\frac{(3-4\nu_s)}{4G_s(1-\nu_s)}\frac{1}{\xi}\bar{q}^s(\xi) \tag{3.11}$$

$$\bar{u}_z^{(o)q}(r,0)=\frac{(3-4\nu_o)}{4G_o(1-\nu_o)}\frac{1}{\xi}\bar{q}^o(\xi) \tag{3.12}$$

Combining the kinematic constraint to which the storage region is subjected (Eq. (3.2)), the displacement induced by the pressurization (Eq.(3.10)) and the restricted deflection by the contact stress (Eq. (3.11)), we obtain the following equation after the zeroth-order Hankel transform:

$$\bar{q}^s(\xi)=\frac{4G_s(1-\nu_s)}{(3-4\nu_s)}\xi\bar{w}(\xi)+\frac{4(1-\nu_s)(1-2\nu_s)bm}{(3-4\nu_s)}\xi\overline{\Delta p}(\xi)e^{-\xi l} \tag{3.13}$$

Considering the kinematic constraints Eq.(3.2) and Eq.(3.12) on the storage region, we can obtain the following:

$$\bar{q}^o(\xi)=-\frac{4G_o(1-\nu_o)}{(3-4\nu_o)}\xi\bar{w}(\xi) \tag{3.14}$$

By evaluating the differential equation Eq.(3.1) with the zeroth-order Hankel transform:

$$D\xi^4\bar{w}(\xi)+\bar{q}^s(\xi)-\bar{q}^o(\xi)=0 \tag{3.15}$$

and introducing Eq.(3.13) and Eq.(3.14), we find the deflection of the caprock layer induced by an arbitrary radial pressurization after the inverse Hankel transformation:

$$w(r)=\frac{\Omega m}{h^2}\int_0^\infty\frac{\xi}{1+\Phi\xi^3}\overline{\Delta p}\left(\frac{\xi}{h}\right)e^{-\frac{\xi l}{h}}J_0\left(\frac{\xi r}{h}\right)d\xi \tag{3.16}$$

where Ω and Φ are constants that depend on the properties of the medium:

$$\Omega = \frac{\alpha_s (1-\nu_s)(1-2\nu_s)(3-4\nu_o)}{G_s (1-\nu_s)(3-4\nu_o) + G_o (1-\nu_o)(3-4\nu_s)} \tag{3.17}$$

$$\Phi = \frac{(3-4\nu_s)(3-4\nu_o)G_c}{24(1-\nu_c)\left[G_s (1-\nu_s)(3-4\nu_o) + G_o (1-\nu_o)(3-4\nu_s)\right]} \tag{3.18}$$

Eq.(3.16) extends the solution of Selvadurai (2009, 2008) to the case of a non-uniform distribution of overpressure and uses the Hankel transformation $\overline{\Delta p}$ to introduce any continuous overpressure evolution functions.

3.2.5 Mathematical approximation and validation

A necessary approximation for evaluating the integral of Eq. (3.7) is given by:

$$\int_{l-m/2}^{l+m/2} e^{-\xi d}\, \mathrm{d}\, d \approx m e^{-\xi l} \tag{3.19}$$

It is very common to employ this approximation in mathematics that comes from the fact that the hyperbolic sinus $\mathrm{sh}(x) \approx x$ for x sufficiently small. This approximation will lead to $\mathrm{sh}(\xi m/2) \approx \xi m/2$ here. However ξ goes from zero to infinity while m remains constant in this study, leading to a not viable approximation. This assumption has been employed in Geertsma (1973, 1966) and Segall, et al. (1994) and the approximated integration can be performed only for the case that the thickness of aquifer m is very small compared to its depth l to the caprock, being true in the application of surface subsidence due to depletion of a deep reservoir. Consequently, the assumption constrains the range of applications and is therefore not appropriate for the case in which the aquifer is situated just below or close to the caprock ($l = m/2$), a typical case for CO2 storage that is one of the objectives of this study. This assumption has not been addressed since its first appearance in Geertsma (1973) and it is necessary for deriving the next step of the mathematical formulation, its restriction must be verified. All integrals composing the $u_z^{(s)p}$ term must be examined.

For simplification and without loss of generality, we assume that the pressure is constant over radius R from the injection well (otherwise we can work with an inequality and the maximum pressure over the domain):

$$P(r,z)=\Delta p \ \text{if}\ d-\frac{t}{2}\le z\le d+\frac{t}{2}$$
$$P(r,z)=0 \quad \text{otherwise} \tag{3.20}$$

The exact integration of Eq. (3.7) can be expressed as:

$$u_z^{(s)p}(r,0)=-\frac{(1-2\nu_s)\alpha_s\Delta pmR}{G_s}\int_0^\infty J_0(kr)J_1(kR)\frac{2}{k}e^{-kl}sh\left(\frac{kt}{2}\right)dk\equiv u \tag{3.21}$$

If we perform the previous approximation, we obtain the same result as Eq.(10) in Segall, et al. (1994):

$$u_z^{(s)p}(r,0)=-\frac{(1-2\nu_s)\alpha_s\Delta pmR}{G_s}\int_0^\infty t\,J_0(kr)J_1(kR)e^{-kl}dk\equiv\tilde{u} \tag{3.22}$$

Setting $C=-\frac{(1-2\nu_s)\alpha_s\Delta pmR}{G_s}$, we obtain the difference of two integrals (3.21) and (3.22) as following:

$$(u-\tilde{u})(r)=C\int_0^\infty\left(\frac{2}{k}sh\left(\frac{kt}{2}\right)-t\right)J_0(kr)J_1(kR)e^{-kl}dk \tag{3.23}$$

We examine the behaviour of the integral Eq. (3.23) as a function of *r*, throughout the numerical computation. For the best computation, we propose following change of the variable:

$$\mathbb{R}^+\to[0;1[$$
$$\varphi: y\to argth(y)=\frac{1}{2}\ln\left(\frac{1-y}{1+y}\right) \tag{3.24}$$

which leads,

$$(u-\tilde{u})(r)=-C\int_0^\infty\left\{\left(\frac{2}{argth(y)}sh\left(\frac{argth(y)t}{2}\right)-t\right)\right.$$
$$\left.\times J_0(argth(y)r)J_1(argth(y)R)e^{-argth(y)l}\frac{y}{1-y^2}\right\}dy \tag{3.25}$$

Figure 3.2 illustrates the integral difference of Eq. (3.25) that represents the mathematical error if performing the approximation. We observe that the difference is very small

(approximately 10^{-13}) compared to the value of u or $\tilde{u}$ (approximately 10^{-3}~10^{-2}). The influence of the relationship between l and m on Green's function is demonstrated not significant because of the decaying behaviour of the multiplication of two Bessel functions in Eq.(3.8). In conclusion, the consequence of this assumption on the physical interpretation can be neglected, and its benefit to the mathematical derivation still holds.

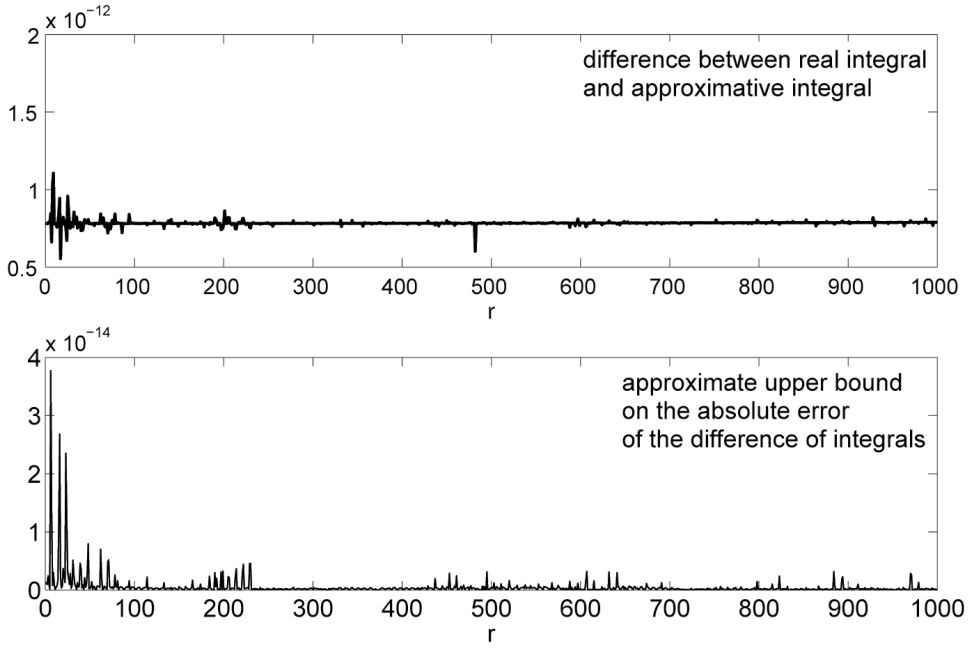

Figure 3.2. Error estimation of the approximation employed in the development

3.3 Caprock deflection induced by CO_2 injection

To determine the deflection *w(r)* according to Eq.(3.16), the overpressure distribution $\overline{\Delta p}$ must be allocated to describe the distribution of centres of pressurization. Selvadurai (2009, 2008) considers a constant overpressure distributed within the injection zone. However, CO_2 injection results in a high concentration of overpressure around the injection well, and this overpressure vanishes with distance. This overpressure pattern is necessary to estimate the magnitude of the deformation more accurately and can be derived from two analytical solutions proposed by Nordbotten et al. (2005) and Dentz and Tartakovsky (2008), which describe the advancing abrupt interface between the injected CO_2 and the host water, which are assumed to be immiscible. As shown in Figure 1, the injection zone is divided into three

regions: (1) around the injection well, where only injected CO_2 exists ($r \le r_b$); (2) the intermediate region, where the two fluids coexist but are separated by a sharp interface ($r_b \le r \le r_0$); and (3) the outer region, where only host water exists ($r_0 \le r \le R$). The governing equation for the interface position is derived by Bear (1972):

$$\frac{1}{r}\frac{\partial}{\partial r}\left[\zeta \frac{Q_0 - 2\pi r(\rho_w - \rho_c) g (k/\mu_c)(m-\zeta)\partial\zeta/\partial r}{\zeta + (m-\zeta)\mu_w/\mu_c}\right] + 2\pi\phi\frac{\partial\zeta}{\partial t} = 0, \qquad (3.26)$$

where Q_0 is the volumetric flux rate of injected CO_2 and ζ denotes the vertical position of the interface between the two fluids. Both solutions (Nordbotten et al. (2005) and Dentz and Tartakovsky (2008)) are approximations of the exact solution of Eq.(3.26) but differ in the assumptions made for the approximation. Whereas Nordbotten et al. (2005) used an energy minimization approximation, Dentz and Tartakovsky (2008) applied the Dupuit assumption of horizontal flow. The development of the solutions is not detailed here; the reader is referred to the original works of Nordbotten et al. (2005) and Dentz and Tartakovsky (2008). In addition, the validity and the applicability of both solutions has been discussed in (Dentz and Tartakovsky, 2009; Lu et al., 2009; Vilarrasa et al., 2010a).

The interface solutions derived by Nordbotten et al. (2005), denoted by NB, and Dentz and Tartakovsky (2008), denoted by DZ, are written as follows:

$$\zeta_{NB}(r,t) = m\left[1 - \frac{\mu_c}{\mu_w - \mu_c}\left(\sqrt{\frac{\mu_w Q_0 t}{\mu_c \phi \pi m r^2}} - 1\right)\right] \qquad (3.27)$$

$$\zeta_{DZ}(r,t) = \frac{Q_0}{2\pi k m g}\frac{\mu_w - \mu_c}{\rho_w - \rho_c}\ln\left(\frac{r}{r_{b,DZ}(t)}\right) \qquad (3.28)$$

where $r_b(t)$ is the radius at which the interface intersects the lower domain boundary and is determined by the volume conservation (Dentz and Tartakovsky (2008)):

$$r_{b,DZ}(t) = 2\sqrt{\frac{tkmg(\rho_w - \rho_c)}{\phi(\mu_w - \mu_c)}\left[\exp\left(\frac{4\pi k m^2 g(\rho_w - \rho_c)}{Q_0(\mu_w - \mu_c)}\right) - 1\right]^{-1}} \qquad (3.29)$$

We further account for the pressure-dependent CO_2 density and viscosity according to Peng and Robinson (1976) and Fenghour et al. (1998), respectively, through the iterative

methodology proposed by Vilarrasa et al. (2010a). Inserting interface Eq.(3.27) and Eq.(3.28) into the integration of Darcy's law results in the derivation of two vertically averaged overpressure expressions with the zeroth-order Hankel transformation. The transformed expressions are substituted into the mechanical deflection Eq. (3.16), which leads to two hydromechanical solutions, the Li-Selvadurai-Nordbotten solution, denoted by LI-SN, and the Li-Selvadurai-Dentz solution, denoted by LI-SD, as shown below. Both solutions permit the analysis of the interaction between the caprock and surrounding regions that are subjected to CO_2 injection-induced pressurization.

$$
\begin{aligned}
w(r)_{LI-SN} = \frac{\Omega m}{h^2}\int_0^{\infty}\frac{\xi e^{-\frac{\xi l}{h}}}{1+\Phi\xi^3}\Bigg\{ & \frac{Ah^2}{\xi^2}\left[y\ln\left(\frac{yh}{\xi R}\right)J_1(y)+J_0(y)\right]_{\xi R/h}^{\xi r_0/h} \\
& +A\left(\ln\left(\frac{R}{r_0}\right)+Br_0\right)\frac{r_0J_1\left(\xi r_0/h\right)-r_bJ_1\left(\xi r_b/h\right)}{\xi/h} \\
& -AB\int_{r_b}^{r_0} r^2J_0(\xi r/h)dr \\
& +\frac{ACh^2}{\xi^2}\left[y\ln\left(\frac{yh}{\xi r_b}\right)J_1(y)+J_0(y)\right]_{\xi r_b/h}^{\xi r_w/h} \\
& +A\left(\ln\left(\frac{R}{r_0}\right)+B\left(r_0-r_b\right)\right)\times \\
& \frac{r_bJ_1\left(\xi r_b/h\right)-r_wJ_1\left(\xi r_w/h\right)}{\xi/h}\Bigg\}J_0\left(\frac{\xi r}{h}\right)d\xi
\end{aligned}
\tag{3.30}
$$

with parameters $A=\dfrac{Q_0\mu_w}{2\pi km}$; $B=\sqrt{\dfrac{\mu_c\phi\pi m}{\mu_w V(t)}}$; $C=\dfrac{\mu_c}{\mu_w}$ and $R=\sqrt{\dfrac{2.25k\rho_w gt}{\mu_w S_s}}$.

$$
\begin{aligned}
w(r)_{LI-SD} = \frac{\Omega m}{h^2}\int_0^{\infty}\frac{\xi e^{-\frac{\xi l}{h}} A}{\left(1+\Phi\xi^3\right)\mu_w}\Bigg\{&\frac{\mu_w h^2}{\xi^2}\left[y\ln\left(\frac{yh}{\xi R}\right)J_1(y)+J_0(y)\right]_{\xi R/h}^{\xi r_0/h}\\
&+\hat{B}\frac{r_0 J_1(\xi r_0/h)-r_w J_1(\xi r_w/h)}{\xi/h}\\
&+\frac{\mu_c h^2}{\xi^2}\left[y\ln(\frac{yh}{r_b\xi})J_1(y)+J_0(y)\right]_{\xi r_0/h}^{\xi r_w/h}\\
&+\hat{C}\int_{r_b}^{r_0} r\ln(\frac{r}{r_b})\ln(\frac{r_b}{r})J_0\left(\frac{\xi r}{h}\right)dr\Bigg\}J_0\left(\frac{\xi r}{h}\right)d\xi
\end{aligned}
\tag{3.31}
$$

and parameters $\hat{B}=\mu_w\ln\left(\frac{R}{r_b}\right)-\frac{\mu_w-\mu_c}{2\gamma};\hat{C}=\frac{(\mu_w-\mu_c)\gamma}{2}$ where $\gamma=\frac{Q_0(\mu_w-\mu_c)}{2\pi km^2 g(\rho_w-\rho_c)}$.

3.4 Numerical evaluation of Bessel integrals

Matlab® is used to compute the infinite integral of the proposed two semi-analytical solutions numerically. The adaptive Gauss-Kronrod quadrature formula is chosen to confront with the oscillatory nature of Bessel integral because it represents the highest efficiency for high accuracies and oscillatory integrands (Shampine, 2008). Most of the integrals appeared in the development can be performed with suitable quadrature. However the computation of $\int_{r_b}^{r_0} r\ln\left(\frac{r_b}{r}\right)\ln\left(\frac{r}{r_b}\right)J_0(\xi r/h)dr$ in the solution LI-SD requires unreasonable number of intervals to be performed. Looking into the nature of the function *F* that is to be integrated,

$$
F: x\mapsto x\ln\left(\frac{x}{a}\right)\ln\left(\frac{a}{x}\right)J_0\left(\xi x\right),\ \left(a,\xi\right)\in\left(\mathbb{R}^{+*}\right)^2 \tag{3.32}
$$

We show a graphic representation of the function *F* in Figure 3.3. It can be noticed that the function *F* is a highly oscillatory function of which amplitude decreases extremely slowly to infinity with ***xi*** (ξ) increasing. For this reason, computing this integral with the chosen formula is often inaccurate and requires large number of intervals and time for calculation.

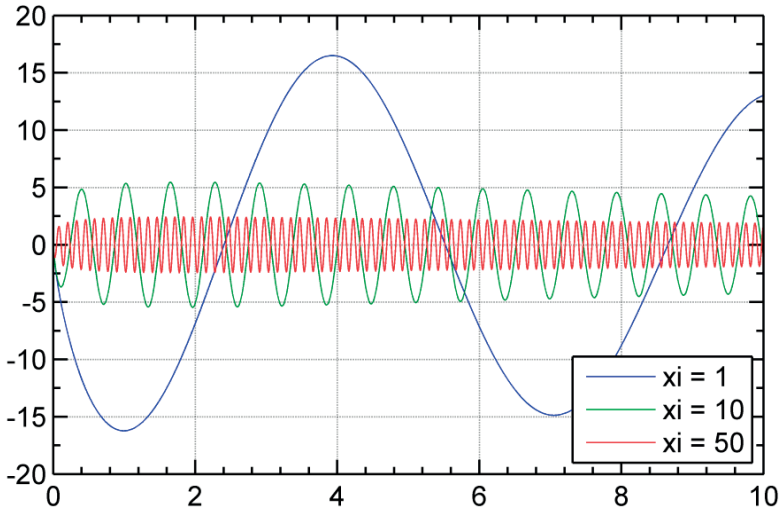

Figure 3.3. Graphic representation of function Eq. (3.32). *a=100* is used.

A stabilization transform is thus proposed as follows:

$$\int_c^d r\ln\left(\frac{a}{r}\right)\ln\left(\frac{r}{a}\right)J_0(\xi r)\,dr = \frac{1}{\xi^2}\left[\ln\left(\frac{r}{a}\right)\left(rln\left(\frac{a}{r}\right)J_1(\xi r) - 2J_0(\xi r)\right)\right]_c^d + \frac{2}{\xi^2}\int_c^d \frac{J_0(\xi r)}{r}\,dr \tag{3.33}$$

As can be seen that we have to compute the integral $\int_c^d \frac{J_0(\xi r)}{r}\,dr$ in which $\frac{J_0(\xi r)}{r}$ displays a less oscillatory nature as illustrated in the Figure 3.4. It decreases very fast to infinity and the oscillation vanishes after several periods so that the calculus of the integral is more accurate when employing the right hand-side term of the equality of Eq. (3.33). To give an idea, we perform numerical integration with 650 integration points (default value of Matlab), for $a = 100; \xi = 1000$ over an integral region of [100, 500], we obtain the integral result of -3.1467 with an error bound around 40 for the non-stabilization scheme, whereas the result for the stabilization scheme is -0.0012 with an approximated error bound of 10^{-4}. To achieve the same error bound, 48000 points is necessary for the quadrature over this small integral region.

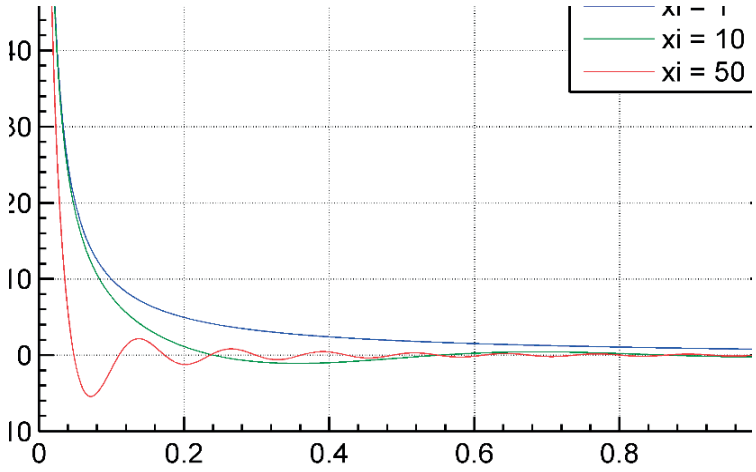

Figure 3.4 Graphic representation of function $\frac{J_0(\xi r)}{r}$

3.5 Model verification

The two semi-analytical solutions Eq.(3.30) and Eq.(3.31) are applied to a CO_2 storage injection problem to evaluate their performance in comparison with a numerical solution. The semi-analytical modelling described above assumes an elastic plate-like caprock and two immiscible fluids separated by an abrupt interface, whereas the numerical model considers poroelasticity and two miscible fluids with a capillary effect. The intent of the developed semi-analytical approach is to provide a straightforward and efficient tool for examining the material sensitivity and geometric uncertainty. However, comparing the semi-analytical and numerical approaches can facilitate the assessment of the relevancy of our approximations.

3.5.1 Finite element numerical model

A typical CO_2 storage model in an axisymmetric configuration is proposed, and the mesh for the numerical model is shown in Figure 3.5. CO_2 is injected into a 100-m-thick aquifer at 100 kg/s through a vertical well of the radius $r_w = 0.15\text{m}$. The aquifer is situated 900 m underground and is overlaid by a 100-m-thick impermeable caprock. The numerical model is set at 10 km to approach the infinite-acting aquifer of the analytical solution, and hydrostatic pressure and fixed displacement are applied on the outer boundary. The mechanical and hydraulic properties are given in Table 3.2. The nonlinear finite element FEM code Lagamine (Collin, 2003) is used to solve the problem numerically.

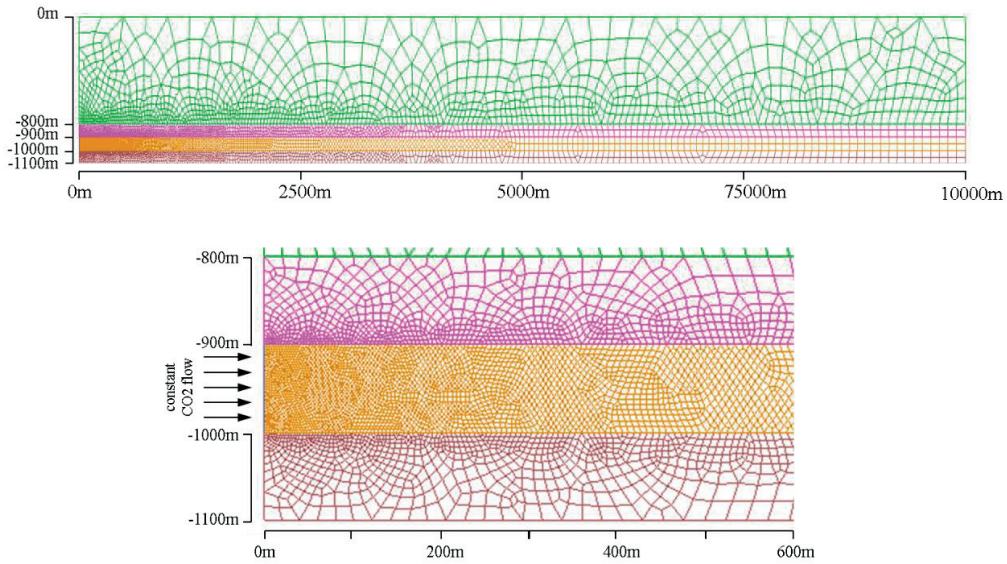

Figure 3.5. Numerical model mesh used for simulation. Details in the vicinity of the well are magnified.

The materials involved in the problem are porous media, which are treated as a mixture consisting of a solid matrix, water and CO_2 phases according to the theory of mixtures (Bowen, 1982) which is implemented by Collin et al. (2003) in the nonlinear finite element code Lagamine (2011). The code is used to solve the mass conservation equations for water, w, and CO_2, c and the momentum equation. In the following, a brief summary of the coupled system is introduced to solve for the displacement of solid matrix $\boldsymbol{u}$, water pressure p_w and CO_2 pressure p_c.

The mass conservation equations are written for water and CO_2:

$$\frac{\partial\left(nS_\alpha\rho_\alpha\right)}{\partial t}+\mathbf{div}\left(\rho_\alpha\mathbf{q}_\alpha\right)=0\,;\,\alpha=c,w \tag{3.34}$$

where n is the porosity, S_α is the degree of saturation of the α-phase, ρ_α is the density and $\mathbf{f}_{\boldsymbol{\alpha}}$ is the velocity of the α-fluid, which is defined by the generalized Darcy's law for porous media:

$$\mathbf{q}_\alpha=\frac{kk_{r,\alpha}}{\mu_\alpha}\left(\mathbf{grad}\left(p_\alpha\right)+\rho_\alpha\mathbf{g}\right) \tag{3.35}$$

in which μ_α is the dynamic viscosity of α phase, k is the intrinsic permeability of the reservoir rock, $k_{r,\alpha}$ is the relative permeability of the α-fluid and p_α is the α fluid pressure.

A van Genuchten function (van Genuchten, 1980) is used to describe the retention behaviour of the reservoir rock:

$$S_w = \left(1 + \left(s / P_r\right)^{1/(1-m)}\right)^{-m} \tag{3.36}$$

where λ and P_0 are a material parameter and a reference pressure, respectively, and s is the matrix suction or capillary pressure defined as the difference between CO_2 and water pressure, $s = p_c - p_w$. A linear function for relative permeability is used:

$$k_\alpha = S_\alpha \tag{3.37}$$

The momentum equation is written as follows:

$$\operatorname{div}(\boldsymbol{\sigma}) + \rho \mathbf{g} = 0 \tag{3.38}$$

where ρ is the density of the mixture, which is defined as follows:

$$\rho = (1-n)\rho_s + nS_w\rho_w + n(1-S_w)\rho_c \tag{3.39}$$

and the total stress $\boldsymbol{\sigma}$ can be decomposed through a combination of the generalized effective stress tensor $\boldsymbol{\sigma}'$, water pressure p_w and CO2 pressure p_c:

$$\boldsymbol{\sigma}' = \boldsymbol{\sigma} - p_c\mathbf{I} + S_w(p_c - p_w)\mathbf{I} \tag{3.40}$$

All materials are considered linear elastic. The stress-strain relationship is described below:

$$\mathrm{d}\boldsymbol{\varepsilon} = \mathbf{E}^{-1}\,\mathrm{d}\boldsymbol{\sigma}' \tag{3.41}$$

where $\mathbf{E}$ is the elastic tensor and $d\boldsymbol{\varepsilon}$ is the strain tensor increment, and the strain is defined as $\boldsymbol{\varepsilon} = 1/2\,(\nabla\mathbf{u} + \nabla^{\mathrm{T}}\mathbf{u})$.

Table 3.1. Parameter values used in the numerical experiments

Analytical model	Overburden unit	Storage unit	Caprock layer
Shear modulus *Go, Gs, Gc* [GPa]	1	10	5
Poisson's ratio v_0, v_s, v_c [-]	0.25	0.25	0.25
Porosity in the injection zone ϕ [-]		0.15	-
Permeability in the injection zone k [m^2]		1.0e-13	-
Thickness of the caprock m [m]		100	
Distance from the caprock to the middle of the injection zone l [m]		50	
Well radius r_w [m]		0.15	
Injection rate Q_m [kg/s]		100	

Numerical model	Retention curve	Relative permeability
van Genuchten*	$S_w = \left(1+\left(s/P_0\right)^{1/(1-m)}\right)^{-m}$ $P_0 = 0.02$ MPa & $m = 0.8$	$k_\alpha = S_\alpha$ $\alpha = CO_2; water$
CO_2 density	Peng and Robinson (Peng and Robinson, 1976)	
CO_2 viscosity	Fenghour et al. (Fenghour et al., 1998)	

*Linear relative permeabilities and a van Genucheten retention curve parameter are set to approximate the abrupt interface approach (Vilarrasa et al., 2010a)

3.5.2 Comparison between numerical and analytical predictions

The analytical versus numerical results are presented in Figure 3.6 and Figure 3.7 for the overpressure and caprock deflection distribution, respectively. The numerical results exhibit a slightly higher overpressure generation near the well field. This higher overpressure generation can be explained by the neglect of the capillary effect in semi-analytical approaches, which lowers the energy needed for CO_2 injection into the saturated aquifer. Furthermore, the numerical model describes a lower caprock deflection around the well. Because the coupling effect is relatively strong around the well, the poroelasticity theory in the numerical model allows more energy dissipation than the embedded plate approach in the semi-analytical method. Differences in the curvature of the deflection shape are also observed because the overpressure decreases logarithmically with distance in the LI-SD solution but linearly in the LI-SN solution. However, the differences remain subtle. Both the overpressure and deflection calculated by the numerical approach are, on average, in good agreement with the analytical results.

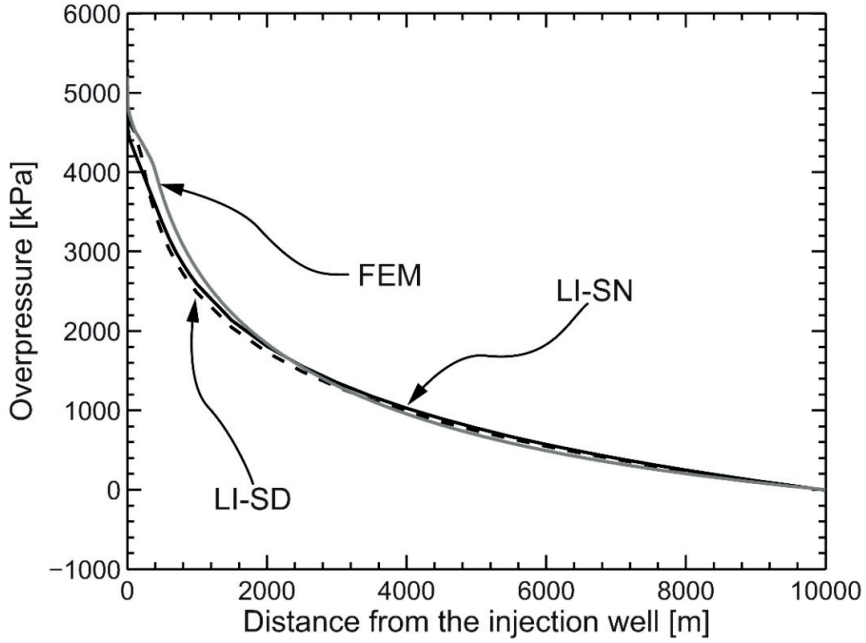

Figure 3.6. Spatial distribution of the vertically averaged overpressure after 100 days of injection with the reference parameters.

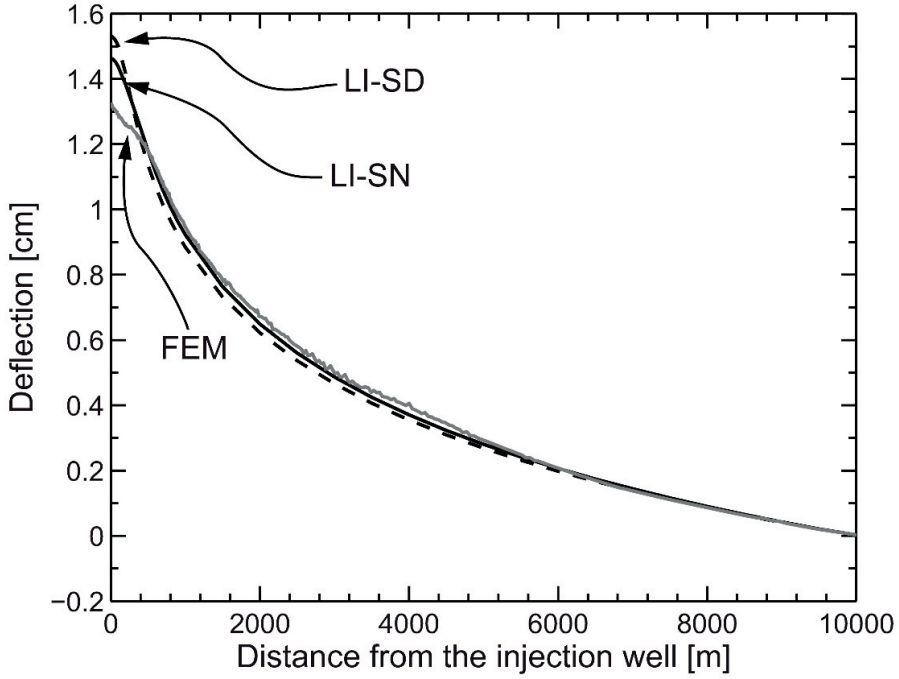

Figure 3.7. Spatial distribution of the deflection of the caprock after 100 days of injection with the reference parameters.

3.6 Parametric studies

Based on the CO_2 storage problem described above, the effects of the geometric and the material parameters on the caprock deflection are studied. Figure 3.8 shows the relationship between the deflection of the caprock and the distance to the injection zone. The magnitude of the overpressure decreases when the distance l is increased. The CO_2 density increases as the hydrostatic pressure increases with depth; thus, for a given mass of injected CO_2, the injected volume decreases and less overpressure accumulates. Because the estimated overpressure at the injection well is higher when using the LI-SD solution compared to the LI-SN solution, a higher overpressure is obtained with the LI-SD solution with a nearly constant difference in magnitude. The thickness of the zone between the caprock and the injection zone limits strain propagation from the injection zone to the caprock. Hence, the difference in the magnitude of deflection at the caprock vanishes with distance l, whereas the difference in the overpressure remains nearly constant (see Figure 3.9). The effect of the overpressure difference is most significant when both layers are adjacent and becomes negligible when l=400 m, suggesting that injection of CO_2 at a certain distance from the primary caprock can reduce the strain within the caprock and further reduce the possibility of fissuring and cracking.

The temporal evolution of the caprock deflection is shown in Figure 3.10 with various permeabilities. At a constant rate of injection, the fluid pressure increases significantly at the beginning of the injection period. As a consequence of the elastic model, the deflection reflects the effect of overpressure and exhibits the same behaviour. The deflection increases gradually after one year of injection and reaches a maximum. The deflection is nearly proportional to the inverse of the permeability (see Eq.(3.30) and Eq.(3.31)). Thus, the permeability can be considered an important factor in limiting overpressure accumulation and subsequent deflection.

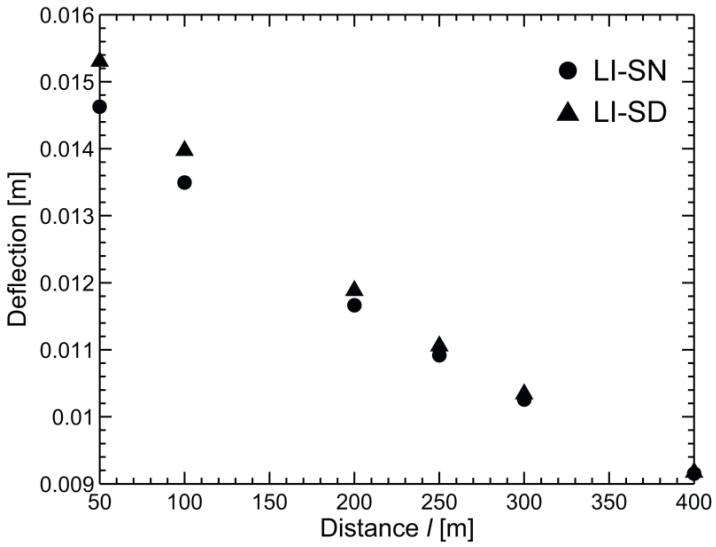

Figure 3.8. Maximum deflection calculated after 100 days of injection at different distances *l* from the interface between the caprock and the aquifer.

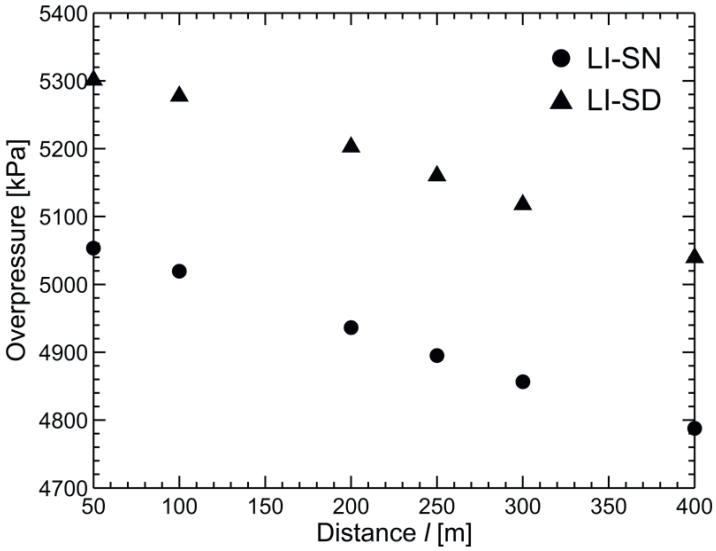

Figure 3.9. Vertically averaged overpressure at the injection well after 100 days of injection at different distances *l* from the interface between the caprock and the aquifer.

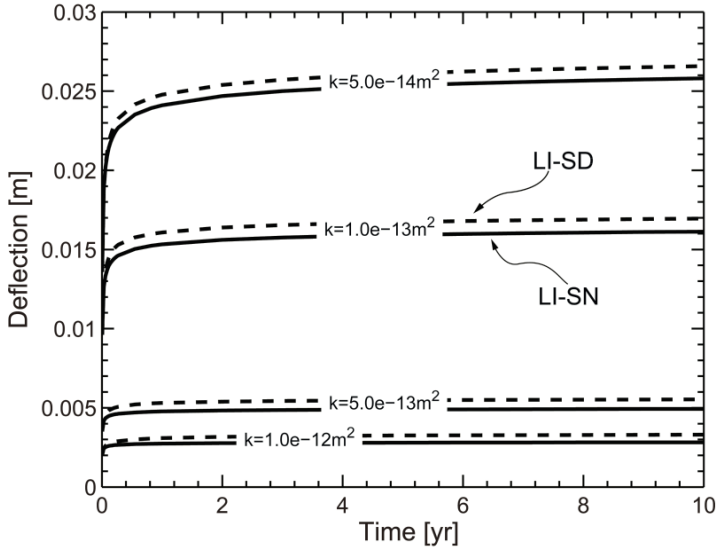

Figure 3.10. Deflection at the injection well with time with variation in permeability.

3.7 Benchmark to the case of the In Salah project

At In Salah, ground deformation was detected around three CO_2 injection wells by satellite imaging (Bohloli et al., 2012; Onuma and Ohkawa, 2009; Vasco et al., 2008). Because highly accurate measurements are available, the surface heave at In Salah is considered an ideal benchmark problem for geomechanical modelling. Using these data, Rutqvist, et al. (2010) and Presig and Prévost (2011) investigated the surface uplift around injection well KB501 using 3D and 2D numerical models, respectively. The results are in good agreement with the field measurements. Here, we apply our semi-analytical solutions to the same data set used by Rutqvist, et al. (2010) to assess the same problem. Instead of a three-dimensional analysis, we perform our analytical modelling in a 2D axisymmetric configuration. Due to the geometrical constraint of the semi-analytical solutions, horizontal well KB501 is simplified to a vertical well. We assume that this simplification is valid because the approximately 70-km^2 area influenced by the injection is large compared to the 2-m-long well (Onuma and Ohkawa, 2009). In addition, because the aquifer is very thin (20 m in thickness), the injection-induced pressurization forms a bulb-like pressure zone that covers the entire well and extends in the radial direction, as observed in Rutqvist, et al. (2010).

As shown in Figure 3.11, the model consists of a 900-m-thick surface layer, 900-m-thick impermeable caprock and a 20-m-thick aquifer where CO2 is to be injected at a rate of approximately 8 kg/s. The material properties of the injection zone are presented in Table 3.2.

Table 3.2. Material parameters used in the simulation of the In Salah uplift

Parameter	Unit	Caprock	Surface
Shear modulus	GPa	8.35	0.625
Poisson's ratio	-	0.2	0.2
Porosity in the injection zone	-	0.17	
Permeability in the injection zone	m^2	1.3e-14	

Figure 3.12 compares the results of the semi-analytical solutions and the actual measurements for the three-year injection. Both semi-analytical solutions indicate an approximately 7-mm surface uplift after the first two years, consistent with the detected surface uplift, but underestimate the uplift in the third year. The computed results of Rutqvist et al. (2010) are the same order of magnitude as the measurement in the third year, but the uplift during the first two years is underestimated. A bell-shaped uplift form is observed, as shown in Figure 3.13. The spatial pattern of surface uplift is consistent with the uplift spread computed by Presig and Prévost (2011) and the satellite imagery presented in Onuma and Ohkawa (2009) and Bohloli, et al. (2012).

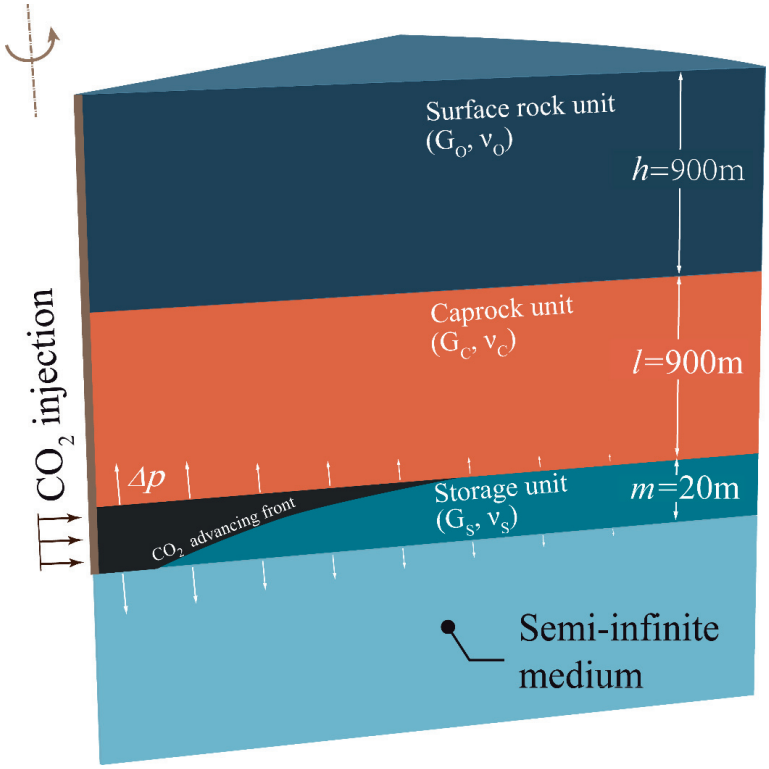

Figure 3.11. Geometry of the model used to simulate the surface uplift around injection well KB501 at In Salah

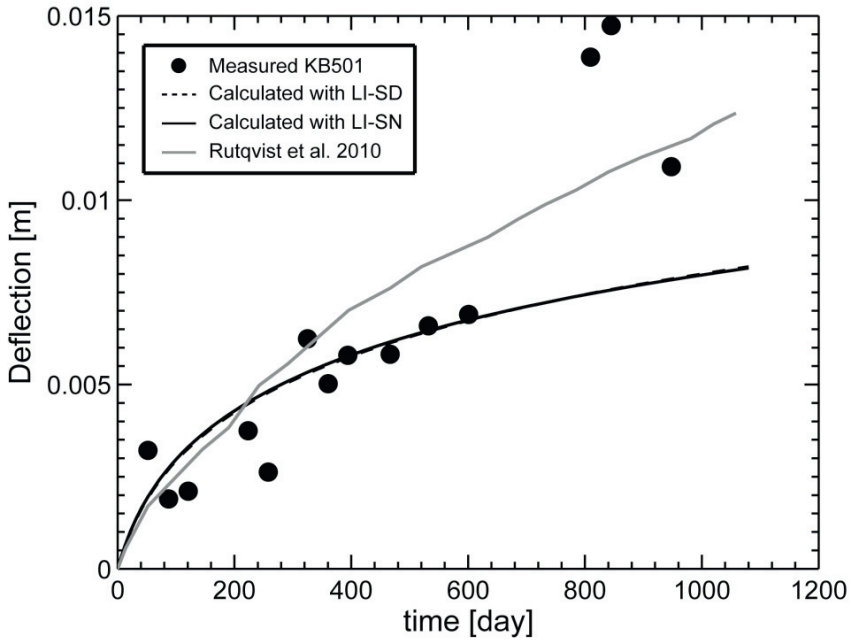

Figure 3.12. Comparison of the calculated temporal surface uplift to the measured ground uplift over well KB501 and the numerical result calculated by Rutqvist et al. (2010).

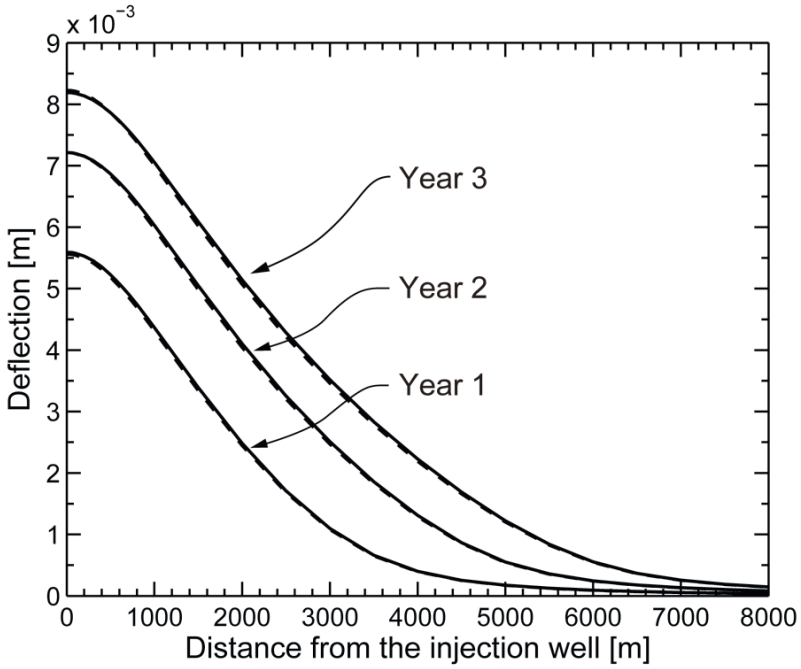

Figure 3.13. Calculated surface uplift over well KB501.

3.8 Conclusion

The injection of CO_2 pressurizes the reservoir and causes caprock deflection, which further results in surface uplift. A semi-analytical approach was developed to predict the temporal and spatial deformation level of the caprock and the surface. The approach assumes linear elastic materials, the caprock as a thin-plate, an abrupt CO_2-water interface and no capillary forces. In developing the analytical model, we accounted for an arbitrary pressurization distribution within the injection zone, followed by a mathematical formulation of caprock deflection subjected to such pressure loading. Next, we incorporated two overpressure distribution functions to address the CO_2 injection-induced pressurization. After including the pressure-dependent CO_2 density and viscosity, the mathematical modelling led to two closed-form analytical expressions to address the mechanical interaction between the primary caprock and adjacent regions that are affected by the CO_2 injection-induced pressurization.

The developed solutions were applied to a representative CO_2 storage case that was solved numerically by the finite element method. The analytical results match the numerical simulation results, demonstrating the relevancy of the approximations and assumptions

implemented in the development. Parametric studies were undertaken to illustrate the influence of factors such as geometry, overpressure magnitude and material properties on the caprock deflection. Finally, we benchmarked the developed semi-analytical solutions to assess the surface uplift observed at In Salah. Good agreement in the temporal and spatial evolution was observed between the measurements and the calculated results.

The advantage of using a semi-analytical approach is that it offers a convenient and efficient way to assess the impact of various factors and material parameters on the safety of CO_2 injection projects. In view of the computational approaches, the developed semi-analytical approach is an alternative and cost-effective calculation tool for candidate site evaluation and sensitivity analysis. In addition, the development within here is straightforward. Other fluid injection-induced pressurization distribution functions can be incorporated into the mechanical part. Thus, this model can integrate advances in hydrology research and be extended to any fluid injection problem.

4 Coupled multiphase thermo-hydro-mechanical analysis of supercritical CO_2 injection: benchmark for the In Salah surface uplift problem

4.1 Introduction

In the fight against climate change, Carbon Capture and Storage (CCS) is seen as one of the key mitigation options to reduce our CO_2 emissions into the atmosphere. There are several examples of large-scale CCS projects throughout the world such as In Salah, Algeria; Snøhvit, Norway; Sleipner, Norway; and Gorgon, Australia (IPCC, 2005). Carbon emissions in the form of CO_2 are collected before injecting under high pressures into a deep geological aquifer, tripped by a sealing caprock for long-term storage. Fluid injection-induced high pressure is particularly prone to the reservoir stability, which has been observed in reservoir industries for a long history (Ferronato et al., 2010; Gaus, 2010; Nuth et al., 2010; Ringrose et al., 2013; Teatini et al., 2011). The high injection rate of massive CO_2, the fully saturated host reservoir, and the nearly impermeable caprock confer on the host aquifer a sudden increase in pressure. The overpressure causes substantial volumetric expansion of the reservoir, resulting in noticeable surface deformation (Li et al., 2015; Rutqvist et al., 2008), seismicity (Nicol et al., 2011; Oye et al., 2012; Vilarrasa and Carrera, 2015; Zoback and Gorelick, 2012) as well as fault reactivation at near and far field (Cappa and Rutqvist, 2011; Rinaldi and Rutqvist, 2013). The CO_2 to be injected is usually colder than the aquifer temperature (Bissell et al., 2011). The cooling can lead to contractive volumetric deformations and noticeable shear deformation if a high contrast in temperature persists (Preisig and Prévost, 2011). CCS is an emerging technology and is expected to expand in the near future, which raises the need to better understand these coupled mechanisms of geological repositories when subjected to CO_2 injection. In view of the large spatial-temporal scale and the involved complex physical coupling processes, numerical simulation is considered as the most appropriate way to enable improved evaluation of suitable locations, by allowing accurate capacity assessment, and control of the injection pressure to ensure that fracturing of the sealing caprock does not occur.

Since the 2000s, some attempts have been made to validate geomechanical models with available surface movement measurements at In Salah to study the relative importance of the hydraulic properties of the reservoir and injection rate. The modelling framework and the involved physical complexity differ from one study to another for fluid injection-induced reservoir deformations as reviewed by Jiang (2011). In the majority of cases (André et al., 2009; Fang et al., 2013; Guy et al., 2010; Li et al., 2005; Rutqvist et al., 2008, 2007; Schäfer et al., 2012; Shi et al., 2012; Vidal-gilbert et al., 2009), fluid flow is solved first, and the mechanical aspects of reservoir are either not considered or are treated in a

sequential hydromechanically coupled manner. However, the difference in simulation results between sequentially and fully coupled coupling schemes can be very high if the coupled effects are strong, as reported by Prévost (2013). The most viable way to capture the coupled effects requires the fully coupled solution of deformation, temperature and pressure equations. Nevertheless, results of recent development in fully coupled simulation (Preisig and Prévost, 2011; Vilarrasa et al., 2015) show contradictory behaviour for a similar model set-up, which may be due to the different assumptions made in each development as well as in the numerical implementation schemes.

In this chapter, a new thermal-hydro-mechanical THM fully coupled continuum modelling approach is introduced that is suitable for the study of various coupled physical processes in deep geological formations subjected to multiphase CO_2 injection. Because its implementation is performed in a fully coupled way, the properties of CO_2 in the gas, liquid and supercritical states such as the density and viscosity have a direct impact on the THM coupled mechanisms. The capacity of this development to analyse and quantify the coupled multiphase fluid flow, thermal flow and deformation processes in CO_2 injection is demonstrated with field measurements, using a THM CO_2 injection finite element simulation. The analysis is performed with a two-dimensional, finite element model aimed at reproducing the surface uplift observed at the In Salah CO_2 storage site. The injection lasts approximately four and a half years from 2004 until 2009, during which time the surface uplift was monitored. This is a unique benchmark to be assessed (Class et al., 2009). Instead of adapting the material parameters to match the numerical results of the surface movement history, we perform a blind prediction of the surface uplift based upon the newest available experimental evidence, as well as the best available hydrogeological and geomechanical data. The goal is to evaluate the simulation performance with comparison to the observed surface displacements and extract the novel insights on the fluid flow and mechanical deformation. To the best of our knowledge, this study presents so far the most detailed, fully coupled model for geomechanical assessment of CO_2 storage problem.

4.2 Thermodynamic analysis of CO_2

Under standard atmospheric conditions, CO_2 is considered as an ideal gas with a density of 1.872 kg/m^3. The injected CO_2 is usually under much higher pressure and temperature than the critical state of CO_2 at $T_c = 31.1$ °C and $P_c = 7.4$ MPa, where T and P are the temperature

and pressure, respectively, and the subscript '*c*' denotes the critical point as illustrated in Figure 4.1. Above this critical pressure and temperature, CO_2 is at a fluid state called the supercritical state of which CO_2 is like a gas but with the density of a liquid. The perfect gas assumption does not hold for this fluid state.

CO_2 is usually injected at a pressure higher than the in-situ pore pressure and a temperature colder than the in-situ temperature (Lu and Connell, 2008). At In Salah, the pre-injection pore pressure is approximately 19 MPa, and an in-situ temperature is approximately 90 °C (Morris et al., 2011). The injection pressure of approximately 25 MPa has been monitored (Bohloli et al., 2012) and the temperature at the bottom hole is estimated at 50 °C (Bissell et al., 2011). At both environmental and injection conditions, CO_2 is at the supercritical state of which the thermodynamic properties must be derived and included in the development to account for the real behaviour of the CO_2 fluid.

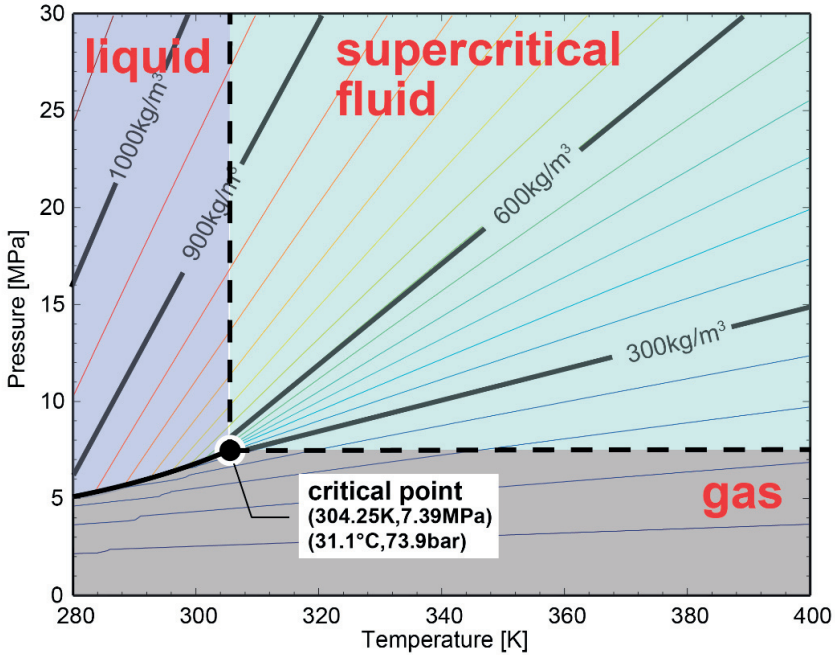

Figure 4.1 CO_2 density and phases diagram.

4.2.1 Specific enthalpy and heat capacity

For a system at pressure *P* and temperature *T*, enthalpy *H* is given by:

$$H = U + PV \tag{4.1}$$

where U is the internal energy of the system, and V is the volume of CO_2. Differentiating Eq. (4.1) with respect to volume at constant temperature, one can obtain

$$\left(\frac{\partial H}{\partial V}\right)_T = \left(\frac{\partial U}{\partial V}\right)_T + \left(\frac{\partial (PV)}{\partial V}\right)_T \tag{4.2}$$

with

$$dU = TdS - PdV \tag{4.3}$$

where S is the entropy of the system. By differentiating Eq. (4.3) also with respect to volume at constant temperature, one can obtain

$$\left(\frac{\partial U}{\partial V}\right)_T = T\left(\frac{\partial S}{\partial V}\right)_T - P \tag{4.4}$$

With the Maxwell relationship, the following equality is obtained:

$$\left(\frac{\partial S}{\partial V}\right)_T = \left(\frac{\partial P}{\partial T}\right)_V \tag{4.5}$$

Combining Eq. (4.2) - (4.5) gives:

$$\left(\frac{\partial H}{\partial V}\right)_T = T\left(\frac{\partial P}{\partial T}\right)_V - P + \left(\frac{\partial (PV)}{\partial V}\right)_T \tag{4.6}$$

We can then integrate Eq. (4.6) to obtain the enthalpy changes between state 1 and state 2:

$$H_2 - H_1 = \int_{v_1}^{v_2} \left[T\left(\frac{\partial P}{\partial T}\right)_V - P \right] dV + (PV)_2 - (PV)_1 \tag{4.7}$$

The equation of state (EOS) by Peng and Robinson (1976) is used to describe the relation between state variables P, V and T at the gas, liquid and supercritical states of CO_2:

$$P = \frac{RT}{V-b} - \frac{a}{V(V+b)+b(V-b)} \tag{4.8}$$

If we consider state 2 as the state of interest and state 1 as an ideal gas state at zero pressure in Eq. (4.7), one can obtain the enthalpy of CO_2 by introducing Eq. (4.8) as:

$$H = RT\left(Z-1\right)-\frac{\sqrt{2}a}{4b}\left[1+\frac{\kappa T}{\sqrt{\alpha T T_c}}\right]\ln\left(\frac{Z+\left(1+\sqrt{2}\right)B}{Z+\left(1-\sqrt{2}\right)B}\right)+H_{ideal} \tag{4.9}$$

where R is the gas constant, $a = a(\alpha, \kappa, T_c), b, \alpha$ and κ are the Peng and Robinson EOS parameters and $B = \frac{bP}{RT}$. Z is the fluid compressibility factor of CO_2 defined as $Z = \frac{PV}{RT}$, which is pressure- and temperature-dependent as detailed in Appendix 1. The ideal gas enthalpy H_{ideal} is given by Span and Wagner (1996):

$$H_{ideal} = RT\left(1+\tau\cdot\phi^0\right) \tag{4.10}$$

where τ is the inverse reduced temperature $\left(\tau = \frac{T_c}{T}\right)$, and ϕ^0 is the dimensionless Helmholtz energy for an ideal gas. Combing Eq. (4.9) and Eq. (4.10) gives the pressure- and temperature-dependent specific enthalpy of CO_2 at all fluid states:

$$h_c = \frac{1}{M_C}\left(Z+\frac{T_c}{T}\phi^0\right)-\frac{\sqrt{2}a}{4bM_C}\left[1+\frac{\kappa T}{\sqrt{\alpha T T_c}}\right]\ln\left(\frac{Z+\left(1+\sqrt{2}\right)B}{Z+\left(1-\sqrt{2}\right)B}\right) \tag{4.11}$$

where M_c is the CO_2 molar weight.

The specific heat capacity $c_{p,c}$ can also be determined by differentiating Eq. (4.9) with respect to temperature at constant pressure:

$$\begin{aligned} c_{p,c} = \left(\frac{\partial h}{\partial T}\right)_P = \frac{d^2a}{dT^2}.\frac{T}{2\sqrt{2}\cdot b\cdot M_c}.\ln\left[\frac{Z+\left(\sqrt{2}+1\right)B}{Z+\left(1-\sqrt{2}\right)B}\right] \\ +\frac{R\left(M-N\right)^2 M_c^{-1}}{M^2-2.A\left(Z+B\right)}-\frac{R}{M_c}+\frac{C_{p,ideal}}{M_c} \end{aligned} \tag{4.12}$$

where $A = \frac{a.p}{R^2.T^2}$, $M = \frac{Z^2+2.B.Z-B^2}{Z-B}$ and $N = \frac{da}{dT}\frac{B}{bR}$. $C_{p,ideal}$ represents heat capacity of an ideal gas that follows the temperature-dependent formula proposed by Reid et al. (2000):

$$C_{p,ideal} = 27+1.13\times10^{-2}T+1.3\times10^{-4}T^2-2.0\times10^{-7}T^3+8.8\times10^{-11}T^4 \tag{4.13}$$

Both the specific heat enthalpy and capacity of CO_2 are illustrated in Figure 4.2.

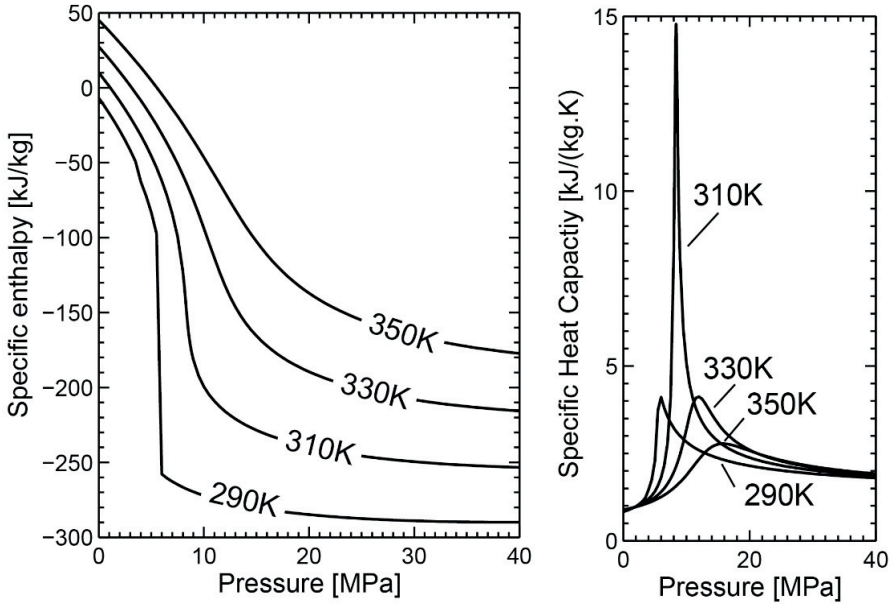

Figure 4.2 CO_2 specific enthalpy and heat capacity

4.2.2 Joule-Thomson effect

The temperature of CO_2 will increase or decrease during an adiabatic expansion or compression, which is termed the Joule-Thomson effect. Adiabatic cooling may also be encountered in CO_2 storage due to free expansion of the injected CO_2 in the pores (Han et al., 2010; Mukhopadhyay et al., 2011; Oldenburg, 2007), especially in the depleted gas reservoir (Giorgis et al., 2007) and inside the injection well (Lu and Connell, 2008). This phenomenon can be illustrated by the Joule-Thomson coefficient, which is defined as the ratio of temperature variation ΔT to pressure variation ΔP at constant enthalpy conditions. It can be determined by the thermodynamic relationships of Eq.(4.9) and (4.12):

$$\mu_{JT} = \lim_{\Delta P \to 0}\left(\frac{\Delta T}{\Delta P}\right)_H = \left(\frac{\partial T}{\partial P}\right)_H ; \mu_{JT} = -\left(\frac{\partial H}{\partial P}\right)_H \left(\frac{1}{C_p}\right) \tag{4.14}$$

Figure 4.3 shows the contour of the μ_{JT} values. The line where μ_{JT} is equal to zero represents the Joule-Thomson inversion curve. Suitable conditions for CO_2 storage lie on the left of the inversion curve. In this zone, μ_{JT} is positive and generally increases as P and T decrease. CO_2 heats upon compression and cools upon expansion. The Joule-Thomson effect is included in the development.

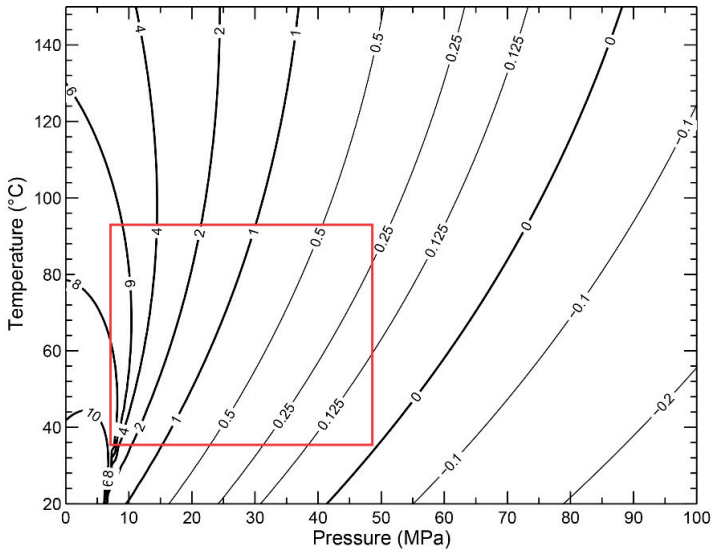

Figure 4.3 Diagram of the Joule-Thomson coefficient μ_{JT}. The box represents suitable conditions for CO_2 storage.

4.3 Thermal-hydro-mechanical coupled modelling framework

4.3.1 Mass balance

The compositional approach is employed and implemented for water and perfect gas in the finite element code *Lagamine* (Collin, 2003; Gerard et al., 2008). This approach has the advantage of writing the mass balance equation for two-phase fluids in a straightforward manner. Based on the current formulation, we extend the framework to account for the supercritical fluid properties, including terms for the storage of both CO_2 and water in the liquid and gaseous form, the advective flow of both fluids, and the non-advective flow of the dissolved CO_2 in water. Water phase pressure p_w, CO_2 phase pressure p_c, temperature T and solid displacement field $\boldsymbol{u}$ are chosen as the primary state variables that describe the state of the material. The mass balance equations and fluid flows are expressed in the moving current configuration using a Lagrangian updated formulation (Charlier et al., 2011), through which the solid mass is automatically conserved for a reference elementary volume V:

$$\frac{d\left((1-n)\rho_s\right)}{dt}=0 \tag{4.15}$$

where t is time, n is the porosity and ρ_s is the solid density. The density variation is following the equation of state that is adapted from Lewis and Schrefler (1998):

$$\frac{1}{\rho_s}\frac{d\rho_s}{dt}=\frac{1}{1-n}\left[\frac{(b-n)}{K_s}\frac{\partial}{\partial t}\left(S_w p_w+(1-S_w)p_c\right)-3(b-n)\alpha_s\frac{\partial T}{\partial t}-(1-b)\mathbf{div}\left(\frac{\partial \mathbf{u}}{\partial t}\right)\right] \tag{4.16}$$

where b is the Biot coefficient, K_s is the bulk modulus of the solid matrix and α_s is the linear thermal expansion coefficient for the solid. The water phase saturation S_w is a function of the capillary pressure (suction) s, which is defined as the difference between the CO_2 phase and the water phase pressures $s = P_c - P_w$. The relationship between the saturation and suction will be given hereafter. Introducing Eq. (4.16) into Eq. (4.15), the solid mass balance equation is then expressed in terms of the variation of the porosity by the primary state variables:

$$\frac{dn}{dt}=(b-n)\left[\frac{1}{K_s}\frac{\partial}{\partial t}\left(S_w p_w+(1-S_w)p_c\right)-3\alpha_s\frac{\partial T}{\partial t}+\mathbf{div}\left(\frac{\partial \mathbf{u}}{\partial t}\right)\right] \tag{4.17}$$

This equation defines the coupling between the geomechanics and thermo-hydraulics. The change in porosity is explicitly shown as proportional to three terms, (a) a volumetrically weighted fluid pressure $P_f = S_w P_w + (1 - S_w)P_w$, (b) temperature and (c) the matrix volumetric deformation. That the Biot coefficient plays a dominant role in terms of the porosity variation.

The mass balance equation for the *water specie* and *CO_2 specie* are written respectively, as:

$$\underbrace{\frac{\partial\left(nS_w\rho_w\right)}{\partial t}+\mathbf{div}\left(\rho_w\mathbf{q}_w\right)}_{\text{liquid water}}=0 \tag{4.18}$$

$$\underbrace{\frac{\partial\left(n(1-S_w)\rho_c\right)}{\partial t}+\mathbf{div}\left(\rho_c\mathbf{q}_c\right)}_{\text{superitical/liquid CO}_2}+\underbrace{\frac{\partial\left(nS_w\rho_{dc}\right)}{\partial t}+\mathbf{div}\left(\rho_{dc}\mathbf{q}_w\right)+\mathbf{div}\left(\mathbf{i}_{dc}\right)}_{\text{dissolved CO}_2\text{ in the water}}=0 \tag{4.19}$$

Assuming that the dissolution of CO_2 in the water is accounted for, but no water dissolution in CO_2 is involved, therefore there is one more component in the mass balance of the *CO_2 specie,* i.e. Eq. (4.19) than in that of the water, i.e. Eq. (4.18). It can also be noted that the

mass exchange associated with the dissolution is not visible in Eq. (4.19) as a consequence of employment of the compositional approach.

Among these terms, the liquid water and supercritical/liquid CO_2 flow $\mathbf{q}_w$ and $\mathbf{q}_c$ are governed by the generalised Darcy's law for porous media to determine the advective flow:

$$\mathbf{q}_{w,c} = -\frac{\mathbf{k}k_{rw,rc}}{\mu_{w,c}}\left[\mathbf{grad}\left(p_{w,c}\right) + \rho_{w,c}\mathbf{g}\right] \tag{4.20}$$

where $\mathbf{k}$ is the intrinsic permeability tensor and k_{rw} amd k_{rc} are water and CO_2 relative permeabilities, which are geomaterial-dependent parameters. μ_w is the dynamic viscosity of water which is calculated according to Thomas and King (1994) and μ_w is the dynamic viscosity of CO_2 which is following the relationship of Fenghour et al. (1998), which is valid for the range of temperatures and pressures considered here.

Liquid water is considered as a compressible and dilatant fluid, of which the exponential relationship for the density ρ_w definition is:

$$\begin{aligned} &\rho_w = \rho_{w0}\exp\left[\kappa_T(p_w - p_{wr}) - \beta_w(T - T_r)\right] \\ &\frac{1}{\rho_w}\frac{\partial\rho_w}{\partial p_w} = \kappa_T \quad ; \quad -\frac{1}{\rho_w}\frac{\partial\rho_w}{\partial T} = \beta_w \end{aligned} \tag{4.21}$$

where ρ_{w0} is the reference density for a given salinity at reference pressure p_{wr} and reference temperatureT_r. κ_T is the isothermal water compressibility, β_w is the volumetric thermal expansion coefficient of water.

CO_2 involved in CO_2 storage cannot be considered as a perfect gas because of its high-pressure high-temperature condition. A compressibility factor Z is used to describe the deviation from the perfect gas density to a real gas as:

$$\rho_c = \frac{1}{Z}\frac{M_c}{R}\frac{p_c}{T} \quad ; \quad \frac{1}{\rho_c}\frac{\partial\rho_c}{\partial p_c} = \left(\frac{1}{p_c} - \frac{1}{Z}\frac{dZ}{dp_c}\right) \quad ; \quad \frac{1}{\rho_c}\frac{\partial\rho_c}{\partial T} = -\left(\frac{1}{T} + \frac{1}{Z}\frac{dZ}{dT}\right) \tag{4.22}$$

This factor Z is a pressure- and temperature-dependent parameter. The advantage of expressing the density change as a function of Z is that one can express the compressible behaviour of gaseous, liquid and supercritical CO_2 with appropriate equations of state (EOSs). In this study, factor Z is calculated through Peng and Robinson's EOS (Peng and

Robinson, 1976) due to its accuracy and computational efficiency (Böttcher et al., 2012b; Lin, 2008).

The Henry law, which describes the amount of a given perfect gas that dissolves in a volume of water, is extended for a real gas with gas fugacity (Pruess and García, 2002; Spycher and Reed, 1988) which is determined through Peng and Robinson's EOS as well:

$$\Phi\, p_c = K_{eq,g-l}^{co_2} X_{dc} \tag{4.23}$$

where $K_{eq,g-l}^{co_2}$ is a temperature-dependent Henry's constant determined according to Crovetto (1991), and X_{dc} is the mole fraction of dissolved CO_2 in water. Incorporating the relationship of Eq. (4.22), the dissolution amount can be represented by the dissolved mass in a unit volume of water as:

$$\rho_{dc} = \frac{\Phi Z \rho_w R T}{K_{eq,g-l}^{co_2} M_w} \rho_c \tag{4.24}$$

This relationship is used in the CO_2 diffusion law that is based on Fick's law in a tortuous medium:

$$\mathbf{i}_{dc} = -nS_w \tau D_c \rho_w \mathbf{grad}\left(\frac{\rho_{dc}}{\rho_w}\right) \tag{4.25}$$

where D_c is the diffusion coefficient of the dissolved CO_2 in the water phase and τ is the tortuosity of the porous media.

Accounting for the variation of porosity (Eq. (4.17)) and the compressible properties of water (Eq.(4.21)) leads to a coupled mass balance for solid and liquid water (Eq. (4.18)) as:

$$\begin{aligned}
\frac{\partial\left(nS_w\rho_w\right)}{\partial t} = \Bigg\{ & \left[-n\frac{\partial S_w}{\partial s} + nS_w\kappa_T + \frac{b-n}{K_s}S_w\left(S_w + \frac{\partial S_w}{\partial s}s\right)\right]\frac{\partial p_w}{\partial t} \\
& + \left[n\frac{\partial S_w}{\partial s} + \frac{b-n}{K_s}S_w\left(1 - S_w - \frac{\partial S_w}{\partial s}s\right)\right]\frac{\partial p_c}{\partial t} \\
& - \left[\left(\mathrm{b}-\mathrm{n}\right)S_w 3\alpha_s - nS_w\beta_w\right]\frac{\partial T}{\partial t} \\
& + bS_w\mathbf{div}\left(\frac{\partial \mathbf{u}}{\partial t}\right) \\
\mathbf{div}\left(\rho_w\mathbf{q}_w\right) = \Bigg\{ & + \mathbf{div}\left(-\frac{\mathbf{k}k_{rw}}{\mu_w}\left[\mathbf{grad}\left(p_w\right) + \rho_w\mathbf{g}\right]\right) = 0
\end{aligned} \tag{4.26}$$

The mass conservation of *CO_2 specie* (Eq. (4.19)) in a deformable medium is obtained by integrating Eq.(4.17) and Eq. (4.22):

$$
\begin{aligned}
&\frac{\partial\left(n\left(1-S_w\right)\rho_c\right)}{\partial t}+\frac{\partial\left(nS_w\rho_{dc}\right)}{\partial t} = \\
&\left\{\begin{array}{l}
\left\{\begin{array}{l} n\left(\rho_{dc}-\rho_c\right)\dfrac{\partial S_w}{\partial s}+nS_w\dfrac{\partial \rho_{dc}}{\partial p_c}+n\left(1-S_w\right)\rho_c\left(\dfrac{1}{p_c}-\dfrac{1}{Z}\dfrac{dZ}{dp_c}\right) \\ +\dfrac{\left(b-n\right)}{K_s}\left[S_w\rho_{dc}+\left(1-S_w\right)\rho_c\right]\left(1-S_w-s\dfrac{\partial S_w}{\partial s}\right) \end{array}\right\}\dfrac{\partial p_c}{\partial t} \\
+\left\{\begin{array}{l} \dfrac{\left(b-n\right)}{K_s}\cdot\left[S_w\rho_{dc}+\left(1-S_w\right)\rho_c\right]\left(S_w+s\cdot\partial\dfrac{\partial S_w}{\partial s}\right) \\ -n\left(\rho_{dc}-\rho_c\right)\dfrac{\partial S_w}{\partial s} \end{array}\right\}\dfrac{\partial p_w}{\partial t} \\
-\left\{\begin{array}{l} \left(b-n\right)3\alpha_s\left[\left(1-S_w\right)\rho_c+S_w\rho_{dc}\right]+nS_w\dfrac{\partial \rho_{dc}}{\partial T} \\ +\left(1-S_w\right)n\rho_c\left(\dfrac{1}{T}+\dfrac{1}{Z}\dfrac{dZ}{dT}\right) \end{array}\right\}\dfrac{\partial T}{\partial t} \\
+\left[S_w\rho_{dc}+\left(1-S_w\right)\rho_c\right]\cdot b\cdot\mathbf{div}\left(\dfrac{\partial \mathbf{u}}{\partial t}\right)
\end{array}\right. \\
&\mathbf{div}\left(\rho_{dc}\mathbf{q}_w\right)+\mathbf{div}\left(\mathbf{i}_{dc}\right) = \left\{\begin{array}{l} +\mathbf{div}\left(-\rho_{dc}\dfrac{\mathbf{k}k_{rw}}{\mu_w}\left[\mathbf{grad}\left(p_w\right)+\rho_w\mathbf{g}\right]\right) \\ -\mathbf{div}\left(nS_w\tau D_c\rho_w\mathbf{grad}\left(\dfrac{\rho_{dc}}{\rho_w}\right)\right) \end{array}\right. \\
&\mathbf{div}\left(\rho_c\mathbf{q}_c\right) = \left\{ +\mathbf{div}\left(-\rho_c\dfrac{\mathbf{k}k_{rc}}{\mu_c}\left[\mathbf{grad}\left(p_c\right)+\rho_c\mathbf{g}\right]\right)=0\right.
\end{aligned}
\tag{4.27}
$$

The mass balance equations Eq.(4.26) and Eq. (4.27) govern the coupled diffusion behaviour, in which the quantities $\mathbf{k}$, k_{rc}, k_{rw} and S_w are dependent on the geomaterial of a specific site and will be detailed in the section related to the model setup.

4.3.2 Energy balance

Assuming a thermal equilibrium, a unique temperature is defined for the mixture. The energy balance equation of the mixture has the following form

$$
\underbrace{\frac{\partial H_m}{\partial t}}_{\text{Heat storage}}+\underbrace{\underbrace{\mathbf{div}\left(\mathbf{\Gamma}\right)}_{\text{conduction}}+\underbrace{\mathbf{div}\left(\mathbf{f}_\mathbf{T}\right)}_{\text{convection}}}_{\text{Heat transfer}}=0 \tag{4.28}
$$

where H_m is the enthalpy of the whole medium and the heat transfer is composed of $\boldsymbol{\Gamma}$, the heat conduction, and $\mathbf{f_T}$, the convection. The mixture enthalpy can then be defined as the sum of the heat of each constituent with neglect to the contribution of CO_2 dissolved in water:

$$H = (1-n)\rho_s c_{p,s}(T-T_0) + nS_r\rho_w c_{p,w}(T-T_0) + n(1-S_r)\rho_c h_c \tag{4.29}$$

where $c_{p,\alpha}$ is the heat capacity of component α. The term h_c corresponds to the specific enthalpy of CO_2 which is temperature and pressure dependent. We determine the specific enthalpy through the fundamental thermodynamics relationship by integrating the Peng and Robinson EOS:

$$h_c = \frac{1}{M_C}\left(Z + \frac{T_c}{T}\phi^0\right) - \frac{\sqrt{2}a}{4bM_c}\left[1 + \frac{\kappa T}{\sqrt{\alpha T T_c}}\right]\ln\left(\frac{Z+(1+\sqrt{2})B}{Z+(1-\sqrt{2})B}\right) \tag{4.30}$$

where a, b, B, α and κ are the Peng and Robinson EOS parameters, which are pressure- and temperature-dependent, T_c is the critical temperature of CO_2 ($T_c = 304.25\,K$) and ϕ^0 is the Helmholtz energy for CO_2 at ideal gas conditions, given by Span and Wagner (1996). This formulation presents a pressure- and temperature-dependent specific enthalpy of CO_2. The advantage of such development is that the Joule-Thomson effect is included in the framework, i.e., depending on the initial state, the temperature of CO_2 will increase or decrease upon adiabatic expansion (Bacci et al., 2011; Böttcher et al., 2012a).

The heat transfer is governed by the thermal conduction and convection:

$$\boldsymbol{\Gamma} + \mathbf{f}_T = -\left(nS_w\lambda_w + n(1-S_w)\lambda_c + (1-n)\lambda_s\right)\mathbf{grad}T + c_{p,w}(T-T_0)\rho_w\mathbf{q}_w + h_c\rho_c\mathbf{q}_c \tag{4.31}$$

The first term corresponds to the heat conduction, where the mixture conductivity λ is considered as a function of the volume ratio of the thermal conductivity of solid λ_s, liquid water λ_w and CO_2 phase λ_c. Combing Eqs.(4.15), (4.21) and (4.22), the hydromechanical effect is placed on the energy balance, as obtained from Eq. (4.32). Changes in the enthalpy of the medium are dependent not only on the temperature variation but also on volumetric deformation. The thermo-hydraulics and thermo-mechanical coupling are present through

the porosity and the saturation. If the pore volume decreases, quantity of fluids (CO_2 or water or both) that hold the heat will decrease.

$$
\begin{aligned}
\frac{\partial\left(nS_w\rho_w c_w\left(T-T_0\right)\right)}{\partial t} = \Bigg\{ & \left[-n\frac{\partial S_w}{\partial s}+nS_w\rho_w\kappa_T+\frac{b-n}{K_s}S_w\left(S_w+\frac{\partial S_w}{\partial s}s\right)\right]\rho_w c_w\left(T-T_0\right)\frac{\partial p_w}{\partial t} \\
& +\left[n\frac{\partial S_w}{\partial s}+\frac{b-n}{K_s}S_w\left(1-S_w-\frac{\partial S_w}{\partial s}s\right)\right]\rho_w c_w\left(T-T_0\right)\frac{\partial p_c}{\partial t} \\
& -\left\{\left[\left(\mathrm{b}-\mathrm{n}\right)S_w 3\alpha_s - nS_w\beta_w\right]\rho_w c_w\left(T-T_0\right)+nS_w\rho_w c_w\right\}\frac{\partial T}{\partial t} \\
& +bS_w\rho_w c_w\left(T-T_0\right)\mathbf{div}\left(\frac{\partial \mathbf{u}}{\partial t}\right) \\
\frac{\partial\left(n\left(1-S_w\right)\rho_c h_c\right)}{\partial t} = \Bigg\{ & \left[\begin{array}{l} -n\frac{\partial S_w}{\partial s}\rho_c h_c+n\left(1-S_w\right)\left(\frac{1}{p_c}-\frac{1}{Z}\frac{dZ}{dp_c}\right)\rho_c h_c \\ +\frac{\left(b-n\right)}{K_s}\left(1-S_w\right)\left(1-S_w-\frac{\partial S_w}{\partial s}s\right)\rho_c h_c \\ +n\left(1-S_w\right)\rho_c\mu_{JT}c_{p,c}\end{array}\right]\frac{\partial p_c}{\partial t} \\
& +\left[\frac{\left(b-n\right)}{K_s}\cdot\left(1-S_w\right)\left(S_w+s\cdot\frac{\partial S_w}{\partial s}\right)+n\frac{\partial S_w}{\partial s}\right]\rho_c h_c\frac{\partial p_w}{\partial t} \\
& -\left[\left(b-n\right)3\alpha_s h_c+nh_c\left(\frac{1}{T}+\frac{1}{Z}\frac{dZ}{dT}\right)+nc_{p,c}\right]\left(1-S_w\right)\rho_c\frac{\partial T}{\partial t} \\
& +b\left(1-S_w\right)\rho_c h_c\mathbf{div}\left(\frac{\partial \mathbf{u}}{\partial t}\right) \\
\frac{\partial\left(\left(1-n\right)\rho_s c_{p,s}\left(T-T_0\right)\right)}{\partial t} = \Bigg\{ & +\left[\left(1-n\right)\rho_s c_{p,s}\right]\frac{\partial T}{\partial t} \\
\mathbf{div}\left(\mathbf{\Gamma}\right) = \Bigg\{ & +\mathbf{div}\left(-\left(nS_w\lambda_w+n\left(1-S_w\right)\lambda_C+\left(1-n\right)\lambda_S\right)\mathbf{grad}T\right) \\
\mathbf{div}\left(\mathbf{f}_\mathbf{T}\right) = \Bigg\{ & +\mathbf{div}\left(c_{p,w}\left(T-T_0\right)\rho_w\mathbf{q}_w+h_c\rho_c\mathbf{q}_c\right)=0
\end{aligned}
\tag{4.32}
$$

4.3.3 Momentum balance

The balance of linear momentum is written as

$$\mathbf{div}\left(\boldsymbol{\sigma}\right)+\rho\mathbf{g}=0 \tag{4.33}$$

where $\boldsymbol{\sigma}$ is the total Cauchy stress tensor with the tensile stress taken as negative and ρ is the bulk density defined as:

$$\rho = (1-n)\rho_s + nS_w\rho_w + n(1-S_w)\rho_c \tag{4.34}$$

The behaviour of the solid matrix is assumed to be governed by the generalized effective stress tensor $\boldsymbol{\sigma}'$ through a combination of the total stress and fluid pressures:

$$\boldsymbol{\sigma}' = \boldsymbol{\sigma} - b\left(S_w p_w + (1-S_w)p_c\right)\mathbf{I} \tag{4.35}$$

where **I** is the identity matrix**.** An average fluid pressure is defined as follows and is weighted by the saturation of each phase:

$$p_f = S_w p_w + (1-S_w)p_c \tag{4.36}$$

The effective stress in Eq. (4.35) thus becomes

$$\boldsymbol{\sigma}' = \boldsymbol{\sigma} - b p_f \mathbf{I} \tag{4.37}$$

An essential ingredient that contributes to the thermo-mechanical coupling is accounted for by the definition of strain due to the phenomenon of thermal expansion. The following description of thermoelastic strains is used:

$$d\boldsymbol{\varepsilon} = \mathbf{E}^{-1} d\boldsymbol{\sigma}' - \alpha_s \mathbf{I} dT \tag{4.38}$$

where $d\boldsymbol{\varepsilon}$ is the total strain tensor increment, **E** is the linear elastic tensor, and α_s is the thermal expansion coefficient. Young's modulus E and Poisson's ratio ν are used to characterize the elastic geomaterial.

4.4 Benchmark to the In Salah surface uplift problem

4.4.1 In Salah CO_2 storage project

In Salah is the biggest on shore CO_2 storage site, located at the Krechba gas field in Algeria as indicated in Figure 4.4b, showing the locations of the injection and production wells at Krechba field. This site produces natural gas, from which over one million tonne of CO_2 are produced every year as a bi-product. The geological storage of this CO_2 was explored as a mitigation option to reduce CO_2 emissions into the atmosphere. The geological formation conveniently acts as both the source and storage location, which means that transportation of the CO_2 is not required. The stratigraphic formation is shown in the Figure 4.4a, and is divided into six main layers (Ringrose et al., 2013): a 900 m thick layer of

sandstone and mudstone (Cretaceous Continental Intracalaire) representing the shallow aquifer, and a 750 m thick layer of mudstone (Visean Mudstone) representing the main caprock. The main CO_2 storage aquifer is an approximately 20 m thick C10.2 formation 1800 m below the surface. The C20 formation, a 130 m thick layer of silty shale representing the lower caprock, together with the 20 m layer of tight sandstone and siltstone C10.3 formation, form the sealing layer to prevent CO_2 from leaking at Krechba (Shi et al., 2012).

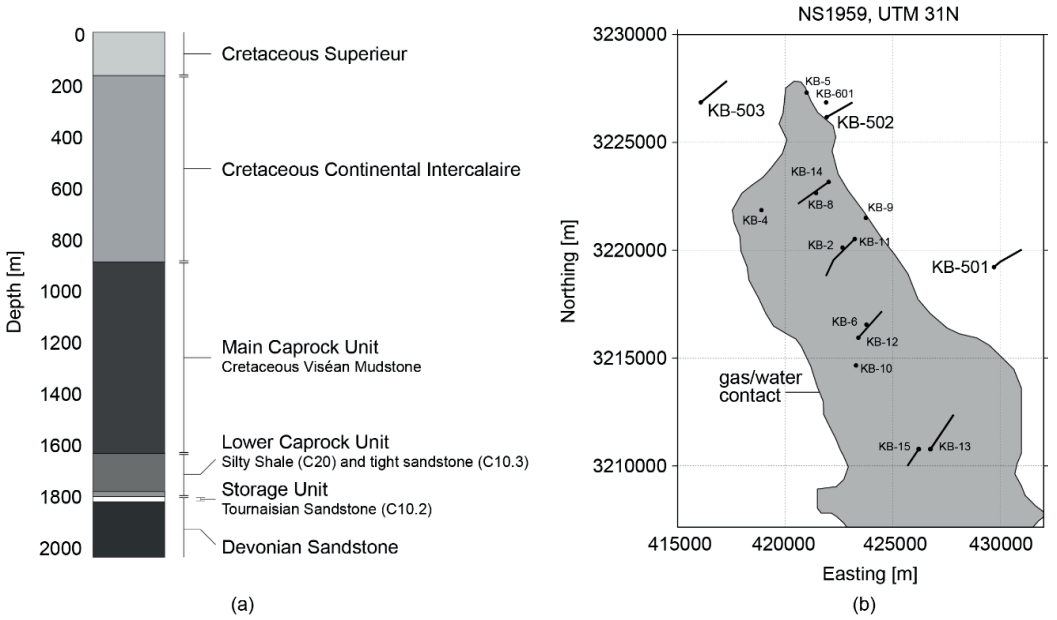

Figure 4.4 (a) Krechba geological stratigraphic summary; (b) Krechba field layout showing the locations of three injection wells KB501, KB502 and KB503 and injection wells figure; Both figures are adapted by the author from Ringrose et al. (2013), Mathieson et al. (2011) and White et al. (2015)

In 2004, the In Salah project began with three injection wells KB501, KB502 and KB503 located in the C10.2 carboniferous sandstone layer that is fully brine-saturated. This layer acts as the principle host formation for the storage of CO_2, and is also the layer from which natural gas is produced at other locations in the Krechba gas field. Shortly after the injection of CO_2 began, Interferometric Synthetic Aperture Radar (InSAR) satellite measurements detected surface uplift over the three injection well sites (Bohloli et al., 2013; Onuma and Ohkawa, 2009; Vasco et al., 2008). These surface uplifts are primarily due to the overpressure in the reservoir caused by the injection of CO_2. These measurements provide a viable benchmark that can be used in the computational analysis of the reservoir response to CO_2 injection and long-term storage. Regarding the current numerical investigation for

this problem at In Salah, Rutqvist et al. (2008) constrained a sequentially hydro-mechanical (HM) coupled model by matching the numerical prediction to the surface uplift that has been monitored at In Salah. A generally good trend is observed, but the difference between the field measurements and numerical predictions is not negligible. Following the same framework, Rinaldi et al. (2014) found a better agreement with the same uplift data through an inverse calculation that adjusts the temporal evolution of the material parameters to minimize the difference between the simulation results and field measurement. Nevertheless, the results of the THM fully coupled simulation that neglect the capillarity between CO_2 and water presented by Preisig and Prévost (2011), has an approximately two times higher estimation of the surface uplift evolution with the same parameters as Rutqvist et al. (2008).

4.4.2 Finite element model of In Salah around injection well KB501

Thermo-hydro-mechanically coupled simulations were run to analyse the reservoir response to high rate CO_2 injection, with the aim to gather information on the evolution of significant geomechanical variables such as surface deformation and stress variations. As shown in Figure 4.5, the THM coupled simulation is run for a two-dimensional section in the plane strain condition, representing the cross-section that is oriented perpendicular to the axis of the injection well and is located at the centre of the well. Two shallow layers are 900 m thick and 750 m thick. The top layer consists of soft cretaceous sandstones and mudstones. The lower layer corresponds to a relatively stiffer mudstone layer. The 20 m thick sandstone aquifer is constrained by a 150 m thick caprock layer of tight sandstone and an underburden layer of 180 m.

The reservoir model consists of 9683 bilinear quadrilateral elements. The elements are refined to 0.2 m in width around the injection well that measures 0.5 m in radius. The model is extended to 4 km to limit the boundary effects that could arise due to the constant pressure condition imposed on this boundary. Displacements are blocked in the perpendicular direction on the right-hand side and bottom of the model. A vertical temperature gradient of 33 °C/km is applied with an initial surface temperature of 30 °C. Therefore, at the depth of the injection well we have a temperature of approximately 90 °C. The temperature on the external boundary is fixed. The maximum horizontal stress is reported larger than the vertical stress, whereas the minimum horizontal stress is found parallel to the injection well (Iding and Ringrose, 2010). The stress magnitudes were estimated later by Morris et al.

(2011), which we use to assume the initial effective stress coefficient K_0 in this study as $\sigma'_H = 1.25\sigma'_v$ and $\sigma'_h = 0.41\sigma'_v$. The initial hydrostatic fluid conditions are applied with the model being fully saturated with brine. The brine density and viscosity in this study are approximated according to Batzle and Wang (1992), and the formulas take the salinity into account. We also account for in the calculation a salinity of 170 g per litre, which has been reported recently for In Salah by Trémosa et al. (2014). To give an idea the density of the brine is approximately 1100 kg/m3 and the viscosity is 5.2×10^{-5} Pa.s for a temperature of 90 °C and a pressure of 19 MPa at the initial state in the aquifer. The water and CO_2 pressures are fixed on the far side of the model. After applying gravity and hydrostatic pressure, the stress initialisation phase is established and the initial vertical effective stress σ'_v at the middle aquifer is 27.8 MPa. The thermo-hydro-mechanical simulation is run over a period of four and a half years. The injection rate is assumed to be 10 mmscfd (million standard cubic feet per day) for the 1.5 km injection well, representing a total amount of 14 bscf (billion standard cubic feet) or approximately 0.8 million tonnes of CO_2 over the whole injection duration, as measured in situ (Bohloli et al., 2013). Therefore, an amount of 0.02 1kg/s/m mass influx is prescribed on the well nodes.

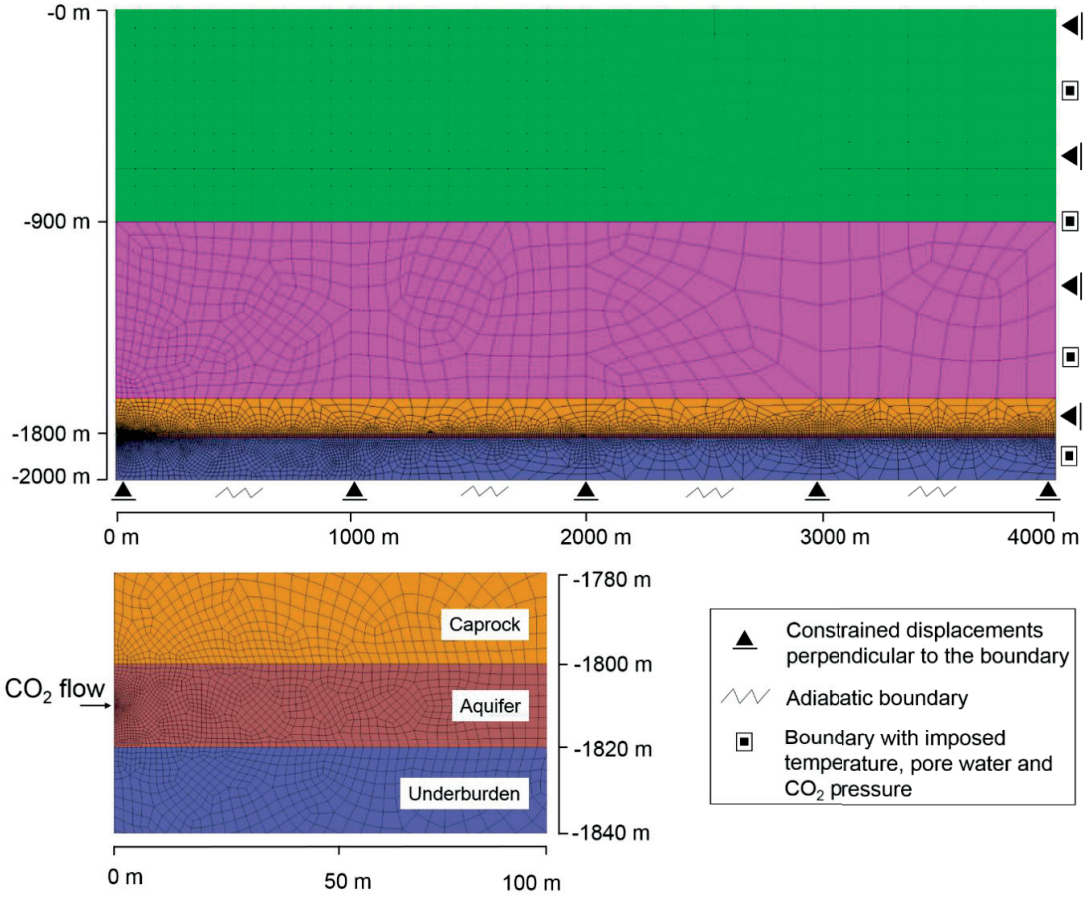

Figure 4.5 Two-dimensional finite element model of the section at In Salah CO_2 storage project, Krechba, Algeria

Parameters were adopted from the studies of Fang et al. (2013) and Shi et al. (2013), along with the hydraulic properties that are considered isotropic. Note that due to lack of better data, the thermo-hydraulic properties for the top three layers are based upon experimental studies on similar formations (Gilliam and Morgan, 1987; Jobmann and Polster, 2007; Robertson and Peck, 1974). Alhough there is some degree of uncertainty in the selected values, this may not have a significant impact on the results because both overpressure and cooling predominantly affect the lower part of the lower caprock as observed from the simulation results. The mechanical parameters for the lower caprock, aquifer and underburden layers are estimated from good quality core logs (Shi et al. 2013) and experimental works (Armitage et al., 2011); therefore, the confidence in their values is high. The retention and relative permeability (for CO2/brine) experimental data for the aquifer have been reported by Shi et al. (2012), and are taken into account in this study. We use the van Genuchten (van Genuchten, 1980) model to describe the retention behaviour of

rocks (Eq.(4.39)), whereas the functions from Corey (1954) are selected for the brine and CO2 relative permeability curves (Eq.(4.40)):

$$S_w = S_{res} + \left(1 - S_{res}\right)\left(1 + \left(s / P_r\right)^m\right)^{1/m-1} \tag{4.39}$$

$$\begin{aligned} k_{rc} &= \left(1 - S_e\right)^{CKA1}\left(1 - S_e^{CKA2}\right), S_e = \frac{S_w - S_{res}}{1 - S_{res}} \\ k_{rw} &= \sqrt{S_w}\left[1 - \left(1 - S_w^{1/CKW1}\right)^{CKW1}\right]^2 \end{aligned} \tag{4.40}$$

where m, P_r, $CKA1$, $CKA2$ and $CKW1$ are the material parameters that are obtained by matching the retention and relative permeability models to the experimental data as shown in Figure 4.6 and Figure 4.7 respectively. The retention curve for the lower caprock and underburden layers have been assumed with an air entry pressure value of approximately 1 MPa. The parameters for the simulation are summarized in Table 4.1.

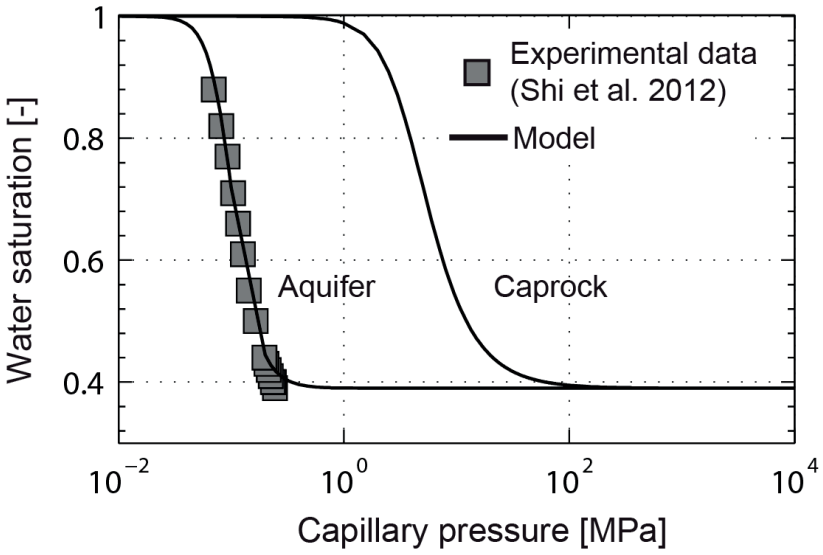

Figure 4.6 Water retention curve of the aquifer and the caprock; the water retention curve of the aquifer is calibrated with the experimental data

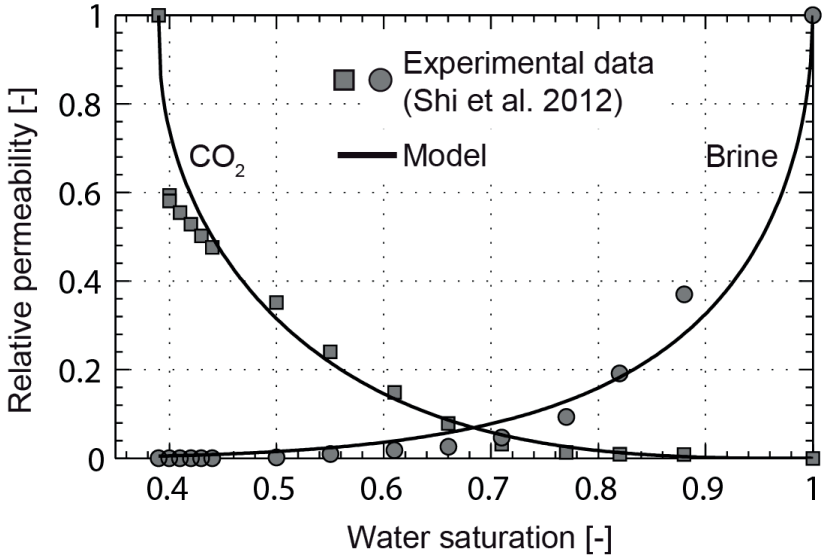

Figure 4.7 CO_2-brine relative permeability curves of the aquifer; the curves are calibrated with the experimental data

Table 4.1 Material parameters for the simulation of the In Salah site, the top layer and lower layer's material properties are taken from the In Salah JIP 2009 reference model proposed by Statoil (Morris et al., 2011).

Mechanical properties	Top layer	Lower layer	Caprock	Aquifer	Underburden
Young modulus E [GPa]	3.0	5.0	18	6.0	20
Poisson ratio ν [-]	0.2	0.3	0.15	0.20	0.30
Solid specific mass ρ_s [kg/m^3]	2600	2700	2400	2200	2800
Intrinsic permeability k_{int} [m^2]	1×10^{-18}	1×10^{-21}	1×10^{-21}	2×10^{-14}	1×10^{-19}
Initial porosity n_0 [-]	0.1	0.01	0.01	0.10	0.01
Tortuosity τ [-]	0.50	0.50	0.50	0.50	0.50
Biot coefficient b [-]	1.0	1.0	1.0	1.0	1.0
Flow parameters					
CO_2 relative permeability parameter *CKA1*	1.8	1.8	1.8	1.8	1.8
CO_2 relative permeability parameter *CKA2*	0.35	0.35	0.35	0.35	0.35
Water relative permeability parameter *CKW1*	0.52	0.52	0.52	0.52	0.52
Van Genuchten parameter m [-]	2.5	2.5	2.5	4.2	2.5
Van Genuchten parameter P_r [Pa]	4×10^6	4×10^6	4×10^6	9.5×10^4	4×10^6
Residual saturation [-]	0.39	0.39	0.39	0.39	0.39
Thermal parameters					
Saturated thermal conductivity λ_s [W/(m.K)]	1.5	1.5	1.50	2.50	1.50
Water thermal conductivity λ_w [W/(m.K)]	0.67	0.67	0.67	0.67	0.67
CO_2 thermal conductivity λ_a [W/(m.K)]	0.08	0.08	0.08	0.08	0.08
Solid specific heat capacity $c_{p,s}$ [J/(kg.K)]	950	950	950	850	950
Water specific heat capacity $c_{p,w}$ [J/(kg.K)]	4183	4183	4183	4183	4183
Solid thermal expansion coefficient α_s [K^{-1}]	1×10^{-5}	1×10^{-5}	1×10^{-5}	1×10^{-5}	1×10^{-5}
Water thermal expansion coefficient β_w [K^{-1}]	4.5×10^{-5}	4.5×10^{-5}	4.5×10^{-5}	4.5×10^{-5}	4.5×10^{-5}

4.5 Analysis of the reservoir response to CO_2 injection

4.5.1 Surface uplift

In Figure 4.8, the evolution of the surface uplift directly over the centre of the injection well is presented for the simulation and the InSAR field measurements. There is a good agreement between computed the results and the field measurement, for both the magnitude of uplift values and the temporal distribution. At the end of injection, an uplift of approximately 16 mm can be seen in both the InSAR data (presented in (Bohloli et al., 2013)) and the simulated results. During the period between 600 days and 1200 days, the simulated results are slightly higher than the InSAR data, but still well within an acceptable tolerance. Both the observed uplift and the calculated displacement tend to converge afterwards.

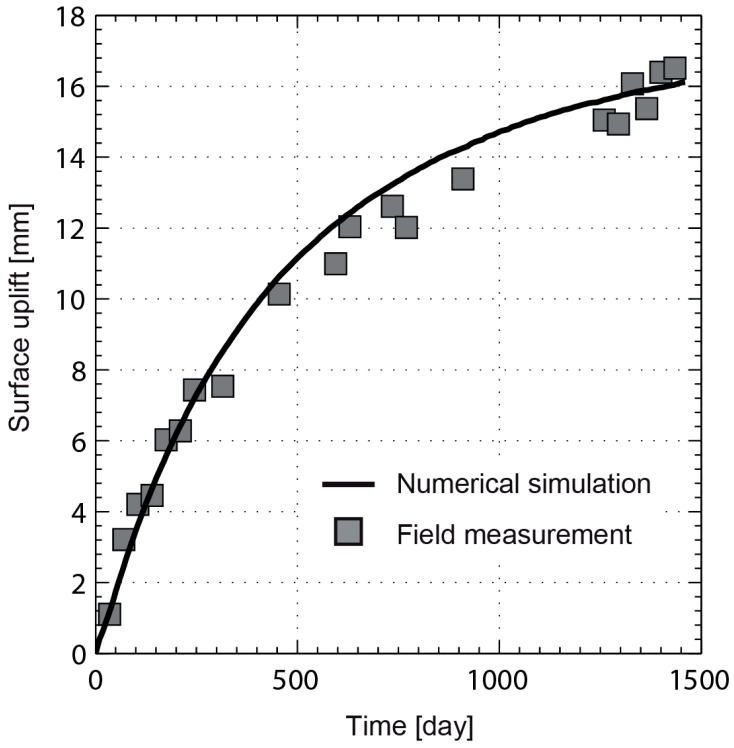

Figure 4.8 Comparison between the surface uplift and in-situ measurement over the injection well KB501, starting date from 26.06.2004. Measurement data are taken from Bohloli et al. (2013)

4.5.2 Thermo-hydro-mechanical responses

The results presented in Figure 4.9 correspond to the pressure, temperature and displacement profiles at a section 5 meters from the injection well. As shown in Figure

4.9a, the fluid pressure is increased 7 MPa within the aquifer and does not have a noticeable change in the caprock after 4.5 years of injection. The presence of the low permeable caprock acts as a barrier for overpressure to generate in the overlaid caprock. The cooling affects the near-well zone for the first year, the temperature drops about 10 °C within the caprock after the injection stops as shown in Figure 4.9b. Because there is no fluid pressure increase in the caprock, one can also conclude that the thermal flow in the caprock is only driven by the heat conduction because of the lack of fluid flow, whereas the thermal flow in the aquifer is driven by not only heat conduction but also convection. Therefore, the cooling-affected zone is smaller in the caprock than in the aquifer where the cooling is accelerated by the high convective flow, as shown in Figure 4.10. The cooling induces contraction of the aquifer, which is illustrated by the change in horizontal displacement both in the caprock and in the aquifer. Figure 4.9c shows that the near-well part contracts in the horizontal direction when it is subjected to cooling, further than the first 50 meters of the caprock at the end of injection. Due to the fluid pressure increase and associated stress changes, vertical expansion occurs in the aquifer, as illustrated in Figure 4.9d. The pressure increase within the aquifer results in a vertical displacement of approximately 2 cm at the top of the aquifer. The surface uplift is attenuated to 1.6 cm mainly due to the restriction by the bending of overlaid rocks. It should also be noted that the magnitude of the horizontal displacement is very small compared to the vertical component. Cooling contraction competes with pressurised expansion.

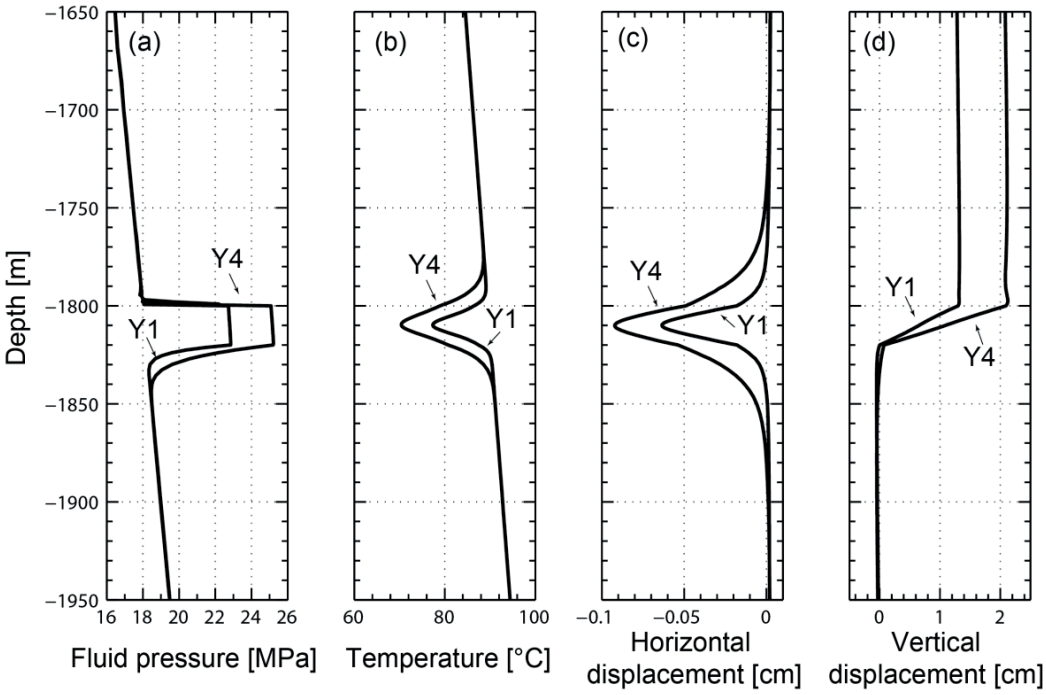

Figure 4.9 Results of the thermo-hydro-mechanical simulation at year 1 (Y1) and year 4 (Y4) for (a) fluid pressure; (b) temperature; (c) horizontal displacement and (d) vertical displacement, at a section 5 meters from the injection well

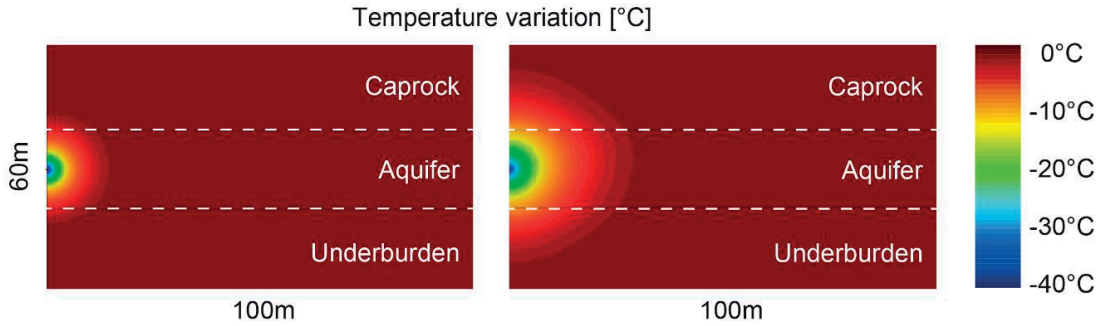

Figure 4.10 Spatial distribution of the temperature variation at year 1(left) and year 4 (right)

4.5.3 Reservoir stability

The stress paths of 5 points, which are arranged horizontally along the middle of the aquifer, are plotted in the *p'-q* plane in Figure 4.11 and are distributed according to their distance to the injection well. The initial stress is anisotropic, leading to a high initial deviatoric stress state. Because the fluid pressure is constantly increasing, the stress paths show a decrease in mean effective stress at all locations. The deviatoric stress also decreases on the locations far from the well. Close to the injection well, the temperature drop reduces the

effective stress mainly in the horizontal direction because of a displacement-fixed boundary at the left-hand side. Consequently, the deviatoric stress increases on the points at 5 meters and 10 meters. This thermal stress is attenuated with the distance to the injection well because the cooling range is limited. The thermal influence in this particular case is relatively small compared to the effect of the fluid pressure increase.

The reservoir stability is illustrated by means of a Mohr circle in Figure 4.12. Due to the initial anisotropic stress state, both the caprock and aquifer show a large Mohr circle at the initial conditions, which is prone to shearing failure. As explained above, the mean effective stress decrease leads to a shift of the Mohr circles towards the failure line, and the increase in size confirms the observation that the deviatoric stress is increased. Figure 4.12 shows that the caprock is potentially unstable after 4.5 years of injection while the aquifer is subjected to shear failure. In addition, this assumption does not take into account the heterogeneity of the caprock, drilling-induced damaged zone, or presence of pre-existing fractures. When considering these possibilities, shear failure is likely to occur near the well if the shear resistance of the caprock is low. Unfortunately, no experimental data are available for further investigation. It can be also noticed that the minimum principle stress σ_3' is reduced to approximately 7 MPa in compression by the end of the injection, showing that tensile failure is not likely to occur in the aquifer or in the caprock.

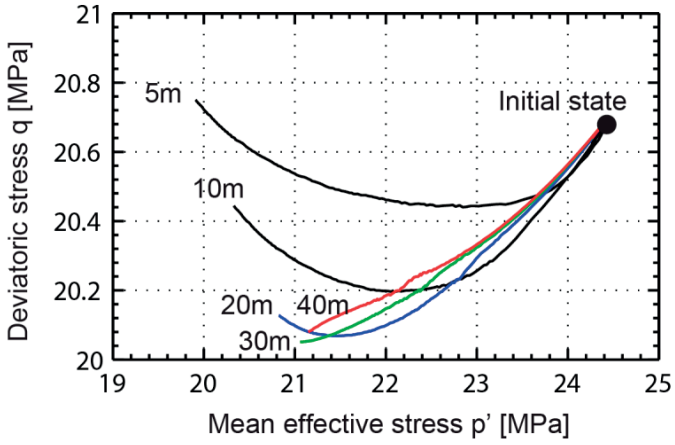

Figure 4.11 Stress paths in the p'-q planes at various distances from the injection well at the section in the middle of the aquifer

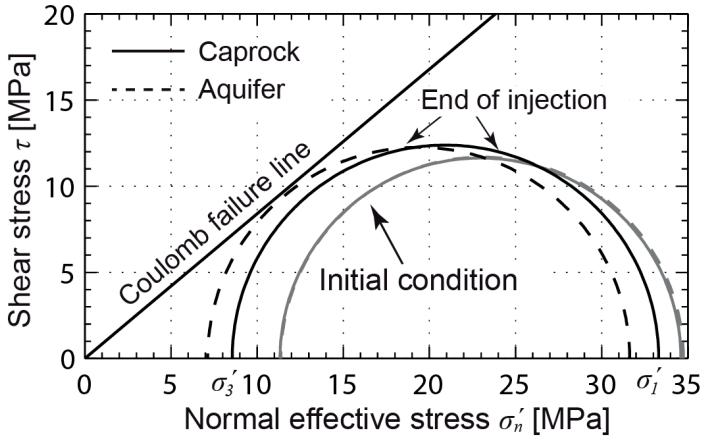

Figure 4.12 Mohr circles of the location at the middle of the aquifer 1 meter from the injection well and one meter above the aquifer-caprock interface over the injection well. Both are shown at the initial state and at the end of injection.

4.6 Conclusion

In this study, a coupled modelling framework was presented for the analysis of reservoir instability processes subjected to CO_2 injection. The thermal-hydro-mechanically coupled formulation integrates the real CO_2 state properties, including CO_2 dissolution and the Joule-Thomson effect, and is suitable for representing multiphase thermal and fluid flow processes and their influence on reservoir performance.

On the basis of the proposed modelling framework, a 2D finite element model was built based on the In Salah CO_2 project to simulate the thermo-hydro-mechanical model response to CO_2 injection over four and a half years of injection with a real injection rate. Instead of solving the fluid and thermal flow and injection-induced geomechanical problem in a sequential manner, the pore water pressure, CO_2 pressure, temperature and reservoir deformation were calculated simultaneously to assess the injection pressure- and temperature-induced geomechanical instabilities.

In contrast with former interpretations of the In Salah measurement data, we attempt to perform blind prediction in the vicinity of the injection well KB501 based on the best available thermo/hydro/mechanical, rather than invert of a specific model to best fit to the observed surface uplift. The comparison of the numerical results with the satellite-based surface uplift measurement demonstrated that the proposed model can reproduce the

surface uplift detected by the satellite at the In Salah CO_2 storage site. The result has an excellent agreement with the measurement. The analysis of the results from the 2D reservoir simulation revealed complex coupled mechanisms especially in the vicinity of the injection well. The fluid pressures are governed by the high injection rate input, increasing nearly 8 MPa, which is mainly responsible for the mean effective stress reduction. The pressure increase affects nearly the entire aquifer whereas the temperature drops in the vicinity of the injection well. The temperature decrease leads not only to a volume contraction but also to a decrease in the effective horizontal stress, which causes the additive generation of deviatoric stress. The results revealed that the stress paths close to the injection well could be assimilated to constantly decreasing mean effective stress with increasing fluid pressures. In addition, deviatoric stress increases due to cooling were observed as the cooling front propagates. The initial anisotropic stress state leads to a high shear failure potential after the cold CO_2 injection. The cooling effect leads to a further decrease in the minimum effective stress in addition to the stress reduction due to the pressure increase.

5 Impact of coupled properties on caprock stability

5.1 Introduction

The storage of CO_2 in geologic reservoirs, particularly in deep aquifers, has become a mitigation method used to reduce the impact of CO_2 and the greenhouse effect (Bachu, 2000; Bryant, 1997). There are currently several ongoing large-scale projects for CO_2 storage in deep aquifers, such as the In Salah CO_2 storage site in Algeria (Metz et al., 2005). The aquifer is usually overlain with a nearly impermeable caprock that primarily serves to prevent CO_2 from leaking (Shukla et al., 2010). Therefore, caprock stability is the main concern, which is also the objective of the current investigation.

The hydromechanical (HM) coupled problems involved in the CO_2 injection problems have received particular attention, as reviewed by Rutqvist (2012). A large volume of injected CO_2 can transform a water reservoir into a CO_2 reservoir and result in the accumulation of overpressure. This overpressure rapidly perturbs the stress field upon injection within the aquifer and extends to the caprock, as results of the main HM coupled processes. In addition, the injection temperature is usually lower than that of the aquifer (Bissell et al., 2011), which adds a thermal factor to HM coupling. The cooling will contract rocks and reduces stresses if constrained, whereas the overpressure will result in an expansion along with a stress reduction. Both effects may be counterbalanced or superposed depending on the specific configuration of the problem, which requires a fully coupled thermal-hydro-mechanical (THM) investigation and motivated numerous computational studies as well as this study, with two main objectives. The first objective is to assess whether the failure potential is attained when the caprock is subjected to a lower temperature; and secondly, to highlight the importance of key factors that are involved in the THM processes. Regarding the former, the low-temperature injection may cause a reduction of compressive stress or even induce tensile stress in the caprock (Gor et al., 2013; Preisig and Prévost, 2011) whereas Vilarrasa et al. (2014, 2013) concluded that there was an improvement in the caprock stability. Vilarrasa et al. (2014) state that these studies are contradictory, although they are complementary, as demonstrated in this study. In view of these studies, despite a similar theoretical formulation, the problem formulations are different from one study to another, and factors such as material properties are different as well, which have a significant influence on the results. This confusion leads to the second objective, which is the effect of material properties on the caprock stability. Current analyses of material sensitivity mainly solely focus on the effect of an intrinsic property of rocks, e.g., overpressure increase is influenced by an aquifer's permeability, and no significant

influence is observed in caprock stability when varying the Young's modulus of the aquifer, as concluded by Bao et al. (2013). However, two key coupled properties of rocks are missing in these studies: an HM coupled property: the Biot coefficient; and a thermal-mechanical property: thermal expansion coefficient. In addition, with regards to the special boundary configuration of CO_2 injection problems (caprock overlying an aquifer), the combination of material properties of the caprock and aquifer are believed to affect the response regimes and may also provide an explanation for the aforementioned contradictory conclusions. Furthermore, the thermal diffusion properties are also crucial for cooling inside the caprock, whose effect on the caprock stability is not known yet.

The main goal of this study is to fill these gaps such that a more rigorous conclusion can be achieved when assessing caprock stability under low-temperature CO_2 injection. We first introduce a CO_2 injection problem in a normal faulting system where the essential physical processes are described. The THM fully coupled theoretical formulation is then presented in detail with the incorporation of the nonlinearity of the CO_2 state properties, especially with an emphasis on the coupled phenomena and thermodynamics, as well as the necessary constitutive equations to describe them. Next, results are presented with a reference model with particular reference to the THM response within the caprock. The coupled effect of the caprock thermal properties, the Biot coefficients of both the caprock and aquifer, and the caprock thermal expansion coefficient are investigated, which to our knowledge has not yet been addressed. These properties are not studied solely from the geomechanical and geometrical perspectives. The geomechanical perspectives is to couple the investigation with other parameters such as Young's modulus to achieve more systematic insights. On the other hand, the objective from a geometrical perspective is to present the results on caprock stability under the influence of the aquifer's behaviour. Although numerical efforts place a burden on the feasibility of the material properties' sensitivity computations, the study cases were carefully chosen to be realistic and to allow us to extract novel quantitative information on the effect of the coupled properties on caprock stability.

5.2 Coupled processes in CGS

Figure 5.1 presents the geometry of the model under investigation. The model consists of three essential geological strata involved in the CO_2 storage problem, sealing caprock, storage aquifer and underburden rock, which are porous media. Two-phase fluid flow

processes in such porous media can be described in the context of the theory of mixtures (Bowen, 1982). This theory postulates the mass balance for each phase and each species, providing an explicit mass quantity during the phase change that cancels out in the balance equations of the species with the compositional approach (Collin, 2003; Panday and Corapcioglu, 1989).

To understand the coupling of the overpressure, temperature effect and thermal diffusion to the deformable porous media mechanics, it is necessary to define the appropriate conditions that are encountered in a CO_2 storage project. The injection of CO_2 is modelled as a prescribed CO_2 mass flow at one million tonne per year through a vertical well along the thickness of an aquifer in a normal faulting system. The initial temperature of the reservoir is set as 330K. The injection temperature is set to 300K, which is within the range of such applications (Song and Zhang, 2013). The aquifer is considered to be water saturated prior to the injection and acted as a host medium for CO_2. The caprock is nearly impermeable to prevent the leakage of CO_2. A constantly distributed stress of 13.5MPa is applied along the top of the caprock, which is equivalent to the overburden's dead load. The displacement on the right-hand side and bottom of the model was constrained in the perpendicular direction.

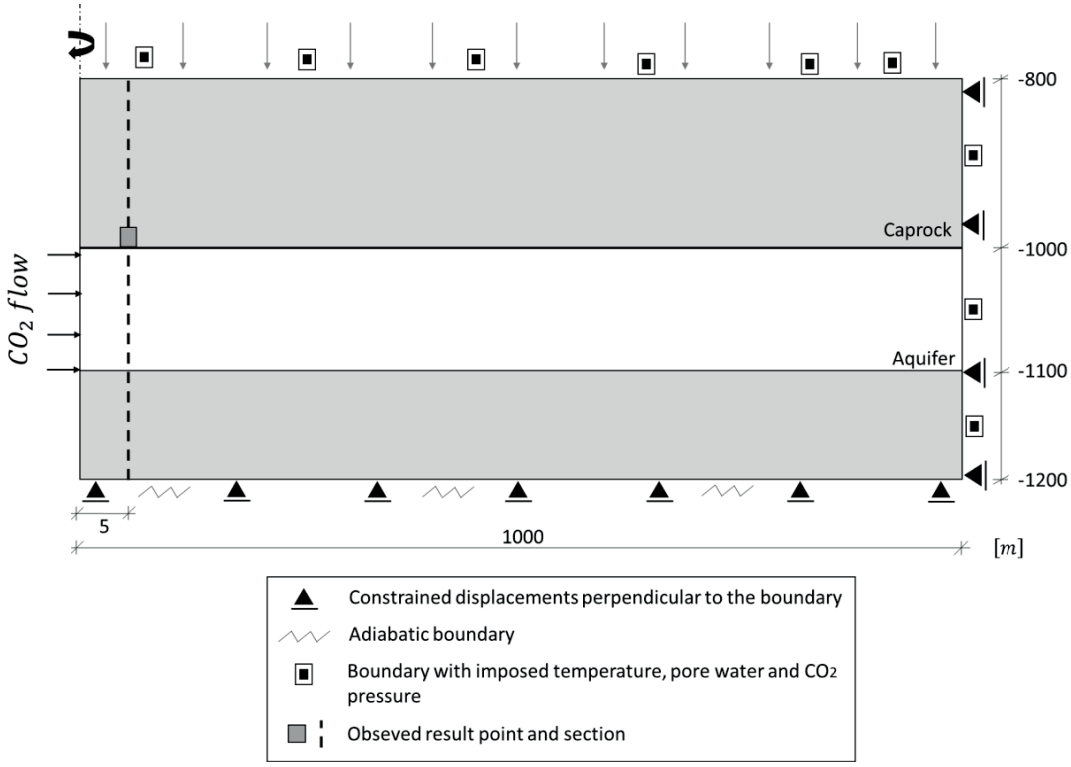

Figure 5.1 Geometry of the storage system under consideration and, the locations of the points where results were determined

The two main coupled processes are thus the CO_2 inflow into the storage aquifer from the injection well and the rapid generation of pressurization, which induced stress variations as the primary HM coupling. Meanwhile, the cooling simultaneously occurs adjacent to the injection well to cope with pressurization-induced expansion and provokes shrinkage in the surrounding materials. The thermal convective flow, which is driven by the CO_2 injected flow, dominates the heat transfer in the aquifer. On the other side, the cooling mainly occurs by heat conduction within the caprock because almost no flow takes place for its very low permeability. An upward movement of the cold flow occurs from the bottom of the caprock, which leads to the THM coupling process that is presented in the following section.

5.3 Thermal-hydro-mechanical formulation

5.3.1 Mass balance

As stated previously, a compositional approach is employed for this study, as implemented for water and perfect gas in the finite element code *Lagamine* (Charlier et al., 2011; Collin,

2003). This approach brings the advantage of writing the mass balance equation for two-phase fluids in a straightforward manner. Based on this, we improve the current code with supercritical fluid properties, including terms for the storage of both CO_2 and water in liquid and gaseous forms, the advective flow of both fluids, and the non-advective flow of dissolved CO_2 in the water. The water phase pressure p_w, CO_2 phase pressure p_c, temperature T and solid displacement field $\boldsymbol{u}$ are chosen as the material's primary state variables. The mass balance equations and fluid flows are expressed in the moving current configuration using a Lagrangian updated formulation (Charlier et al., 2011), through which the solid mass is automatically conserved for a reference elementary volume V:

$$\frac{d\left(\left(1-n\right)\rho_s\right)}{dt}=0 \tag{5.1}$$

where t is time, and n is the porosity, ρ_s is the solid density, for which the equation of state from Lewis and Schrefler (1998) is adapted:

$$\frac{1}{\rho_s}\frac{d\rho_s}{dt}=\frac{1}{1-n}\left[\frac{\left(b-n\right)}{K_s}\frac{d}{dt}\left(S_w p_w+\left(1-S_w\right)p_c\right)-3\left(b-n\right)\alpha_s\frac{dT}{dt}-\left(1-b\right)\mathbf{div}\left(\frac{\partial\mathbf{u}}{\partial t}\right)\right] \tag{5.2}$$

where b is the Biot coefficient, K_s is the bulk modulus of the solid matrix and α_s is the linear thermal expansion coefficient for the solid. The water phase saturation S_w is a function of the capillary pressure (suction) s which is defined as the difference between the CO_2 phase and the water phase pressures $s = P_c - P_w$. The relationship between the saturation and suction will be given later. Introducing Eq. (5.2) into Eq. (5.1), the solid mass balance equation is then expressed in terms of variation of the porosity by the primary state variables:

$$\frac{dn}{dt}=\left(b-n\right)\left[\frac{1}{K_s}\frac{d}{dt}\left(S_w p_w+\left(1-S_w\right)p_c\right)-3\alpha_s\frac{dT}{dt}+\mathbf{div}\left(\frac{\partial\mathbf{u}}{\partial t}\right)\right] \tag{5.3}$$

This defines the coupling between the geomechanics and thermo-hydraulics. The change in porosity is explicitly shown to be proportional to three terms, (a) a volumetrically weighted fluid pressure $P_f = S_w P_w + (1 - S_w)P_w$, (b) temperature and (c) matrix volumetric deformation. Note that the Biot coefficient plays a dominant role in terms of the porosity variation.

The mass balance equation for the *water specie* and *CO_2 specie* are written, respectively as:

$$\underbrace{\frac{\partial\left(nS_w\rho_w\right)}{\partial t}+\mathbf{div}\left(\rho_w\mathbf{q}_w\right)}_{\text{liquid water}}=0 \tag{5.4}$$

$$\underbrace{\frac{\partial\left(n\left(1-S_w\right)\rho_c\right)}{\partial t}+\mathbf{div}\left(\rho_c\mathbf{q}_c\right)}_{\text{superitical/liquid CO}_2}+\underbrace{\frac{\partial\left(nS_w\rho_{dc}\right)}{\partial t}+\mathbf{div}\left(\rho_{dc}\mathbf{q}_w\right)+\mathbf{div}\left(\mathbf{i}_{dc}\right)}_{\text{dissolved CO}_2\text{ in the water}}=0 \tag{5.5}$$

We account for the dissolution of CO_2 in the water, but no water dissolution in the CO_2 is involved, and there is one more component in the mass balance of the *CO_2 specie,* i.e., Eq. (5.5), than in that of the water, i.e., Eq. (5.4). Note also that the mass exchange associated with the dissolution is not visible in Eq. (5.5), which is a consequence of the employment of the compositional approach.

Among these terms, the liquid water and supercritical/liquid CO_2 flow $\mathbf{q}_w$ and $\mathbf{q}_c$ are governed by the generalized Darcy's law for porous media to determine the advective flow:

$$\mathbf{q}_{w,c}=-\frac{\mathbf{k}k_{rw,rc}}{\mu_{w,c}}\left[\mathbf{grad}\left(p_{w,c}\right)+\rho_{w,c}\mathbf{g}\right] \tag{5.6}$$

where $\mathbf{k}$ is the intrinsic permeability and k_{rw}, k_{rc} are the water and CO_2 relative permeabilities, respectively, which are geomaterial dependent parameters. μ_w is the dynamic viscosity of water, which is calculated according to Thomas and King (1994) and μ_w is the dynamic viscosity of CO_2, which follows the relationship of Fenghour et al. (1998) and is valid for the ranges of temperatures and pressures considered here.

The liquid water is considered to be a compressible and dilatant fluid, for which the density ρ_w is:

$$\begin{aligned}&\rho_w=\rho_{w0}\exp\left[\kappa_T\left(p_w-p_{wr}\right)-\beta_w\left(T-T_r\right)\right]\\&\frac{1}{\rho_w}\frac{\partial\rho_w}{\partial p_w}=\kappa_T\quad;\quad-\frac{1}{\rho_w}\frac{\partial\rho_w}{\partial T}=\beta_w\end{aligned} \tag{5.7}$$

where ρ_{w0} is the reference density for a given salinity at reference pressure p_{wr} and reference temperature T_r. κ_T is the isothermal water compressibility, and β_w is the volumetric thermal expansion coefficient of water.

The CO_2 involved in CO_2 storage cannot be considered to be a perfect gas because of its high-pressure high-temperature condition. A compressibility factor Z is used to describe the deviation from a perfect gas density to a real gas as:

$$\rho_c = \frac{1}{Z}\frac{M}{R}\frac{p_c}{T} \quad ; \quad \frac{1}{\rho_c}\frac{\partial \rho_c}{\partial p_c} = \left(\frac{1}{p_c} - \frac{1}{Z}\frac{dZ}{dp_c}\right) \quad ; \quad \frac{1}{\rho_c}\frac{\partial \rho_c}{\partial T} = -\left(\frac{1}{T} + \frac{1}{Z}\frac{dZ}{dT}\right) \tag{5.8}$$

The factor Z is a pressure- and temperature-dependent parameter. The advantage of expressing the change in density as a function of Z is that one can express the compressible behaviour of gaseous, liquid and supercritical CO_2 with appropriate equations of state (EOSs). In this study, the factor Z is calculated using the Peng and Robinson EOS (Peng and Robinson, 1976) because of its accuracy and computational efficiency (Lin, 2008).

The Henry law, which describes the amount of a given perfect gas that dissolves in a volume of water, is extended for a real gas with the gas fugacity (Pruess and García, 2002) which is determined using the Peng and Robinson EOS as well:

$$\Phi p_c = K_{eq,g-l}^{co_2} X_{dc} \tag{5.9}$$

where $K_{eq,g-l}^{co_2}$ is the temperature-dependent Henry's constant determined according to Crovetto (1991), and X_{dc} is the mole fraction of dissolved CO_2 in water. Inserting the relationship of Eq. (5.8), the dissolution amount can be represented by the dissolved mass in a unit volume of water as:

$$\rho_{dc} = \frac{\Phi Z \rho_w RT}{K_{eq,g-l}^{co_2} M_w}\rho_c \tag{5.10}$$

This relationship is used in the CO_2 diffusion law that is based on Fick's law in a tortuous medium:

$$\mathbf{i}_{dc} = -nS_w \tau D_c \rho_w \mathbf{grad}\left(\frac{\rho_{dc}}{\rho_w}\right) \tag{5.11}$$

where D_c is the diffusion coefficient of the dissolved CO_2 in the water phase and τ is the tortuosity of the porous media.

Accounting for the variation of porosity (Eq. (5.3)) and the compressible properties of water (Eq. (5.7)) leads to a coupled mass balance for solid and liquid water (Eq. (5.4)) as:

$$\frac{\partial\left(nS_w\rho_w\right)}{\partial t}=\begin{cases}\left[-n\dfrac{\partial S_w}{\partial s}+nS_w\kappa_T+\dfrac{b-n}{K_s}S_w\left(S_w+\dfrac{\partial S_w}{\partial s}s\right)\right]\dfrac{\partial p_w}{\partial t}\\ \quad+\left[n\dfrac{\partial S_w}{\partial s}+\dfrac{b-n}{K_s}S_w\left(1-S_w-\dfrac{\partial S_w}{\partial s}s\right)\right]\dfrac{\partial p_c}{\partial t}\\ \quad-\left[\left(\mathrm{b}-\mathrm{n}\right)S_w 3\alpha_s-nS_w\beta_w\right]\dfrac{\partial T}{\partial t}\\ \quad+bS_w\mathbf{div}\left(\dfrac{\partial\mathbf{u}}{\partial t}\right)\end{cases} \tag{5.12}$$

$$\mathbf{div}\left(\rho_w\mathbf{q}_w\right)=\begin{cases}\quad+\mathbf{div}\left(-\dfrac{\mathbf{k}k_{rw}}{\mu_w}\left[\mathbf{grad}\left(p_w\right)+\rho_w\mathbf{g}\right]\right)=0\end{cases}$$

The mass conservation of *CO_2 specie* (Eq. (5.5)) in a deformable medium is obtained by integrating Eq. (5.8) and Eq. (5.6) as:

$$
\begin{aligned}
\frac{\partial\left(n\left(1-S_w\right)\rho_c\right)}{\partial t} + \frac{\partial\left(nS_w\rho_{dc}\right)}{\partial t} = & \left\{ \begin{array}{l} n\left(\rho_{dc}-\rho_c\right)\dfrac{\partial S_w}{\partial s} + nS_w\dfrac{\partial \rho_{dc}}{\partial p_c} + n\left(1-S_w\right)\rho_c\left(\dfrac{1}{p_c}-\dfrac{1}{Z}\dfrac{\partial Z}{\partial p_c}\right) \\ +\dfrac{\left(b-n\right)}{K_s}\left[S_w\rho_{dc}+\left(1-S_w\right)\rho_c\right]\left(1-S_w-s\dfrac{\partial S_w}{\partial s}\right) \end{array} \right\}\frac{\partial p_c}{\partial t} \\
& + \left\{ \begin{array}{l} \dfrac{\left(b-n\right)}{K_s}\cdot\left[S_w\rho_{dc}+\left(1-S_w\right)\rho_c\right]\left(S_w+s\cdot\dfrac{\partial S_w}{\partial s}\right) \\ -n\left(\rho_{dc}-\rho_c\right)\dfrac{\partial S_w}{\partial s} \end{array} \right\}\frac{\partial p_w}{\partial t} \\
& - \left\{ \begin{array}{l} \left(b-n\right)3\alpha_s\left[\left(1-S_w\right)\rho_c+S_w\rho_{dc}\right]+nS_w\dfrac{\partial \rho_{dc}}{\partial T} \\ +\left(1-S_w\right)n\rho_c\left(\dfrac{1}{T}+\dfrac{1}{Z}\dfrac{\partial Z}{\partial T}\right) \end{array} \right\}\frac{\partial T}{\partial t} \\
& + \left[S_w\rho_{dc}+\left(1-S_w\right)\rho_c\right]\cdot b\cdot\mathbf{div}\left(\frac{\partial \mathbf{u}}{\partial t}\right)
\end{aligned}
$$

$$
\begin{aligned}
\mathbf{div}\left(\rho_{dc}\mathbf{q}_w\right) + \mathbf{div}\left(\mathbf{i}_{dc}\right) = & + \mathbf{div}\left(-\rho_{dc}\frac{\mathbf{k}k_{rw}}{\mu_w}\left[\mathbf{grad}\left(p_w\right)+\rho_w\mathbf{g}\right]\right) \\
& - \mathbf{div}\left(nS_w\tau D_c\rho_w\mathbf{grad}\left(\frac{\rho_{dc}}{\rho_w}\right)\right)
\end{aligned}
$$

$$
\mathbf{div}\left(\rho_c\mathbf{q}_c\right) = + \mathbf{div}\left(-\rho_c\frac{\mathbf{k}k_{rc}}{\mu_c}\left[\mathbf{grad}\left(p_c\right)+\rho_c\mathbf{g}\right]\right) = 0 \tag{5.13}
$$

The mass balance equations Eq. (5.12) and Eq. (5.13) govern the coupled diffusion behaviour, in which the quantities $\boldsymbol{k}$, k_{rc}, k_{rw} and, S_w are dependent on the geomaterial of a specific site and will be detailed in the section related to the model setup.

5.3.2 Energy balance

Assuming thermal equilibrium, a unique temperature is defined for the mixture. The energy balance equation of the mixture has the following form:

$$
\underbrace{\frac{\partial H}{\partial t}}_{\text{Heat storage}} + \underbrace{\underbrace{\mathbf{div}\left(\mathbf{\Gamma}\right)}_{\text{conduction}} + \underbrace{\mathbf{div}\left(\mathbf{f_T}\right)}_{\text{convection}}}_{\text{Heat transfer}} = 0 \tag{5.14}
$$

where H is the enthalpy of the whole medium and the heat transfer is composed of $\mathbf{\Gamma}$, the heat conduction, and $\mathbf{f_T}$, the convection. The mixture enthalpy can then be defined as the

sum of the heat of each constituent neglecting the contribution of the dissolved CO_2 in the water:

$$H = (1-n)\rho_s c_{p,s}(T-T_0) + nS_r\rho_w c_{p,w}(T-T_0) + n(1-S_r)\rho_c h_c \tag{5.15}$$

where $c_{p,\alpha}$ is the heat capacity of the component α. The term h_c corresponds to the specific enthalpy of CO_2 which is temperature and pressure dependent. It can be determined through the fundamental thermodynamics relationship by employing the Peng and Robinson EOS:

$$h_c = \frac{1}{M_C}\left(Z + \frac{T_c}{T}\phi^0\right) - \frac{\sqrt{2}a}{4bM_c}\left[1 + \frac{\kappa T}{\sqrt{\alpha T T_c}}\right]\ln\left(\frac{Z+(1+\sqrt{2})B}{Z+(1-\sqrt{2})B}\right) \tag{5.16}$$

where a, b, B, α and κ are the Peng and Robinson EOS parameters, T_c is the critical temperature of the CO_2 ($T_c = 304.25\ K$), and ϕ^0 is the Helmholtz energy for CO_2 under ideal gas condition, as given by Span and Wagner (1996).

The heat transfer is governed by the heat conduction and convection:

$$\mathbf{\Gamma} + \mathbf{f_T} = -\left(nS_w\lambda_w + n(1-S_w)\lambda_C + (1-n)\lambda_S\right)\mathbf{grad}T + c_{p,w}(T-T_0)\rho_w\mathbf{q}_w + h_c\rho_c\mathbf{q}_c \tag{5.17}$$

The first term corresponds to the heat conduction where the mixture conductivity is considered to be a function of the volume ratio of the solid, liquid water and CO_2 phases. It can be observed that thermo-hydraulics and thermo-mechanical coupling are present through the porosity and saturation.

As stated previously and presented later in this chapter, the most important thermal feature in the caprock is the heat conduction. If considering a particular configuration such that the vertical one-dimensional flux occurs from the bottom of the caprock, the energy balanced equation Eq. (5.14) can be simplified under a water-saturated condition as:

$$\frac{\partial T}{\partial t} = D\frac{\partial^2 T}{\partial z^2} \quad \text{and} \quad D = \frac{\lambda_m}{(\rho c_p)_m} = \frac{n\lambda_w + (1-n)\lambda_S}{(1-n)\rho_s c_{p,s} + n\rho_w c_{p,w}} \tag{5.18}$$

$D\ [m^2/s]$ is the thermal diffusivity which is a measure of the thermal inertia and the controlling parameter for the heat conduction process, as defined as the ratio between the

saturated conductivity λ_m and the volumetric heat capacity $(\rho c_p)_m$. The cooling proceeds more quickly if the material has a higher thermal diffusivity, and the mechanical stability will therefore be altered more quickly.

5.3.3 Momentum balance

The balance of linear momentum is written as

$$\mathbf{div}(\boldsymbol{\sigma}) + \rho \mathbf{g} = 0 \tag{5.19}$$

where $\boldsymbol{\sigma}$ is the total Cauchy stress tensor with the tensile stress taken as negative and ρ is the bulk density, which is defined as:

$$\rho = (1-n)\rho_s + nS_w\rho_w + n(1-S_w)\rho_c \tag{5.20}$$

The behaviour of the solid matrix is assumed to be governed by the generalized effective stress tensor $\boldsymbol{\sigma}'$ through a combination of total stress and fluid pressures:

$$\boldsymbol{\sigma}' = \boldsymbol{\sigma} - b\left(S_w p_w + (1-S_w)\, p_c\right)\mathbf{I} \tag{5.21}$$

where **I** is the identity matrix**.** An average fluid pressure weighted by the saturation of each phase is defined as:

$$p_f = S_w p_w + (1-S_w)\, p_c \tag{5.22}$$

The effective stress in Eq. (5.21) thus becomes

$$\boldsymbol{\sigma}' = \boldsymbol{\sigma} - b\, p_f \mathbf{I} \tag{5.23}$$

An important ingredient that contributes to the thermo-mechanical coupling is accounted for by the definition of the strain, due to thermal expansion. The following description includes the thermoelastic strains:

$$d\boldsymbol{\varepsilon} = \mathbf{E}^{-1} d\boldsymbol{\sigma}' - \alpha_s \mathbf{I} dT \tag{5.24}$$

where $d\boldsymbol{\varepsilon}$ is the total strain tensor increment, **E** the linear elastic tensor, and α_s is the thermal expansion coefficient. Using Young's modulus E and Poisson's ratio ν to characterize the elastic geomaterial, we can write this expression in a more explicit form with indexed notation:

$$d\varepsilon_{ij} = \frac{1+\nu}{E} d\sigma_{ij} - \frac{\nu}{E} d\sigma'_{kk}\delta_{ij} - \alpha_s dT\delta_{ij}$$

or (5.25)

$$d\sigma'_{ij} = \frac{E}{1+\nu}\left\{ d\varepsilon_{ij} + \frac{\nu}{1-2\nu} d\varepsilon_{kk}\delta_{ij} \right\} + \frac{E\alpha_s dT}{1-2\nu}\delta_{ij}$$

From equations (5.23), (5.24) and (5.25), we find that as the temperature decreases at constant volume, the relationship can be described as:

$$d\boldsymbol{\sigma}' = d\boldsymbol{\sigma} - bdp_f \mathbf{I} \quad \text{and} \quad d\boldsymbol{\sigma}' = \mathbf{E}\alpha_s dT \quad \text{or} \quad d\sigma'_{ij} = \frac{E\alpha_s dT}{1-2\nu}\delta_{ij} \tag{5.26}$$

When evolving under only a decrease of temperature and in the absence of fluid pressure variation, the stress will be reduced as the product of the elastic properties, temperature variation and thermal expansion coefficient is incremented. The thermal expansion coefficient thereby has an important impact on the mechanical behaviour. A large temperature increment and high magnitude of the elastic modulus will certainly lead to more stress reduction, as illustrated by Preisig and Prévost (2011). However, when a constraint on the temperature is imposed, as in the case of isothermal injection or in an area where temperature front has not yet reached, the effect of Biot coefficient on the stress reduction is evident for a given fluid pressure increment.

5.4 Model Characteristics

It is necessary to describe the materials involved in this study. A sealing caprock usually involves very low permeability and porosity but an aquifer is much more porous, whereupon we consider clayey shale as the caprock, and sandstone as the storage rock, which is the case in most on-going CO_2 storage projects (Busch et al., 2008; Metz et al., 2005). The fluid thermodynamic properties are taken from Jamieson et al. (1969) and Wilson (1973), and the geomaterial parameters are taken as the averaged values from Rutqvist (2002) and Tsang Vilarrasa (2013). The rocks are initially saturated and later come into contact with the invading CO_2, and the water and CO_2 pressure are generated along with the development of suction. Therefore, the aquifer is subjected to desaturation through changes in the relative permeability, which influences the pressure generation. A

van Genuchten function is used to describe the retention behaviour of the rocks, and a power law for the relative permeability is used:

$$S_w = \left(1+\left(s/P_r\right)^{1/(1-m)}\right)^{-m} \tag{5.27}$$

$$k_{rw} = S_w^{CKW} \qquad k_{rc} = \left(1-S_w\right)^{CKC} \tag{5.28}$$

where m and P_r are a material parameter and a reference pressure, CKW and CKC are material parameters. The parameters for the reference simulation are summarized in Table 5.1. The variations in the coupled parameters and thermal properties are specified in the corresponding analysis.

Table 5.1 Material parameters for the reference model

Thermal parameters	Symbol	Unit	Seal	Aquifer	Underburden
Saturated thermal conductivity	λ_s	W/(m.K)	1.50	2.50	1.50
Water thermal conductivity	λ_w	W/(m.K)	0.67	0.67	0.67
CO_2 thermal conductivity	λ_a	W/(m.K)	0.08	0.08	0.08
Solid specific heat capacity	$c_{p,s}$	J/(kg.K)	950	850	950
Water specific heat capacity	$c_{p,w}$	J/(kg.K)	4183	4183	4183
Solid thermal expansion coefficient	α_s	K^{-1}	1×10^{-5}	1×10^{-5}	1.5×10^{-5}
Water thermal expansion coefficient	β_w	K^{-1}	4.5×10^{-5}	4.5×10^{-5}	4.5×10^{-5}
Flow parameters					
Intrinsic permeability	k_{int}	m^2	1×10^{-18}	1×10^{-13}	1×10^{-18}
CO_2 relative permeability	k_{rc}	-	S_c^6	S_c^3	S_c^6
Water relative permeability	k_{rw}	-	S_w^6	S_w^3	S_w^6
Van Genuchten parameter	m	-	0.80	0.50	0.80
Van Genuchten parameter	P_r	MPa	0.60	0.02	0.60
Initial porosity	n_0	-	0.01	0.10	0.01
Tortuosity	τ	-	0.50	0.50	0.50
Other parameters					
Solid specific mass	ρ_s	kg/m^3	2700	2400	2700
Water specific mass	ρ_w	kg/m^3	1000	1000	1000
Mechanical parameters					
Young modulus	E	GPa	5.0	2.5	5.0
Poisson ratio	ν	-	0.30	0.30	0.30
Initial stress factor	K_0	-	0.60	0.60	0.60

The model consists of 8723 quadrilateral elements and is run as an axisymmetric model. Despite the geometry of the problem, which was defined in the physical description section, the loading path of the simulation is required. The initial stress equilibrium is obtained by the application of the body force and the lithostatic stress along the top of the caprock. The horizontal stress is calculated with a lateral earth pressure ratio K_0 taken as 0.6 as for a normal stress faulting system.

5.5 Non-isothermal CO_2 injection

The two simulations described in Figure 5.2 correspond to the stress and displacement evolution of both isothermal injection and low-temperature injection. For isothermal injection (Figure 5.2a-d), injection induced overpressure is the only driving mechanism to reduce the caprock stability. The fluid pressure is raised rapidly at the very beginning of the injection, whereupon both horizontal and effective stresses drop quickly in the first dozens of days (Figure 5.2a and b). An expansion within the aquifer is observed and pushes the caprock upwards, and a slight compressional regime is thus triggered in the caprock because the vertical displacement is restricted due to the bending moment (Li et al., 2015; Selvadurai, 2008), which is observed as a transfer delay of displacement as shown between $-950m$ to $-1000m$ in Figure 5.2d. The occurrence of this compression contributed a small add of stress, which unfortunately remains at a level that was too small to improve the caprock stability. This also indicates that the stress state within the caprock depends on the expansion level of the aquifer.

The results of the low-temperature injection are shown in Figure 5.2e-h to illustrate the thermal contribution to the reservoir performance. It can be noted that the cooling has a major influence on the horizontal components of the stress and displacement (Figure 5.2e and g), and a moderate influence on the vertical one (Figure 5.2f and h). The cooling significantly reduces the vertical displacement at 300 days (Figure 5.2d and Figure 5.2h), and alters the horizontal displacement regime from expansion to contraction (Figure 5.2c and Figure 5.2g). However, free contraction upon cooling is not fully allowed due to the boundary condition on the left-hand side, whereupon such a deformation constraint causes a significant horizontal stress reduction upon cooling (Recall Eq. 25). There is nearly a factor of two stress reduction within the aquifer upon cooling compared to that without

cooling in the horizontal direction. More stress reduction are observed upon cooling at the interface aquifer-caprock for both short and long durations, when comparing Figure 5.2a and Figure 5.2e. On the other hand, the vertical displacement is less constrained, although the level of stress reduction is as significant as the horizontal reduction in the aquifer at ten days, as illustrated by the results in Figure 5.2b and Figure 5.2f. This can be explained because the expansion is sustained by the overpressure that is being generated inside the aquifer over the short term; the deformation upon cooling is thus mostly restricted by that expansion and converted to a stress reduction in return. Over the long term, part of effective stress reduction is recovered in the aquifer due to the overpressure drop. The overall decrease in the vertical effective stress is thereby reduced in the aquifer. In the lower portion of the caprock, the vertical effective stress continues to decrease, which is a direct consequence of the cooling induced stress reduction for the constrained deformation condition. Figure 5.2a, b, e and f clearly show that the effect of cooling on the effective stress reduction is greater than that of overpressure, being a factor of two in the decrease in the effective stress within the aquifer and more than three times on the interface of the aquifer-caprock, especially in the horizontal direction.

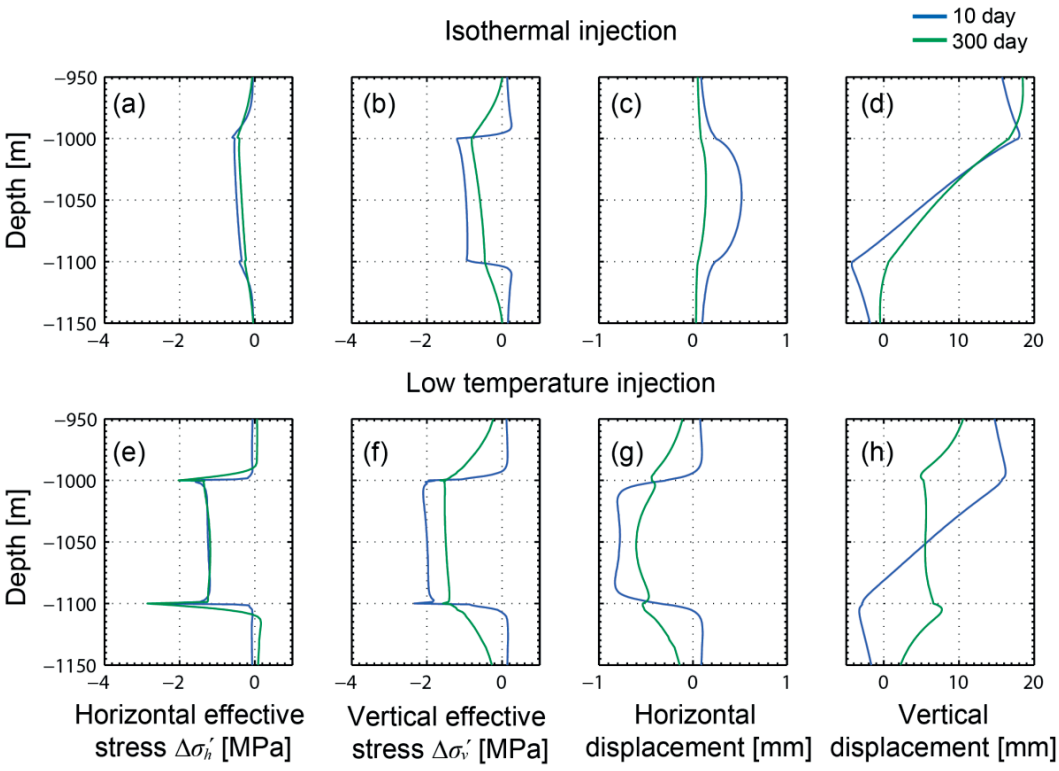

Figure 5.2 Results of the hydromechanical and thermo-hydro-mechanical simulations for (a), (e) Horizontal effective stress variation; (b), (f) vertical effective stress variation; (c),

(g) horizontal displacement and (d), (h) vertical displacement, at a section 5 meters from the injection well

Figure 5.3 more precisely shows the development of the effective horizontal stress of a section 5 meters from the well, with a zoom in the stress and temperature distributions in the first 25 metres of the caprock. After ten days of low-temperature injection, the locations above the interface caprock-aquifer are subjected to a 23°C decrease in temperature. The effective horizontal stress decreases by approximately 2MPa at this interface, but it decreases 1.2MPa in the aquifer, in which the temperature decreases 30°C. This remarkably sharp reduction in stress in the caprock compared to that in the aquifer is found to depend on the ratio of the thermo-mechanical coupled terms $\frac{E\alpha}{1-2\upsilon}$ between the caprock and aquifer, which will be investigated later in the section *Influence of the thermal-mechanical coupling parameters.*

The upward propagating temperature decrease continues from the aquifer to the caprock, reducing the stress as shown in the zoom of Figure 5.3. After 100 days the stress variation remains unchanged at the interface where the temperature has dropped to the injection temperature. As shown in the zoom of Figure 5.3, the caprock experiences a reduction in stress as the temperature decrease spreads upward and tends toward a steady state. The stress reduction exhibits a negligible delay with respect to the cooling front, and both have a nearly identical trend. This corresponds to the proportionality between the two terms $d\sigma'$ and dT as indicated in the Eq. (24), which reveals that the injection induced pressurization has been accommodated by the cooling effect in the caprock and that, the thermal contraction has a major influence on the stress reduction there.

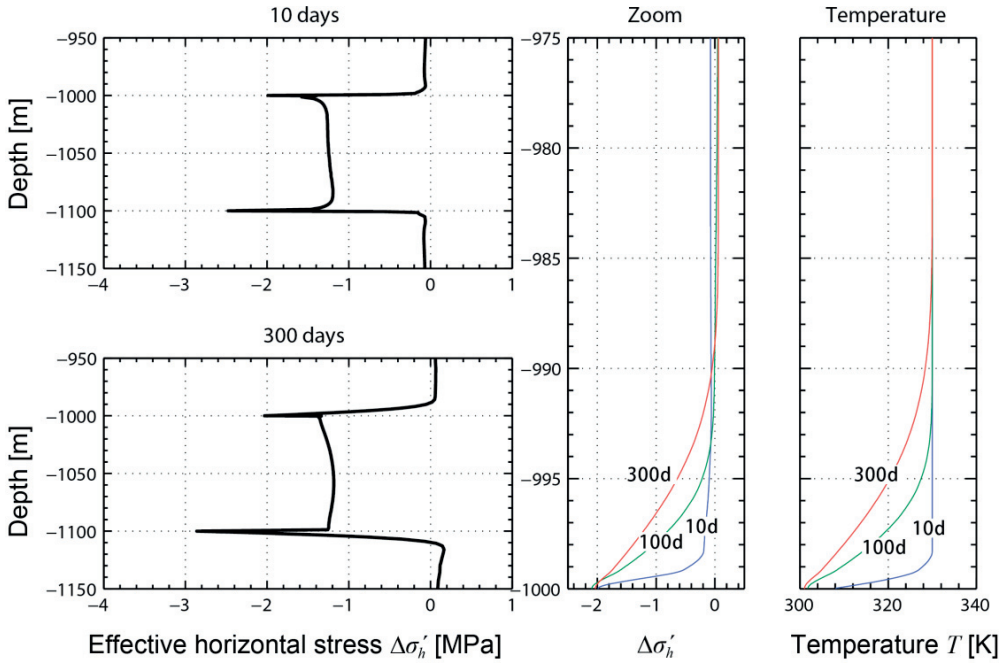

Figure 5.3 Horizontal effective stress variations at a section 5 meters from the injection well with a zoom of the stress variation and temperature in the first 25 meters in the caprock

5.6 Influence of the thermal transport properties

The thermal conduction is dominant in the caprock as observed in the simulation. It is therefore necessary to investigate the role of the thermal diffusivity in controlling the heat transfer process. Experimental studies on the thermal conductivity of shales have shown that the conductivity varies from *0.7* to *2.1 w/(m.K)* (Blackwell and Steele, 1989; Eppelbaum et al., 2014), the saturated specific capacity is in the range of *850-1100 J/(kg.K)* (Eppelbaum et al., 2014; Pasquale et al., 2011; Robertson, 1988; Waples and Waples, 2004) and the measured density range from *2400* to *2700 kg/m*^{3} as shown in (Shalabi et al., 2007). The diffusivity is the ratio between the thermal conductivity and the production of the density and specific heat capacity as shown in Eq. (5.18). We suggest three thermal diffusivities for the caprock *D=3.35E-7* ($\lambda = 0.95, c_p = 1050, \rho = 2700$), *5.85E-7*($\lambda = 1.5, c_p = 950, \rho = 2700$), and *1.03E-6 m*^{2}*/s* ($\lambda = 2.1, c_p = 850, \rho = 2400$). Note that the highest diffusivity is calculated from the maximum combination of the experiment data, although a lower density is chosen, which changes the initial stress state of the caprock.

The three simulations of the Figure 5.4 correspond to a higher thermal expansion coefficient of the caprock α_c =*2.0E-5* to better illustrate the effect. As shown in the temperature profile of Figure 5.4d, the cooling front moves upwards faster with a higher thermal diffusivity. Correspondingly, in the presence of a restricted deformation, the horizontal effective stress is reduced according to the distribution of the temperature decrease. For the simulation with the highest value of thermal diffusivity, *D=1.03E-6*, the cooling has an impact on the first $15m$ of the caprock for a period of 300 days, which is twice that for *D=3.35E-7*. The acceleration in the stress reduction upon cooling can be clearly observed with the increase in diffusivity in Figure 5.4a-c, for which the rate is proportional to the value of the thermal diffusivity. Therefore, the prediction of thermal transfer can be helpful to foresee the cooling breakthrough of the caprock.

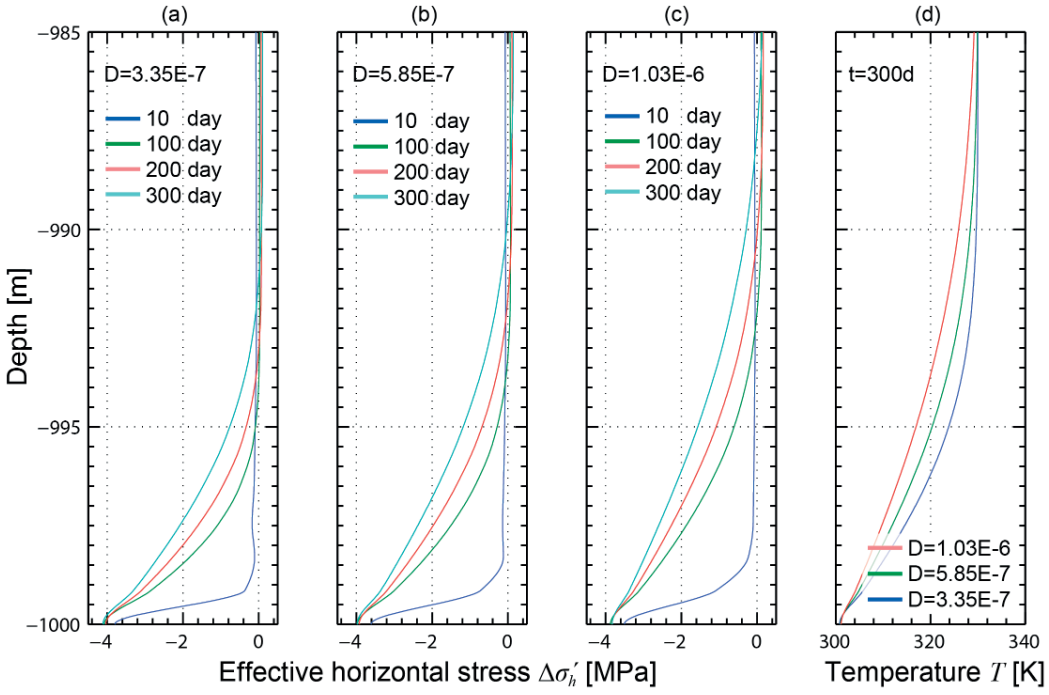

Figure 5.4 Effect of the thermal diffusivity on the horizontal effective stress variations and temperature profiles for three diffusivities at t=300 days.

The thermal conduction governs the heat transfer within the caprock. Based on this observation, we approximate the vertical movement of the cooling front in a section of the caprock by solving the simplified 1D heat transfer equation, as in Eq. (5.18). As seen in Figure 5.4, the reduction in the effective stress mostly follows the temperature distribution within the caprock. Therefore, temperature evolution can be used as an estimation tool to evaluate the times and distances that are affected by the cooling-induced reduction in stress.

If the interface aquifer-caprock is subjected to an injection temperature $T_{int} = 300K$ at an instant *t=0,* and the far side of the vertical section remains at the initial temperature of $T_0 = 330K$, the analytical solution Eq. (5.18) can be used to estimate the vertical temperature distribution, as given as follows:

$$T(z,t) = (T_{\text{int}} - T_0)\,\text{erfc}\left(\frac{z}{2\sqrt{Dt}}\right) + T_0 \tag{5.29}$$

The Complementary Error Function erfc can be solved using MATLAB built-in function. The results shown in Figure 5.5 correspond to the three simulations of Figure 5.4. The analytical calculation is in excellent agreement with the numerical simulation of the temperature evolution for simulation times of 100 days and 300 days. In addition, we calculated the temperature distribution for another four years of injection. It can be observed that the cooling transfer very rapidly at the beginning but also slows down very quickly later on, following the nature of erfc $\left(\frac{1}{2\sqrt{Dt}}\right)$. The cooling front holds in a vertical position in the caprock for a long time. The calculations also confirm the numerical observations of Vilarrasa et al. (2014) for a long term simulation. Note that this solution is useful for the zone close to the injection well where the temperature at of the caprock base quickly attains the injection temperature after the beginning of injection. In the far zone only a minor drop in temperature is found. And T_{int} refers to the temperature at the interface aquifer-caprock.

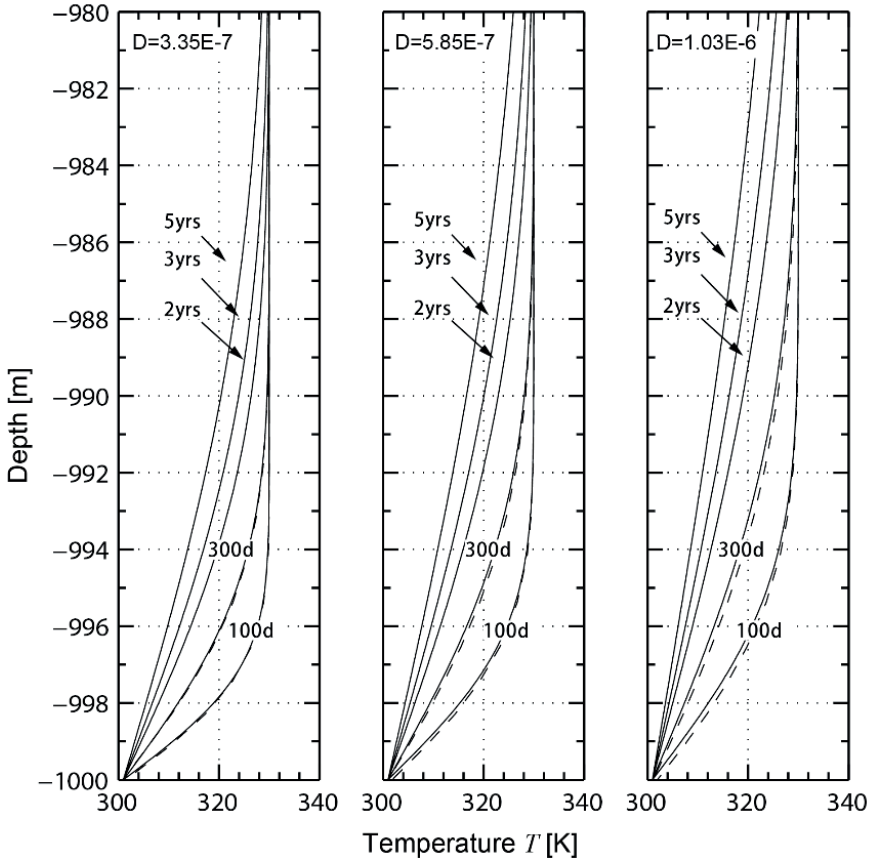

Figure 5.5 Analytical prediction (solid lines) of the temperature profiles with comparison to the numerical result (dotted lines) for t=100day and t=300day.

5.7 Influence of the thermomechanical coupled properties

The thermal expansion coefficient governs the shrinkage level of the rocks upon cooling, and for the few studies that have addressed this aspect for CO_2 problems, a value of unity is usually considered. Only Vilarrasa (2014) has suggested that the caprock stability is reduced in a normal faulting system in the absence of the thermal expansion coefficient, although neglecting the coefficient is certainly contrary to reality. Cooling induced stress reduction is sensitive to the thermal expansion coefficient as shown in Eq.(5.26). Experimental investigations have shown that the coefficient differs from unity and ranges from *1.0E-5 to 2.0E-5* (Gilliam and Morgan, 1987; Jobmann and Polster, 2007). The quantitative influence of the coefficient is sufficiently interesting to warrant investigation.

Figure 5.6 shows graphs of the horizontal stress reduction and displacement for three thermal expansion coefficients of the caprock $\alpha_c = \alpha_a$, $1.5\alpha_a$ and $2\alpha_a$ with α_a=*1.0E-5* in all three cases. For the sake of clarity, because its overall behaviour varies slightly in the later period of injection, as shown in Figure 5.2e, the horizontal stress variation is only shown at 100 days whereas the displacements are shown at 4 times during the first year. Figure 5.6d-f show that the horizontal displacement increases very slightly in the negative direction as the thermal expansion coefficient increases. The displacement is still very constrained as mentioned previously. Consequently, the increase in the thermal expansion coefficient can only trigger a severe reduction of stress under such a deformation-constrained condition. The magnitude of the effective stress reduction is proportional to the value of thermal expansion coefficient for a given stiffness of rock. Note that for the case where the thermal expansion coefficients of the caprock and aquifer are equal, $\alpha_c = \alpha_a$, the horizontal stress drops more in the caprock than in the aquifer because the caprock is twice as stiff as the aquifer. This observation is confirmed by Eq.(5.25), the cooling induced stress reduction is indeed controlled by the combination of three hydro-mechanical parameters as $\frac{E\alpha}{1-2\upsilon}$ for a same decrease in temperature. At the interface aquifer-caprock, the ratio $R = \frac{E_c\alpha_c}{1-2\upsilon_c} / \frac{E_a\alpha_a}{1-2\upsilon_a}$ can indicate the stress reduction difference between the point in the caprock and that in the aquifer, if both are subjected to the same temperature drop.

The caprock's stiffness is thus investigated to discriminate the effect of $\frac{E\alpha}{1-2\upsilon}$ of the caprock and aquifer. As shown in Figure 5.7, three stiffnesses of the caprock, $E_c = 1, 2 \text{ and } 5$ GPa are considered for a setup of a thermal expansion coefficient $\alpha_c = 1.5\ \alpha_a$, $E_a = 2.5GPa$ for the aquifer and $\upsilon = 0.3$ for both the caprock and aquifer. The results are shown for 100 days and 300 days after the beginning of injection, at which time the temperature at interface has already reached the injection temperature. In all three cases, the vertical effective stress experiences a similar reduction in magnitude, which is not significantly influenced by variations in Young's modulus, whereas the Young's modulus has a major impact on the horizontal effective stress reduction. For the lowest value of $E_c = 1GPa$, the ratio $R = \frac{E_c\alpha_c}{1-2\upsilon_c} / \frac{E_a\alpha_a}{1-2\upsilon_a}$ between the caprock and aquifer is small as $R = 0.6$. The decreased horizontal effective stress upon cooling is therefore lower in the caprock than that in the aquifer. The decrease in the vertical effective stress is higher than the horizontal one with this combination inside the caprock. In the case where the stiffness of the caprock

is equal to $E_c = 2GPa$, shown in Figure 5.7b, although smaller than that of the aquifer, $\frac{E\alpha}{1-2\upsilon}$ of the caprock becomes slightly higher due to the higher thermal expansion coefficient, leading to $R = 1.2$. The decrease in the horizontal effective stress is thereby lightly greater in the caprock than that in the aquifer, which is less than the effective stress reduction of the vertical one at the interface caprock-aquifer. As long as the ratio is as high as $R = 3$ as illustrated in Figure 5.7c, the horizontal stress has a major reduction and is higher than the decrease in the vertical effective stress, and a sharp difference in the stress reduction is observed.

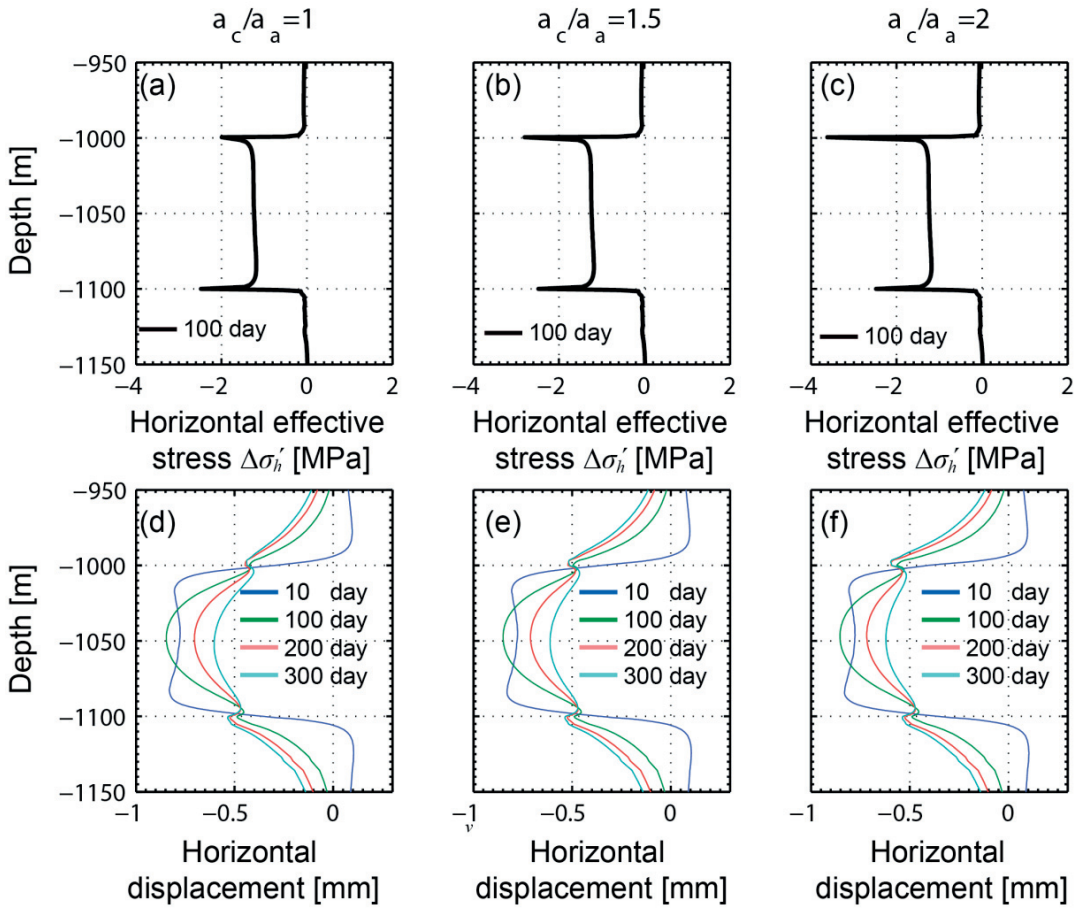

Figure 5.6 Effect of the thermal expansion coefficient of the caprock on the horizontal stress variations and the horizontal displacement at 5 meters away from the injection well.

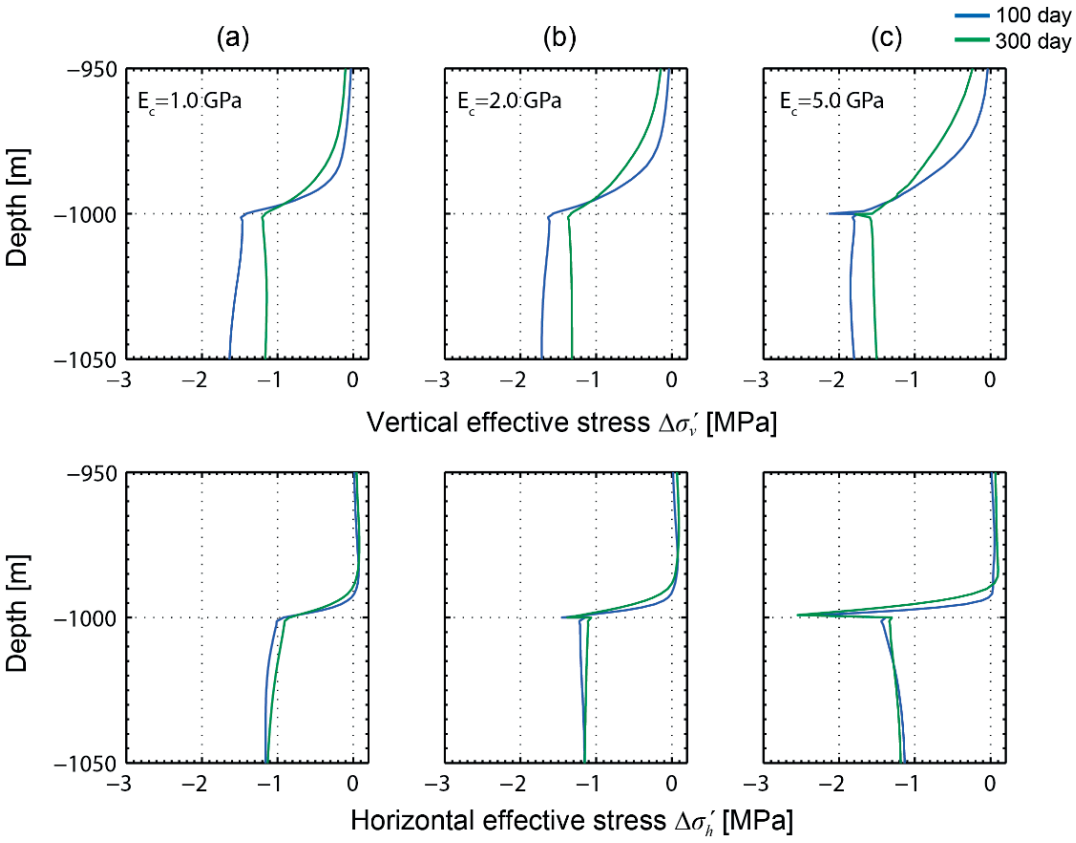

Figure 5.7 Effect of the caprock's Young's modulus on the vertical and horizontal effective stress variations 5 metres from the injection well.

5.8 Influence of the hydromechanical coupled property

The Biot coefficient b governs the percentage of stress reduction that is caused by the overpressure, which is defined as $= 1 - \frac{K_m}{K_s}$, where K_m is the bulk modulus of the porous matrix and K_s is the bulk modulus of the solid particles. For soft and unconsolidated rock, $b = 1$ and for a stiff rock, $0.5 < b < 1$. The Biot coefficient has been assumed to be 1 in current numerical studies (Orlic, 2009; Preisig and Prévost, 2011; Vilarrasa et al., 2010b), but the coefficient usually differs from 1 for sandstones from experimental studies (Bouteca et al., 2013; Nur and Byerlee, 1971; Siggins, 2003; Vidal-Gilbert et al., 2010). Note that a Biot coefficient of 0.5 can reduce the overpressure effect by half. A recent study has shown that a very low porous shale has a Biot coefficient close to 0.9 (personal communication by V. Favero EPFL, 2015).

Figure 5.8 illustrates the effect of the Biot coefficient on the vertical effective stress variation $\Delta\sigma_v'$ and the vertical displacement. Aquifers are usually represented as sandstone-like materials, for which the solid compressibility is comparable to the matrix compressibility, which leads to a lower value of the Biot coefficient. A comparison of the graphs in Figure 5.8a and Figure 5.8c reveals that the Biot coefficient of the aquifer has a moderate influence on the vertical displacement and a minor influence on the stress reduction. As recalled of Eq. (4.35), the effect of the overpressure on the effective stress – the hydromechanical coupling effect, is reduced for a lower values of the Biot coefficient, whereupon the aquifer undergoes a smaller order of magnitude expansion. The displacement is reduced by 30% at 10 days when the Biot coefficient of the aquifer changes from 1.0 to 0.6. Accordingly, the caprock experiences the same reduction because of the displacement continuity. Because the initial expansion driven by overpressure is reduced with the lower Biot coefficient, whereas the subsequent cooling continues to have a dominant impact on the deformation, a negative vertical displacement is eventually observed at 300 days. This suggests that the caprock may have induced the settlement in the long term cooling when the hydromechanical coupling term becomes weak. The results in Figure 5.8b-d demonstrate that the consideration of the caprock's Biot coefficient has a negligible effect on the caprock deformation. The level of displacement in the lower portion of the caprock is essentially controlled by the expansion of the aquifer, which implies that it is primarily influenced by the consideration of the Biot coefficient of the aquifer. The subsequent reduction in the vertical stress is solely affected by cooling not by hydromechanical coupling.

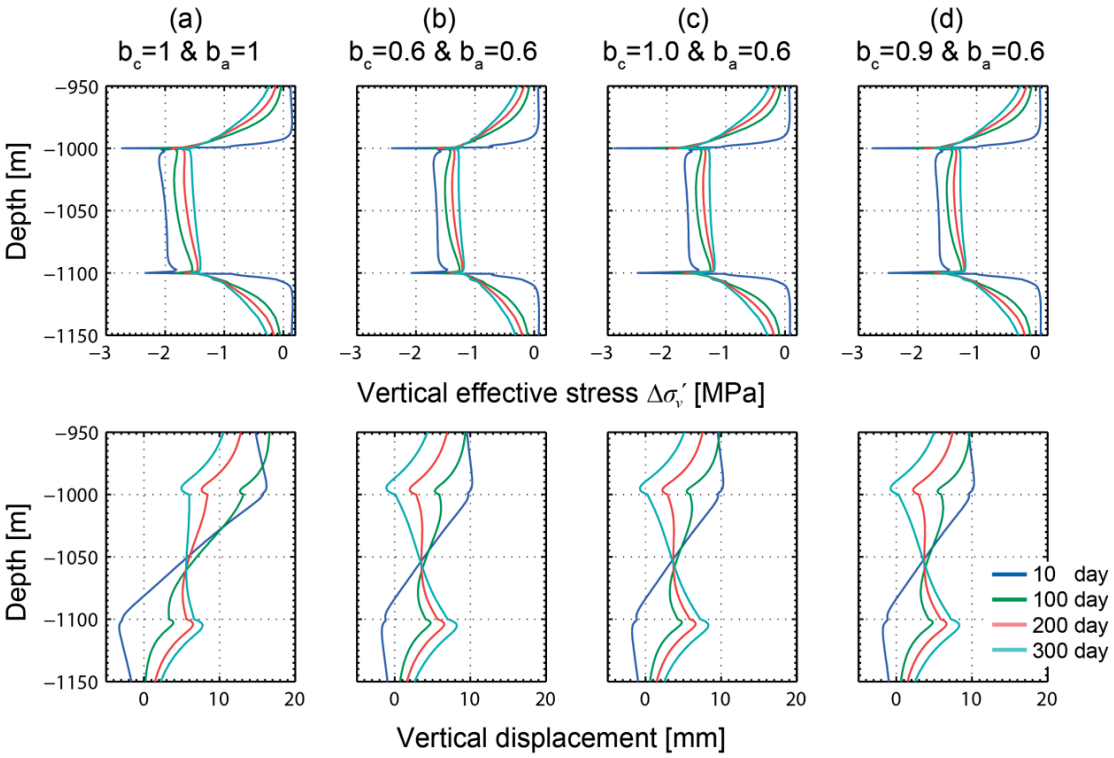

Figure 5.8 Effect of the Biot coefficient on the vertical effective stress variations and the vertical displacement 5 metres from the injection well.

5.9 Discussion on the failure threshold due to cooling injection of CO_2

Despite numerical studies of CO_2 injection that covers a series of material properties, as reviewed by Bao et al. (2013), an attempt to investigate the links between the thermal-hydro-mechanical coupled properties, thermal properties and failure thresholds are missing. Figure 5.9 displays the Mohr circle movement for simulations with different thermal-mechanical coupled coefficient settings for caprock in a normal faulting system, which means that the vertical effective stress is the maximum principle stress σ_1' and that the horizontal effective stress is the minimum principle stress σ_3'. Five Mohr circles after 100 days of injection for ratios $R = \frac{E_c\alpha_c}{1-2\upsilon_c} / \frac{E_a\alpha_a}{1-2\upsilon_a}$ ranging from 0.6 to 4 are synthesized in Figure 5.9.

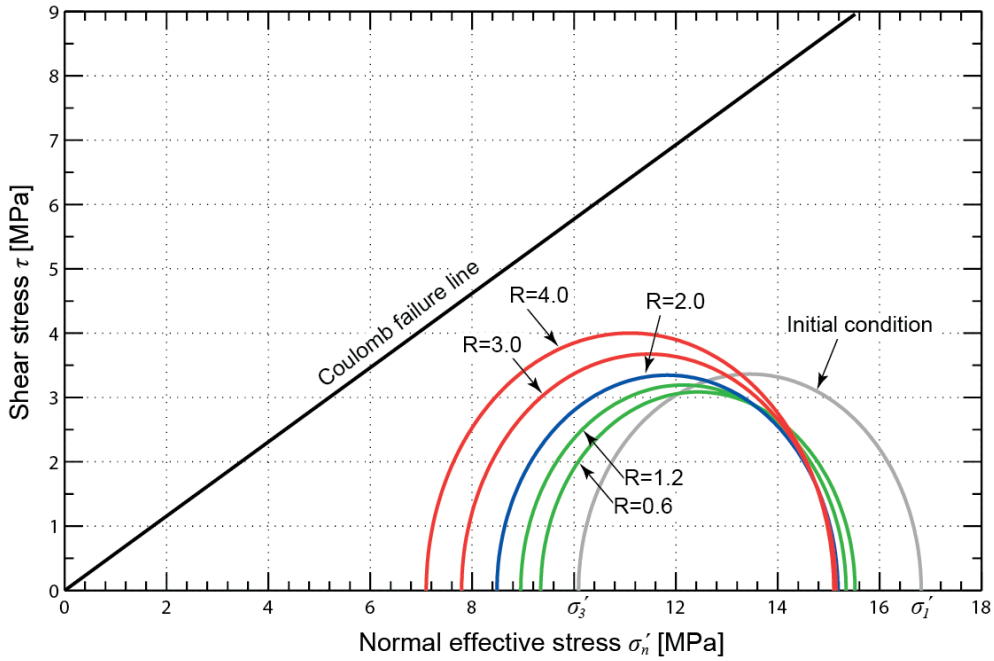

Figure 5.9 Influence of the material property combination ratio *R* on the Mohr circles after 100 days of injection and the Mohr circle of the initial condition at the aquifer-caprock interface and 5 metres from the injection well.

The decrease in the vertical effective stress in all of the cases is similar in magnitude, although the stress decreases in the horizontal direction are quite different from one case to another. This leads to a movement of the Mohr circles towards the failure line with either the shrinkage or expansion of the circles.

The circles for *R=0.6* and *R=1.2* are smaller than the initial one. We thus recover the conclusion of the study by Vilarrasa et al. (2013) in which the failure potential of caprock is reduced for material properties with a ratio *R=0.5*. A pure leftwards shifting of the circle for *R=2* and a proportional increase in the radius with an increase in the ratio *R* can be seen, which raises the failure potential. In the scenarios considered here for *R=3* and *4*, the Mohr circle expands significantly and is close to the failure line. This tendency confirms the concluding remark of Preisig and Prévost (2011) in which a high ratio, *R=3.1,* is involved. The results in Figure 5.9 reveals that when subjected to a low-temperature CO2 injection, caprock stability may be compromised for a stiffer caprock and a higher thermal expansion coefficient. Moreover, the failure potential is sensitive to the ratio *R* of the thermal-mechanical parameter in combination with the Young's modulus, Poisson's ratio and the thermal expansion coefficient. With a very stiff and thermal-mechanically sensitive caprock i.e., a higher Young's Modulus of the caprock and thermal coefficient, the caprock

stability is subjected to a high failure potential and may eventually reach failure the threshold if confronting a locally weak fractured zone in the caprock.

The Mohr circles in Figure 5.10 mark the effect of the hydromechanical coupled property - Biot coefficient on the failure threshold. The four cases used to produce Figure 5.8 are summarized here. All of the simulations have a ratio of *R=3*. The Mohr circles thereby move towards the failure line with expansion 100 days after injection. Despite the fact that the initial Mohr circle sizes are different because of the presence of the Biot coefficient in the definition of the effective stress in Eq. (4.35), the changes in size are quite similar for all of the cases. This observation is consistent with the aforementioned analysis that the thermal-mechanical coupling rather than the hydromechanical coupling primarily induces an effective stress reduction in the caprock. On the other hand, one can note that the failure potential for the lowest Biot coefficient set of the caprock and aquifer (red circles in Figure 10) is slightly larger than the other cases, as represented by the slightly higher slope of the red Coulomb failure line than that of the blue line. This observation implies that the thermal effect will more strongly affect the caprock stability if the hydromechanical coupling is attenuated.

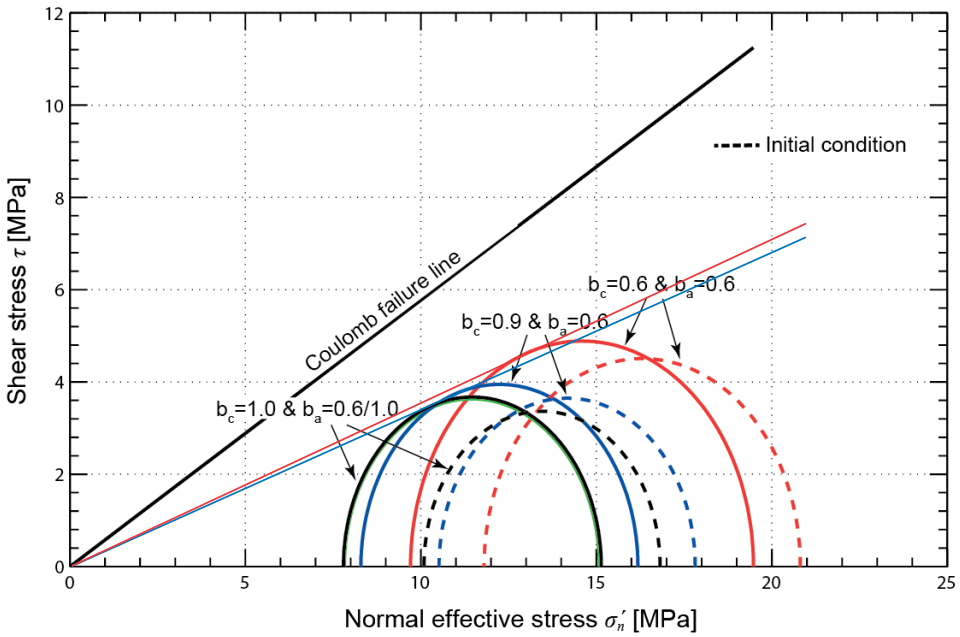

Figure 5.10 Influence of the Biot coefficients on the Mohr circles after 100 days of injection and the Mohr circle of the initial condition at the aquifer-caprock interface and 5 metres from the injection well.

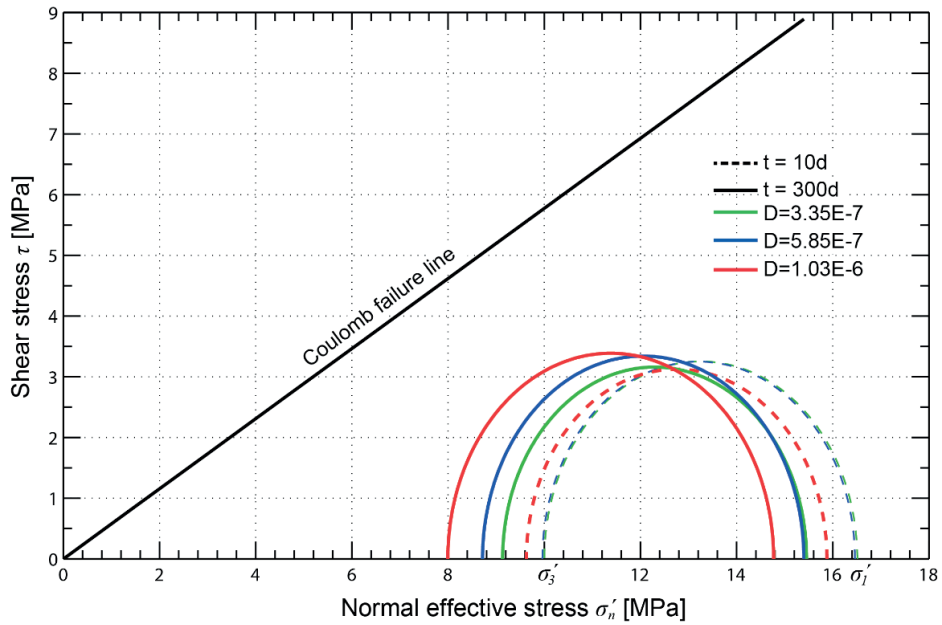

Figure 5.11 Influence of the caprock diffusivities on the Mohr circles at 5 metres further in the caprock and 5 metres from the injection well.

Figure 5.11 plots the Mohr circle evolutions with three thermal diffusivities for the case of *R=4*. The results presented in the remainder of the figure are obtained 5 metres above the caprock-aquifer interface (at 995m of depth) to clearly show the heat transfer. The superposition of the blue and green dashed circles shows that the stress states after 10 days of injection are equal for the case of D=3.35E-7 and D=5.85E-7. Both circles are also bigger than the red one for D=1.03E-6. This difference occurs because the caprock density for the case of D=1.03E-6 is smaller than those in the other two cases, thereby the initial vertical stress is smaller. The Mohr circle thus is smaller and initially on the left-hand side. The subsequent shifts in the three circles after ten days has identical magnitudes because of the same overpressure generation. After 300 days of injection, the cooling propagates through the caprock at rates according to the diffusivities. The temperature in the case of the highest conductivity D=1.03E-6 is 7°C lower than that of the lowest case for D=3.35E-7 (recall Figure 5.4). Consequently, the red circle (D=1.03E-6) expands the most even with its small initial size, because the horizontal stress decreases as the temperature decreases. A dilatation of the Mohr circle for D=5.85E-7 is also observed but with a smaller magnitude than the case of D=1.03E-6. Considering for this simulation time, the caprock with a lower thermal diffusivity suffers less cooling, and the mechanical stability thereby is less vulnerable. However, it needs to be pointed out that the failure potential remains the same

for all of the cases, and only a delay exists between a higher and lower diffusivity. The shrinkage of Mohr circle for D=3.35E-7 will eventually turn into an expansion with time.

5.10 Conclusions

The interaction between an aquifer and a sealing caprock was parametrically investigated. This study has revealed that heat transfer, thermal-mechanical and hydro-mechanical coupling parameters have a very strong influence on the mechanical stability of caprock. The ratio *R* of coupling parameters set (Young's modulus, Poisson's ratio and thermal expansion coefficient) between the caprock and aquifer is defined and use to indicate the caprock failure potential.

We presented results for coupling ratio *R=0.6* to *R=4.0,* which is the a range of parameters most suitable for materials associated with CO_2 injection projects. Previous studies (Vilarrasa et al., 2014, 2013) have shown that the low-temperature injection may increase caprock stability for *R<1* approximately. On the other hand, for a stiffer caprock with a higher thermal expansion coefficient, i.e., *R>4*, as in the study of Preisig and Prévost (2011), a failure is attained with an additional temperature drop. The present simulations are consistent with earlier predictions, which, in addition, emphasize that caprock with a higher ratio *R* has a higher potential for the failure and lower the mechanical stability.

Current numerical studies have been undertaken to assess aquifer performance and surface movement with a Biot coefficient equal to unity and without attention on the thermal diffusive properties. With an investigation into the experimental evidence, the present results complement earlier studies and extend for a range of geophysical conditions in which the coupled parameters and the heat transfer parameters are substantially valid in practice. A consideration of the aquifer's Biot coefficient is essential for properly estimating the expansion of the aquifer and eventually the surface movement. However, the consideration of the Biot coefficient for caprock in this study does not influence the results because no HM coupling processes occur inside the caprock. It is necessary to investigate if a higher permeable caprock is involved in the problem because the overpressure may penetrate and lead to the occurrence of HM processes within the caprock. In view of the thermal processes, the heat transfer and thermal-induced stress reduction within the caprock can be evaluated following 1D thermal flow theory, with the

temperature decreases in time following the nature of erfc $\left(\frac{1}{\sqrt{t}}\right)$. In addition, the thermal diffusive coefficient plays a major role in the time delay for preventing caprock from failure.

The high degree of coupled complex phenomena observed in this study leads to apparently paradoxical results such that a change in the thermal-mechanical coupling parameter combination (Young's modulus and thermal expansion coefficient) may reduce or improve caprock stability. For this reason, it is very risky to extrapolate the effects of a set of parameters to another situation in which the materials may have quite different properties, and there are also problems of different geometrical configurations. For the same reason, it is necessary to exercise special caution when averaging material properties over a wide range of values, especially when handling with coupled terms of the problem.

6 Concluding remarks

6.1 Summary of the main results achieved

This thesis was devoted to geomechanical modelling of CO_2 injection into deep aquifers. Emphasis was placed on a better understanding and prediction of the thermo-hydro-mechanical multiphase flow processes and associated mechanical responses of the reservoir. The main contributions of the presented thesis have been (i) to identify and understand the crucial processes arising from CO_2 injection into deep aquifers and (ii) to develop and evaluate both analytical and numerical tools for assessing coupled mechanisms, which are detailed hereafter and conclude the manuscript.

Hydromechanical coupled processes in a deep aquifer

A continuum modelling approach was proposed for the analysis of the hydro-mechanical process in deep aquifers subjected to CO_2 injection. The modelling framework extended the finite element code LAGAMINE to be capable of dealing with multiphase real fluid CO_2. A finite element of a deep conceptual aquifer is built to gauge the coupled processes involved during the injection. Numerical simulations are run to analyses the effects of hydromechanical couplings and injection strategies on the mechanical stabilities of the aquifer. The hydromechanical simulation results reveal that upon injection geomechanical instabilities originate from the fluid pressure accumulation within the aquifer, and most significant hydromechanical processes occur in the vicinity of the injection well, compromising the caprock integrity. The plastic zone is located at the top of the aquifer next to the injection well, where material damage may occur. Overpressure decreases as the water becomes desaturated by injected CO_2 and propagates along the aquifer as the injection continues.

Low-rate injection significantly reduces the fluid pressure accumulation within the aquifer. More interestingly progressively increasing the injection rate to the target value cannot limit the overpressure development significantly. Therefore, the caprock integrity may not be guaranteed by changing injection strategies. The analysis with a local failure indicator shows that shear failures along the aquifer-caprock interface are likely to occur if local fractures exist. The parametric studies also reveal that the permeability of the aquifer and the initial anisotropy stress factor K_0 are crucial to being evaluated before injection starts.

Thermo-hydro-mechanical assessment of a CO_2 storage site In Salah

The temperature of injected CO_2 is usually lower than the in-situ temperature, providing additional complexity to the hydromechanical coupling. A multiphase thermo-hydro-mechanical modelling approach is proposed on the basis of the hydromechanical framework. Numerical simulations were carried out with a 2D finite element reservoir model that is based on a real CO_2 storage project In Salah, Algeria over an injection period of four and a half years. Instead of solving fluid and thermal flow and injection induced geomechanical problem in a sequential manner, pore water pressure, CO_2 pressure, temperature and reservoir deformation were calculated simultaneously to assess the injection pressure and temperature induced geomechanical instabilities.

The stratigraphic geometry of the model represents a section that is perpendicular to the horizontal well based upon core analysis. A Van Genuchten water retention curve and Corey relative permeability functions are calibrated on the basis of available experimental data in the literature. Real log data measured on the field are used for the best estimation of input parameters. The blind prediction carried out by the thermo-hydro-mechanical simulation was in excellent accordance with real-time monitoring surface uplift at In Salah. Fluid pressures are governed by the high injection rate input, increasing nearly 8 MPa that is main responsible for the mean effective stress reduction and thereby surface uplift. The pressure increase affects nearly the entire aquifer whereas the temperature drops in the vicinity of the injection well. The temperature decrease leads not only to a volumetric contraction but also to a decrease in the effective horizontal stress that causes the additive generation of deviatoric stress. Modelling responses reveal that the combination of overpressure and cooling has a crucial influence on the potential development of shear failure in the caprock and the aquifer.

Effects of coupled parameters on caprock and aquifer stabilities

A fully coupled finite element model is established for assessing an aquifer-caprock system subjected to CO_2 injection through a vertical injection well. With an investigation into the experimental evidence, the present work that formulated an extensive parametric fully coupled study complement previous studies, extending them in a geophysical range of conditions where the coupled parameters and heat

transferring parameters are substantially valid in practice. A ratio of coupled parameters set (Young's modulus, Poisson's ratio and thermal expansion coefficient) between caprock and aquifer is defined and used as an indication of the caprock failure potential. The results demonstrate that the use of the ratio is consistent with the earlier predictions and can explain the contradictory concluding remarks of previous studies that are whether or not low-temperature injection will compromise the caprock stability.

The consideration of the aquifer's Biot coefficient is essential for properly estimating the expansion of the aquifer. For the case of a Biot coefficient close to 0.6, a reduction of nearly 40% in magnitude of overpressure effect on aquifer expansion is observed. However, the consideration of the Biot coefficient for low permeable caprock in this study does not have an influence on the results because no HM coupling processes occur inside the caprock. In view of the thermal processes, the heat transfer and thermal-induced stress reduction within the caprock can be evaluated following 1D thermal flow theory. The temperature decreases with time following the nature of erfc $\left(\frac{1}{\sqrt{t}}\right)$, and the horizontal effective stress thereby reduces accordingly. In addition, the thermal diffusive coefficient plays a major role in the time delay for preventing caprock from failure.

The high degree of coupled complex phenomena observed in this study leads to apparently paradoxical results such that a change in the thermo-hydro-mechanical coupled parameter combination (Young's modulus, Biot coefficient and thermal expansion coefficient) may reduce or improve caprock stability. For this reason, the effects presented with a set of parameters and a specific geometrical configuration are very risky to be extrapolated to another situation in which the materials may have quite different properties and problem geometry are different too. For the same reason, it is necessary to exercise special caution when averaging material properties over a wide range of values, especially when handling the coupled terms of the problem.

Determination of caprock deformation and surface uplift on the basis of analytical considerations

The injection of CO_2 pressurizes the reservoir and causes caprock deflection, which further results in surface uplift. The nearly impermeable caprock limit the occurrence of overpressure within the aquifer. Adopting both observations, analytical resolution of the plate theory with the abrupt interface theory led to two closed-form analytical solutions that are validated against in-situ monitoring data at In Salah as well as finite element modelling results. By incorporating elastic properties of the reservoir system and the real thermodynamic properties of CO_2 and brine, the temporal and spatial evolution of caprock deformation and surface uplift can be obtained readily. Furthermore, the use of two solutions allows assessing uncertainty in essential parameters for a CO_2 storage project such as the injection rate, porosity, rock properties and geological structures.

In view of the computational approaches, the analytical development considers a semi-infinite domain that omits the limitation of boundary value problem. For a detailed numerical study, the analytical consideration can offer the basis for boundary establishment both on the mechanical deformation and fluid pressure propagation. In addition, this development allows incorporate any fluid injection-induced pressurization distribution functions in a straightforward way. Thus, advances in hydrology research can be integrated easily, and the current development can be extended to any fluid injection and extraction problem. The proposed approach offers a practical solution for determination of caprock and surface deformation, candidate site evaluation and sensitivity analysis of essential parameters. Two solutions can be considered as one of most efficient and accurate design tool for estimating the influence of high injection rates of CO_2 on surface uplift and caprock deformation, which account for the hydraulic and mechanical properties of the reservoir and real CO_2 properties.

6.2 Future perspectives

The analytical and numerical developments obtained in this work placed focus on continuum modelling of the thermo-hydro-mechanical impact on the aquifer and caprock in a CO_2 storage site. With respect to the framework of the present work, several analytical and numerical developments are recommended below for fulfilling the gaps between the current state of research and the need for understanding the coupled processes during CO_2 injection into deep aquifers.

The current analytical approach considers linear elasticity to evaluate the interaction between aquifer and caprock. The mechanical description of reservoir rocks can be further extended to as a non-linear elasticity, or elasto-damage constitutive model to enlarge the applicability of the current solutions.

3D extension of the current analytical development is potential. Instead of Bessel integration, the inverse Laplace transform and Bromwich integral are suggested to be employed to solve the governing equations. Such development can allow reservoir performance assessment with a more realistic geometrical configuration.

Numerical simulations of reservoir responses in a 2D plain strain and an axisymmetric configuration led to the limitation such that responses cannot be accurately reproduced in the cases of horizontal well injection and multi-well injection due to boundary effects. Additional finite element simulations with a 3D reservoir model are recommended to quantify the pressure and thermal influence in a real configuration.

An approach that integrates both the analytical and numerical developments can be envisaged. Design and risk assessment for a CO_2 storage site are often performed by means of numerical simulations. Using numerical methods can be very time consuming for a reservoir scale. On the other hand, analytical models are very efficient but less accurate in the zone where most complex coupled processes occur. The integration of both can increase the accuracy of analytical computation whereas computational effort of numerical simulations can be reduced.

The interface between caprock and aquifer as well as pre-existing faults in the reservoir are crucial locations where CO may leak through fractures and faults that are initiated or opened by pressurization. Consideration of different contact regimes between different media will be useful for assessment of potential shearing, relative movement and mutual interaction with fluid flow. Current advances in interface modelling can be extended to two-phase flow with mechanical consideration and further allow the consideration of variation of the interface permeability, fluid storage due to the fault/fracture opening as well as the thermal influence (e.g. Cerfontaine et al., 2015).

The occurrence of salt precipitation in the pore throats is observed from laboratory experiments on the cores (Grude et al., 2013). The salt precipitation restricts fluid flows and causes eventually an additional pressure build-up (Espinoza et al., 2011; White et al., 2015). To enhance the successful implementation of geological sequestration of CO_2 in deep brine aquifer, it requires an in-depth understanding of the issues arising from coupled Thermo-Hydro-Chemo-Mechanical (THMC) processes that will affect both short-term and long-term reliability of the endeavours, including thermal flow, multiphase fluid flow, geomechanical response and geochemical reactions. This development is currently being carried out by the author and Prof. Lyesse Laloui at Laboratory of Soil Mechanics at EPFL, which is intended to account for coupled integration of individual element of the salt precipitation due to CO_2 drying-out (Spycher et al., 2003), the redistribution of stress with the presence of precipitated salts (Osselin et al., 2015), the dissolution of important minerals in the water, the interaction between CO_2 and water, thermal effect and geomechanical deformation.

7 References

Alonso, J., Navarro, V., Calvo, B., 2012. Flow path development in different CO2 storage reservoir scenarios. Engineering Geology 127, 54–64. doi:10.1016/j.enggeo.2012.01.001

André, L., Azaroual, M., Menjoz, A., 2009. Numerical Simulations of the Thermal Impact of Supercritical CO2 Injection on Chemical Reactivity in a Carbonate Saline Reservoir. Transport in Porous Media 82, 247–274. doi:10.1007/s11242-009-9474-2

Andreani, M., Gouze, P., Luquot, L., Jouanna, P., 2008. Changes in seal capacity of fractured claystone caprocks induced by dissolved and gaseous CO 2 seepage. Geophysical Research Letters 35, L14404. doi:10.1029/2008GL034467

Armitage, P.J., Faulkner, D.R., Worden, R.H., Aplin, a. C., Butcher, a. R., Iliffe, J., 2011. Experimental measurement of, and controls on, permeability and permeability anisotropy of caprocks from the CO 2 storage project at the Krechba Field, Algeria. Journal of Geophysical Research 116, B12208. doi:10.1029/2011JB008385

Bacci, G., Korre, A., Durucan, S., 2011. Experimental investigation into salt precipitation during CO2 injection in saline aquifers, in: Energy Procedia. pp. 4450–4456. doi:10.1016/j.egypro.2011.02.399

Bachu, S., 2000. Sequestration of CO2 in geological media: criteria and approach for site selection in response to climate change. Energy Conversion and Management 41, 953–970. doi:10.1016/S0196-8904(99)00149-1

Bachu, S., Adams, J.J., 2003. Sequestration of CO2 in geological media in response to climate change: capacity of deep saline aquifers to sequester CO2 in solution. Energy Conversion and Management 44, 3151–3175. doi:10.1016/S0196-8904(03)00101-8

Bachu, S., Bennion, B., 2007. Effects of in-situ conditions on relative permeability characteristics of CO2-brine systems. Environmental Geology 54, 1707–1722. doi:10.1007/s00254-007-0946-9

Bao, J., Hou, Z., Fang, Y., Ren, H., Lin, G., 2013. Uncertainty quantification for evaluating impacts of caprock and reservoir properties on pressure buildup and ground surface displacement during geological CO 2 sequestration. Greenhouse Gases: Science and Technology 3, 338–358. doi:10.1002/ghg.1362

Barnichon, J.D., Charlier, R., 1996. Finite element modelling of the competition between shear bands in the early stages of thrusting: Strain localization analysis and constitutive law influence. Geological Society, London, Special Publications 99, 235–250. doi:10.1144/GSL.SP.1996.099.01.18

Batzle, M., Wang, Z., 1992. Seismic properties of pore fluids. Geophysics 57, 1396 – 1408.

doi:10.1190/1.1443207

Bear, J., 1972. Dynamics of Fluids in Porous Media. Elsevier, New York, USA.

Benson, S.M., Cole, D.R., 2008. CO2 Sequestration in Deep Sedimentary Formations. Elements 4, 325–331. doi:10.2113/gselements.4.5.325

Birkholzer, J.T., Oldenburg, C.M., Zhou, Q., 2015. CO2 migration and pressure evolution in deep saline aquifers. International Journal of Greenhouse Gas Control 40, 203–220. doi:10.1016/j.ijggc.2015.03.022

Bissell, R.C., Vasco, D.W., Atbi, M., Hamdani, M., Okwelegbe, M., Goldwater, M.H., 2011. A full field simulation of the in Salah gas production and CO2 storage project using a coupled geo-mechanical and thermal fluid flow simulator. Energy Procedia 4, 3290–3297. doi:10.1016/j.egypro.2011.02.249

Blackwell, D., Steele, J., 1989. Thermal Conductivity of Sedimentary Rocks: Measurement and Significance, in: Naeser, N., McCulloh, T. (Eds.), Thermal History of Sedimentary Basins SE - 2. Springer New York, pp. 13–36. doi:10.1007/978-1-4612-3492-0_2

Bohloli, B., Aker, E., Cuisiat, F., Oye, V., Khn, D., 2012. Analysis of Pressure Versus Flow Regime of CO2 To Assess Matrix and Fracture Injection at In Salah , Algeria, in: Third EAGE CO2 Geological Storage Workshop. pp. 26–28.

Bohloli, B., Bjørnarå, T.I., Grande, L., Park, J., Oye, V., Kühn, D., Rucci, A., 2013. Geomechanical Assessment of Ground Surface Uplift due to CO2 Storage at In Salah, Algeria, in: International EAGE Workshop on Geomechanics and Energy. doi:10.3997/2214-4609.20131984

Böttcher, N., Singh, A.K., Kolditz, O., Liedl, R., 2012a. Non-isothermal, compressible gas flow for the simulation of an enhanced gas recovery application. Journal of Computational and Applied Mathematics 236, 4933–4943. doi:10.1016/j.cam.2011.11.013

Böttcher, N., Taron, J., Kolditz, O., Park, C.-H., Liedl, R., 2012b. Evaluation of thermal equations of state for CO2 in numerical simulations. Environmental Earth Sciences 67, 481–495. doi:10.1007/s12665-012-1704-1

Bouteca, M.J., Bary, D., Piau, J.M., Kessler, N., Boisson, M., Fourmaintraux, D., 2013. Contribution of poroelasticity to reservoir engineering: Lab experiments, application to core decompression and implication in HP-HT reservoirs depletion, in: Rock Mechanics in Petroleum Engineering. Society of Petroleum Engineers. doi:10.2118/28093-MS

Bowen, R.M., 1982. Compressible porous media models by use of the theory of mixtures. International Journal of Engineering Science 20, 697–735. doi:10.1016/0020-7225(82)90082-9

Bradshaw, J., Dance, T., 2005. Mapping geological storage prospectivity of CO_2 for the world's sedimentary basins and regional source to sink matching.

Bryant, E., 1997. Climate Process and Change. Cambridge University Press, 1997, Cambridge, UK.

Busch, a, Alles, S., Gensterblum, Y., Prinz, D., Dewhurst, D., Raven, M., Stanjek, H., Krooss, B.M., 2008. Carbon dioxide storage potential of shales. International Journal of Greenhouse Gas Control 2, 297–308. doi:10.1016/j.ijggc.2008.03.003

Cappa, F., Rutqvist, J., 2011. Modeling of coupled deformation and permeability evolution during fault reactivation induced by deep underground injection of CO2. International Journal of Greenhouse Gas Control 5, 336–346. doi:10.1016/j.ijggc.2010.08.005

Cerfontaine, B., Dieudonné, A.C., Radu, J.P., Collin, F., Charlier, R., 2015. 3D zero-thickness coupled interface finite element: Formulation and application. Computers and Geotechnics 69, 124–140. doi:10.1016/j.compgeo.2015.04.016

Charlier, R., Radu, J.-P., Collin, F., 2011. Numerical modelling of coupled transient phenomena. Revue Française de Génie Civil 5, 719–743.

Chevalier, G., Diamond, L.W., Leu, W., 2010. Potential for deep geological sequestration of CO2 in Switzerland: a first appraisal. Swiss Journal of Geosciences 103, 427–455. doi:10.1007/s00015-010-0030-4

Class, H., Ebigbo, A., Helmig, R., Dahle, H.K., Nordbotten, J.M., Celia, M. a., Audigane, P., Darcis, M., Ennis-King, J., Fan, Y., Flemisch, B., Gasda, S.E., Jin, M., Krug, S., Labregere, D., Naderi Beni, A., Pawar, R.J., Sbai, A., Thomas, S.G., Trenty, L., Wei, L., 2009. A benchmark study on problems related to CO2 storage in geologic formations. Computational Geosciences 13, 409–434. doi:10.1007/s10596-009-9146-x

Collin, F., 2003. Couplages thermo-hydro-mécaniques dans les sols et les roches tendres partiellement saturés. University of Liège, Belgium.

Crovetto, R., 1991. Evaluation of Solubility CO2-H2O. Journal of Physical and Chemical Reference Data 20, 575–589. doi:10.1063/1.555905

De Silva, P.N.K., Ranjith, P.G., 2012. A study of methodologies for CO2 storage capacity estimation of saline aquifers. Fuel 93, 13–27. doi:10.1016/j.fuel.2011.07.004

Dentz, M., Tartakovsky, D.M., 2009. Response to "Comments on Abrupt-Interface

Solution for Carbon Dioxide Injection into Porous Media by Dentz and Tartakovsky (2008)" by Lu et al. Transport in Porous Media 79, 39–41. doi:10.1007/s11242-009-9363-8

Dentz, M., Tartakovsky, D.M., 2008. Abrupt-Interface Solution for Carbon Dioxide Injection into Porous Media. Transport in Porous Media 79, 15–27. doi:10.1007/s11242-008-9268-y

Eppelbaum, L., Kutasov, I., Pilchin, A., 2014. Thermal Properties of Rocks and Density of Fluids, in: Applied Geothermics. Springer Berlin Heidelberg, pp. 99–149. doi:10.1007/978-3-642-34023-9

Espinoza, D.N., Kim, S.H., Santamarina, J.C., 2011. CO2 geological storage — Geotechnical implications. KSCE Journal of Civil Engineering 15, 707–719. doi:10.1007/s12205-011-0011-9

Fang, Y., Nguyen, B.N., Carroll, K., Xu, Z., Yabusaki, S.B., Scheibe, T.D., Bonneville, A., 2013. Development of a coupled thermo-hydro-mechanical model in discontinuous media for carbon sequestration. International Journal of Rock Mechanics and Mining Sciences 62, 138–147. doi:10.1016/j.ijrmms.2013.05.002

Fenghour, A., Wakeham, W.A., Vesovic, V., 1998. The Viscosity of Carbon Dioxide. Journal of Physical and Chemical Reference Data 27, 31. doi:10.1063/1.556013

Ferronato, M., Gambolati, G., Janna, C., Teatini, P., 2010. Geomechanical issues of anthropogenic CO2 sequestration in exploited gas fields. Energy Conversion and Management 51, 1918–1928. doi:10.1016/j.enconman.2010.02.024

Fjar, E., Holt, R.M., Raaen, A.M., Risnes, R., Horsrud, P., 2008. Petroleum Related Rock Mechanics: 2nd Edition. Elsevier.

Gaus, I., 2010. Role and impact of CO2–rock interactions during CO2 storage in sedimentary rocks. International Journal of Greenhouse Gas Control 4, 73–89. doi:10.1016/j.ijggc.2009.09.015

Geertsma, J., 1973. Land Subsidence Above Compacting Oil and Gas Reservoirs. Journal of Petroleum Technology 25, 734–744. doi:10.2118/3730-PA

Geertsma, J., 1966. Problems of Rock Mechanics In Petroleum Production Engineering, in: 1st ISRM Congress. International Society for Rock Mechanics.

Gerard, P., Charlier, R., Chambon, R., Collin, F., 2008. Influence of evaporation and seepage on the convergence of a ventilated cavity. Water Resources Research 44, n/a–n/a. doi:10.1029/2007WR006500

Gilliam, T.M., Morgan, T.M., 1987. Shale: Measurement of Thermal Properties (No.

ORNL/TM-10499). Oak Ridge National Lab., TN (USA). Oak Ridge, Tennessee.

Giorgis, T., Carpita, M., Battistelli, A., 2007. 2D modeling of salt precipitation during the injection of dry CO2 in a depleted gas reservoir. Energy Conversion and Management 48, 1816–1826. doi:10.1016/j.enconman.2007.01.012

Gor, G.Y., Elliot, T.R., Prévost, J.H., 2013. Effects of thermal stresses on caprock integrity during CO2 storage. International Journal of Greenhouse Gas Control 12, 300–309. doi:10.1016/j.ijggc.2012.11.020

Grude, S., Landrø, M., Osdal, B., 2013. Time-lapse pressure–saturation discrimination for CO2 storage at the Snøhvit field. International Journal of Greenhouse Gas Control 19, 369–378. doi:10.1016/j.ijggc.2013.09.014

Guy, N., Seyedi, D.M., Hild, F., 2010. Hydro-mechanical modelling of geological CO 2 storage and the study of possible caprock fracture mechanisms. Georisk: Assessment and Management of Risk for Engineered Systems and Geohazards 4, 110–117. doi:10.1080/17499511003676663

Han, W.S., Stillman, G.A., Lu, M., Lu, C., McPherson, B.J., Park, E., 2010. Evaluation of potential nonisothermal processes and heat transport during CO2 sequestration. Journal of Geophysical Research 115, B07209. doi:10.1029/2009JB006745

Iding, M., Ringrose, P., 2010. Evaluating the impact of fractures on the performance of the In Salah CO2 storage site. International Journal of Greenhouse Gas Control 4, 242–248. doi:10.1016/j.ijggc.2009.10.016

IEA/OECD, 1994. IEA/OECD scoping study: energy and environmental technologies to respond to global climate change concerns. IEA [etc.], Paris.

Jamieson, D.T., Tudhope, J.S., Morris, R., Cartwright, G., 1969. Physical properties of sea water solutions: heat capacity. Desalination 7, 23–30. doi:10.1016/S0011-9164(00)80271-4

Jiang, X., 2011. A review of physical modelling and numerical simulation of long-term geological storage of CO2. Applied Energy 88, 3557–3566. doi:10.1016/j.apenergy.2011.05.004

Jobmann, M., Polster, M., 2007. The response of Opalinus clay due to heating: A combined analysis of in situ measurements, laboratory investigations and numerical calculations. Physics and Chemistry of the Earth, Parts A/B/C 32, 929–936. doi:10.1016/j.pce.2006.03.014

Kharaka, Y.K., Cole, D.R., Hovorka, S.D., Gunter, W.D., Knauss, K.G., Freifeld, B.M., 2006. Gas-water-rock interactions in Frio Formation following CO2 injection:

Implications for the storage of greenhouse gases in sedimentary basins. Geology 34, 577. doi:10.1130/G22357.1

Laloui, L., Nuth, M., 2009. On the use of the generalised effective stress in the constitutive modelling of unsaturated soils. Computers and Geotechnics 36, 20–23. doi:10.1016/j.compgeo.2008.03.002

Lewis, R.W., Schrefler, B.A., 1998. The finite element method in the static and dynamic deformation and consolidation of porous media. Second Edition. Wiley, Chichester, UK.

Li, C., Barès, P., Laloui, L., 2015. A hydromechanical approach to assess CO2 injection-induced surface uplift and caprock deflection. Geomechanics for Energy and the Environment 4, 51–60. doi:10.1016/j.gete.2015.06.002

Li, Q., Wu, Z., Murakami, Y., Satoh, T., Lei, X., 2005. Hydraulic and geomechanical simulation of fractured porous media under geo-sequestration of carbon dioxide, in: Younane N, A., Cheung, A.H.-D., Franz-Josef, U. (Eds.), Poromechanics III - Biot Centennial (1905-2005). CRC Press, p. 828.

Lin, C.K., 2008. Algorithm for determining optimum sequestration depth of CO 2 trapped by residual gas and solubility trapping mechanisms in a deep saline formation. Geofluids 8, 333–343. doi:10.1111/j.1468-8123.2008.00221.x

Longuemare, P., Mainguy, M., Lemonnier, P., Onaisi, A., Gérard, C., Koutsabeloulis, N., 2002. Geomechanics in Reservoir Simulation: Overview of Coupling Methods and Field Case Study. Oil & Gas Science and Technology 57, 471–483. doi:10.2516/ogst:2002031

Lu, C., Lee, S.-Y., Han, W.S., McPherson, B.J., Lichtner, P.C., 2009. Comments on "Abrupt-Interface Solution for Carbon dioxide Injection into Porous Media" by M. Dentz and D. Tartakovsky. Transport in Porous Media 79, 29–37. doi:10.1007/s11242-009-9362-9

Lu, M., Connell, L., 2008. Non-isothermal flow of carbon dioxide in injection wells during geological storage. International Journal of Greenhouse Gas Control 2, 248–258. doi:10.1016/S1750-5836(07)00114-4

Mathias, S.A., Hardisty, P.E., Trudell, M.R., Zimmerman, R.W., 2008. Approximate Solutions for Pressure Buildup During CO2 Injection in Brine Aquifers. Transport in Porous Media 79, 265–284. doi:10.1007/s11242-008-9316-7

Mathieson, A., Midgely, J., Wright, I., Saoula, N., Ringrose, P., 2011. In Salah CO2 Storage JIP: CO2 sequestration monitoring and verification technologies applied at

Krechba, Algeria. Energy Procedia 4, 3596–3603. doi:10.1016/j.egypro.2011.02.289

Metz, B., Davidson, O., de Coninck, H., Loos, M., Meyer, L., 2005. IPCC Special Report on Carbon Dioxide Capture and Storage, IPCC. doi:10.1002/anie.201000431

Michael, K., Golab, A., Shulakova, V., Ennis-King, J., Allinson, G., Sharma, S., Aiken, T., 2010. Geological storage of CO2 in saline aquifers—A review of the experience from existing storage operations. International Journal of Greenhouse Gas Control 4, 659–667. doi:10.1016/j.ijggc.2009.12.011

Morris, J.P., Hao, Y., Foxall, W., McNab, W., 2011. A study of injection-induced mechanical deformation at the In Salah CO2 storage project. International Journal of Greenhouse Gas Control 5, 270–280. doi:10.1016/j.ijggc.2010.10.004

Mukhopadhyay, S., Yang, S.-Y., Yeh, H.-D., 2011. Pressure Buildup During Supercritical Carbon Dioxide Injection From a Partially Penetrating Borehole into Gas Reservoirs. Transport in Porous Media 91, 889–911. doi:10.1007/s11242-011-9879-6

Nicol, a., Carne, R., Gerstenberger, M., Christophersen, a., 2011. Induced seismicity and its implications for CO2 storage risk. Energy Procedia 4, 3699–3706. doi:10.1016/j.egypro.2011.02.302

Nordbotten, J.M., Celia, M. a., Bachu, S., 2005. Injection and Storage of CO2 in Deep Saline Aquifers: Analytical Solution for CO2 Plume Evolution During Injection. Transport in Porous Media 58, 339–360. doi:10.1007/s11242-004-0670-9

Nur, A., Byerlee, J.D., 1971. An exact effective stress law for elastic deformation of rock with fluids. Journal of Geophysical Research 76, 6414. doi:10.1029/JB076i026p06414

Nuth, M., Laloui, L., Schrefler, B.A., 2010. Analysis of compaction phenomena due to water injection in reservoirs with a three-phase geomechanical model. Journal of Petroleum Science and Engineering 73, 33–40. doi:10.1016/j.petrol.2010.05.005

Office fédéral de L'énergie, O., 2015. Energie nucléaire [WWW Document]. URL http://www.bfe.admin.ch/themen/00511/index.html?lang=fr (accessed 12.4.15).

Oldenburg, C.M., 2007. Joule-Thomson cooling due to CO2 injection into natural gas reservoirs. Energy Conversion and Management 48, 1808–1815. doi:10.1016/j.enconman.2007.01.010

Onuma, T., Ohkawa, S., 2009. Detection of surface deformation related with CO2 injection by DInSAR at In Salah, Algeria. Energy Procedia 1, 2177–2184. doi:10.1016/j.egypro.2009.01.283

Orlic, B., 2009. Some geomechanical aspects of geological CO2 sequestration. KSCE

Journal of Civil Engineering 13, 225–232. doi:10.1007/s12205-009-0225-2

Osselin, F., Fabbri, A., Fen-Chong, T., Dangla, P., Pereira, J.-M., Lassin, A., 2015. Stress from NaCl crystallisation by carbon dioxide injection in aquifers. Environmental Geotechnics 2, 280–291. doi:10.1680/envgeo.13.00057

Ouellet, A., Bérard, T., Desroches, J., Frykman, P., Welsh, P., Minton, J., Pamukcu, Y., Hurter, S., Schmidt-Hattenberger, C., 2011. Reservoir geomechanics for assessing containment in CO2 storage: A case study at Ketzin, Germany. Energy Procedia 4, 3298–3305. doi:10.1016/j.egypro.2011.02.250

Oye, V., Aker, E., Daley, T.M., Kühn, D., Bohloli, B., Korneev, V., 2013. Microseismic Monitoring and Interpretation of Injection Data from the in Salah CO2 Storage Site (Krechba), Algeria. Energy Procedia 37, 4191–4198. doi:10.1016/j.egypro.2013.06.321

Oye, V., Zhao, P., Khn, D., Iranpour, K., Aker, E., Bohloli, B., 2012. Monitoring of the In Salah CO2 Storage Site (Krechba) Using Microseismic Data Analysis, in: Third EAGE CO2 Geological Storage Workshop. pp. 27–29.

Panday, S., Corapcioglu, M.Y., 1989. Reservoir transport equations by compositional approach. Transport in Porous Media 4, 369–393. doi:10.1007/BF00165780

Pasquale, V., Gola, G., Chiozzi, P., Verdoya, M., 2011. Thermophysical properties of the Po Basin rocks. Geophysical Journal International 186, 69–81. doi:10.1111/j.1365-246X.2011.05040.x

Peng, D.-Y., Robinson, D.B., 1976. A New Two-Constant Equation of State. Industrial & Engineering Chemistry Fundamentals 15, 59–64. doi:10.1021/i160057a011

Poling, B.E., Prausnitz, J.M., O'Connell, J.P., 2000. The properties of gases and liquids, Fifth Edition. McGraw Hill Book Co., New York, NY, New York, Chicago, San Francisco, Athens, London, Madrid, Mexico City, Milan, New Delhi, Singapore, Sydney, Toronto. doi:10.1036/0070116822

Preisig, M., Prévost, J.H., 2011. Coupled multi-phase thermo-poromechanical effects. Case study: CO2 injection at In Salah, Algeria. International Journal of Greenhouse Gas Control 5, 1055–1064. doi:10.1016/j.ijggc.2010.12.006

Prévost, J.H., 2013. One-Way versus Two-Way Coupling in Reservoir-Geomechanical Models (ASCE), in: Poromechanics V. pp. 517–526. doi:http://dx.doi.org/10.1061/9780784412992.061

Pruess, K., García, J., 2002. Multiphase flow dynamics during CO 2 disposal into saline aquifers. Environmental Geology 42, 282–295. doi:10.1007/s00254-001-0498-3

Reichle, D., Houghton, J., Kane, B., Ekmann, J., 1999. Carbon sequestration research and development (DOE/SC/FE-1). Oak Ridge, Tennessee. doi:10.2172/810722

Rinaldi, A.P., Rutqvist, J., 2013. Modeling of deep fracture zone opening and transient ground surface uplift at KB-502 CO2 injection well, In Salah, Algeria. International Journal of Greenhouse Gas Control 12, 155–167. doi:10.1016/j.ijggc.2012.10.017

Ringrose, P.S., Mathieson, A.S., Wright, I.W., Selama, F., Hansen, O., Bissell, R., Saoula, N., Midgley, J., 2013. The In Salah CO2 Storage Project: Lessons Learned and Knowledge Transfer. Energy Procedia 37, 6226–6236. doi:10.1016/j.egypro.2013.06.551

Robertson, E.C., 1988. Thermal Properties of Rocks. US Department of the Interior: Geological Survey 88–441.

Robertson, E.C., Peck, D.L., 1974. Thermal conductivity of vesicular basalt from Hawaii. Journal of Geophysical Research 79, 4875–4888. doi:10.1029/JB079i032p04875

Rohmer, J., Seyedi, D.M., 2010. Coupled Large Scale Hydromechanical Modelling for Caprock Failure Risk Assessment of CO 2 Storage in Deep Saline Aquifers. Oil & Gas Science and Technology – Revue de l'Institut Français du Pétrole 65, 503–517. doi:10.2516/ogst/2009049

Rutqvist, J., 2012. The Geomechanics of CO2 Storage in Deep Sedimentary Formations. Geotechnical and Geological Engineering 30, 525–551. doi:10.1007/s10706-011-9491-0

Rutqvist, J., Birkholzer, J.T., Cappa, F., Tsang, C.-F., 2007. Estimating maximum sustainable injection pressure during geological sequestration of CO 2 using coupled fluid flow and geomechanical fault-slip analysis. Energy Conversion and Management 48, 1798–1807. doi:10.1016/j.enconman.2007.01.021

Rutqvist, J., Birkholzer, J.T., Tsang, C.-F., 2008. Coupled reservoir–geomechanical analysis of the potential for tensile and shear failure associated with CO2 injection in multilayered reservoir–caprock systems. International Journal of Rock Mechanics and Mining Sciences 45, 132–143. doi:10.1016/j.ijrmms.2007.04.006

Rutqvist, J., Tsang, C.-F., 2002. A study of caprock hydromechanical changes associated with CO 2 -injection into a brine formation. Environmental Geology 42, 296–305. doi:10.1007/s00254-001-0499-2

Rutqvist, J., Vasco, D.W., Myer, L., 2010. Coupled reservoir-geomechanical analysis of CO2 injection and ground deformations at In Salah, Algeria. International Journal of Greenhouse Gas Control 4, 225–230. doi:10.1016/j.ijggc.2009.10.017

Saripalli, P., McGrail, P., 2002. Semi-analytical approaches to modeling deep well injection of CO2 for geological sequestration. Energy Conversion and Management 43, 185–198. doi:10.1016/S0196-8904(01)00017-6

Schäfer, F., Walter, L., Class, H., Müller, C., 2012. The regional pressure impact of CO2 storage: a showcase study from the North German Basin. Environmental Earth Sciences 65, 2037–2049. doi:10.1007/s12665-011-1184-8

Scheidegger, A.E., 1958. The Physics of Flow Through Porous Media. Soil Science 86, 355.

Segall, P., Grasso, J.-R., Mossop, A., 1994. Poroelastic stressing and induced seismicity near the Lacq gas field, southwestern France. Journal of Geophysical Research 99, 15423. doi:10.1029/94JB00989

Selvadurai, A.P.S., 2009. Heave of a surficial rock layer due to pressures generated by injected fluids. Geophysical Research Letters 36, L14302. doi:10.1029/2009GL038187

Selvadurai, A.P.S., 2008. Mechanics of an embedded caprock layer during pressurization of a CO2 storage reservoir, in: S. Pietruszczak, G.N. Pande, C.T. and R.W. (Ed.), Proceedings of ComGeo 09: Computational Geomechanics I. pp. 466–475.

Selvadurai, A.P.S., 2000. Partial Differential Equations in Mechanics 2: The Biharmonic Equation, Poisson's Equation. Springer. doi:10.1007/978-3-662-09205-7

Shalabi, F.I., Cording, E.J., Al-Hattamleh, O.H., 2007. Estimation of rock engineering properties using hardness tests. Engineering Geology 90, 138–147. doi:10.1016/j.enggeo.2006.12.006

Shampine, L.F., 2008. Vectorized adaptive quadrature in MATLAB. Journal of Computational and Applied Mathematics 211, 131–140. doi:10.1016/j.cam.2006.11.021

Shi, J.-Q., Sinayuc, C., Durucan, S., Korre, A., 2012. Assessment of carbon dioxide plume behaviour within the storage reservoir and the lower caprock around the KB-502 injection well at In Salah. International Journal of Greenhouse Gas Control 7, 115–126. doi:10.1016/j.ijggc.2012.01.002

Shukla, R., Ranjith, P., Haque, A., Choi, X., 2010. A review of studies on CO2 sequestration and caprock integrity. Fuel 89, 2651–2664. doi:10.1016/j.fuel.2010.05.012

Siggins, A.F., 2003. Saturation, pore pressure and effective stress from sandstone acoustic properties. Geophysical Research Letters 30, 10–13. doi:10.1029/2002GL016143

Song, J., Zhang, D., 2013. Comprehensive review of caprock-sealing mechanisms for geologic carbon sequestration. Environmental science & technology 47, 9–22. doi:10.1021/es301610p

Span, R., Wagner, W., 1996. A New Equation of State for Carbon Dioxide Covering the Fluid Region from the Triple-Point Temperature to 1100 K at Pressures up to 800 MPa. Journal of Physical and Chemical Reference Data 25, 1509. doi:10.1063/1.555991

Spycher, N., Pruess, K., Ennis-King, J., 2003. CO2-H2O mixtures in the geological sequestration of CO2. I. Assessment and calculation of mutual solubilities from 12 to 100°C and up to 600 bar. Geochimica et Cosmochimica Acta 67, 3015–3031. doi:10.1016/S0016-7037(03)00273-4

Spycher, N., Reed, M.H., 1988. Fugacity coefficients of H2, CO2, CH4, H2O and of H2O-CO2-CH4 mixtures: A virial equation treatment for moderate pressures and temperatures applicable to calculations of hydrothermal boiling. Geochimica et Cosmochimica Acta 52, 739–749. doi:10.1016/0016-7037(88)90334-1

Teatini, P., Gambolati, G., Ferronato, M., Settari, a. (Tony), Walters, D., 2011. Land uplift due to subsurface fluid injection. Journal of Geodynamics 51, 1–16. doi:10.1016/j.jog.2010.06.001

Thomas, H.R., King, S.D., 1994. A non-linear, two-dimensional, potential-based analysis of coupled heat and mass transfer in a porous medium. International Journal for Numerical Methods in Engineering 37, 3707–3722. doi:10.1002/nme.1620372108

Trémosa, J., Castillo, C., Vong, C.Q., Kervévan, C., Lassin, A., Audigane, P., 2014. Long-term assessment of geochemical reactivity of CO2 storage in highly saline aquifers: Application to Ketzin, In Salah and Snøhvit storage sites. International Journal of Greenhouse Gas Control 20, 2–26. doi:10.1016/j.ijggc.2013.10.022

van Genuchten, M.T., 1980. A Closed-form Equation for Predicting the Hydraulic Conductivity of Unsaturated Soils1. Soil Science Society of America Journal 44, 892. doi:10.2136/sssaj1980.03615995004400050002x

Vasco, D.W., Ferretti, A., Novali, F., 2008. Reservoir monitoring and characterization using satellite geodetic data: Interferometric synthetic aperture radar observations from the Krechba field, Algeria. Geophysics 73, WA113–WA122. doi:10.1190/1.2981184

Verdon, J.P., Kendall, J.-M., White, D.J., Angus, D. a., 2011. Linking microseismic event observations with geomechanical models to minimise the risks of storing CO2 in

geological formations. Earth and Planetary Science Letters 305, 143–152. doi:10.1016/j.epsl.2011.02.048

Vidal-gilbert, S., Nauroy, J., Brosse, E., 2009. 3D geomechanical modelling for CO 2 geologic storage in the Dogger carbonates of the Paris Basin. International Journal of Greenhouse Gas Control 3, 288–299. doi:10.1016/j.ijggc.2008.10.004

Vidal-Gilbert, S., Tenthorey, E., Dewhurst, D., Ennis-King, J., Van Ruth, P., Hillis, R., 2010. Geomechanical analysis of the Naylor Field, Otway Basin, Australia: Implications for CO2 injection and storage. International Journal of Greenhouse Gas Control 4, 827–839. doi:10.1016/j.ijggc.2010.06.001

Vilarrasa, V., 2014. Impact of CO2 injection through horizontal and vertical wells on the caprock mechanical stability. International Journal of Rock Mechanics and Mining Sciences 66, 151–159. doi:10.1016/j.ijrmms.2014.01.001

Vilarrasa, V., Bolster, D., Dentz, M., Olivella, S., Carrera, J., 2010a. Effects of CO2 Compressibility on CO2 Storage in Deep Saline Aquifers. Transport in Porous Media 85, 619–639. doi:10.1007/s11242-010-9582-z

Vilarrasa, V., Bolster, D., Olivella, S., Carrera, J., 2010b. Coupled hydromechanical modeling of CO2 sequestration in deep saline aquifers. International Journal of Greenhouse Gas Control 4, 910–919. doi:10.1016/j.ijggc.2010.06.006

Vilarrasa, V., Carrera, J., 2015. Geologic carbon storage is unlikely to trigger large earthquakes and reactivate faults through which CO2 could leak. Proceedings of the National Academy of Sciences of the United States of America 112, 5938–5943. doi:10.1073/pnas.1413284112

Vilarrasa, V., Olivella, S., Carrera, J., Rutqvist, J., 2014. Long term impacts of cold CO2 injection on the caprock integrity. International Journal of Greenhouse Gas Control 24, 1–13. doi:10.1016/j.ijggc.2014.02.016

Vilarrasa, V., Rutqvist, J., Rinaldi, A.P., 2015. Thermal and capillary effects on the caprock mechanical stability at In Salah, Algeria. Greenhouse Gases: Science and Technology n/a–n/a. doi:10.1002/ghg.1486

Vilarrasa, V., Silva, O., Carrera, J., Olivella, S., 2013. Liquid CO2 injection for geological storage in deep saline aquifers. International Journal of Greenhouse Gas Control 14, 84–96. doi:10.1016/j.ijggc.2013.01.015

Waples, D.W., Waples, J.S., 2004. A Review and Evaluation of Specific Heat Capacities of Rocks, Minerals, and Subsurface Fluids. Part 2: Fluids and Porous Rocks. Natural Resources Research 13, 123–130. doi:10.1023/B:NARR.0000032648.15016.49

White, J.C., Williams, G.A., Grude, S., Chadwick, R.A., 2015. Utilizing spectral decomposition to determine the distribution of injected CO 2 at the Snøhvit Field. Geophysical Prospecting 63, 1213–1223. doi:10.1111/1365-2478.12217

Wilson, J. V., 1973. Approximations for physical properties of sea salt solutions. Oak Ridge, Tennessee.

Xu, T., Apps, J.A., Pruess, K., 2004. Numerical simulation of CO2 disposal by mineral trapping in deep aquifers. Applied Geochemistry 19, 917–936. doi:10.1016/j.apgeochem.2003.11.003

Zeidouni, M., Pooladi-Darvish, M., Keith, D., 2009. Analytical solution to evaluate salt precipitation during CO2 injection in saline aquifers. International Journal of Greenhouse Gas Control 3, 600–611. doi:10.1016/j.ijggc.2009.04.004

Zhou, Q., Birkholzer, J.T., Tsang, C.-F., Rutqvist, J., 2008. A method for quick assessment of CO2 storage capacity in closed and semi-closed saline formations. International Journal of Greenhouse Gas Control 2, 626–639. doi:10.1016/j.ijggc.2008.02.004

Zoback, M.D., Gorelick, S.M., 2012. Earthquake triggering and large-scale geologic storage of carbon dioxide. Proceedings of the National Academy of Sciences of the United States of America 109, 10164–8. doi:10.1073/pnas.1202473109

8 Appendices

8.1 Equation of State of Peng and Robinson

The properties of gases and liquids strongly depend on the environmental pressure and temperature conditions. The equation of state developed by Peng and Robinson (1976) is used to describe the relationship of the volume V, pressure P and temperature T of real fluids as presented in the following:

$$P = \frac{RT}{V-b} - \frac{a}{V\left(V+b\right)+b\left(V-b\right)} \tag{8.1}$$

where

R	universal gas constant
a	$a_c\,\alpha$
α	$\left[1+\kappa\left(1-\sqrt{T/T_c}\right)\right]$
a_c	$0.457235\,R^2T_c^2/P_c$
κ	$0.37464 + 1.54226\omega - 0.26992\omega^2$ if $\omega \leq 0.49$
κ	$0.379642 + 1.48503\omega - 0.164423\omega^2 + 0.016666\omega^3$ if $\omega > 0.49$
ω	pitzer acentric factor
P_c	critical pressure
T_c	critical temperature

Eq. (8.1) can be rewritten in a cubic polynomial form for the compressibility Z as

$$Z^3 - \left(1-B\right)Z^2 + \left(A - 3B^2 - 2B\right)Z - \left(AB - B^2 - B^3\right) = 0 \tag{8.2}$$

where

$$\begin{aligned} A &= \frac{aP}{R^2T^2} \\ B &= \frac{bP}{RT} \\ Z &= \frac{PV}{RT} \end{aligned} \tag{8.3}$$

The solution to the cubic equation Eq. (8.2) yields one or three real roots for the compressibility factor Z, depending on the number of phases in the system. The largest root is for the compressibility Z of the gaseous phase, whereas the smallest positive root corresponds to that of the liquid in a two-phase system. The Peng and Robinson equation of state can be applied to fluids such as carbon dioxide, ethane, methane and water by

adopting the corresponding parameters to the formula. Table 8.1 shows the pitzer acentric factor and the critical state variables for different real fluids.

Table 8.1 Fluid properties used in the Peng and Robinson equation of state.

Fluid substance	ω [-]	P_c [MPa]	T_c [T]
Carbon dioxide CO_2	0.239	7.39	304.25
Water H_2O	0.344	22	647.10
Ethane C_2H_6	0.099	4.87	305.32
Methane CH_4	0.011	4.60	190.56

8.2 CO_2 Density and fugacity

The density of CO_2 can be determined as

$$\rho_c = \frac{1}{Z}\frac{M_c}{R}\frac{P}{T} \tag{8.4}$$

where M_c (0.04401 kg/mol) is the molar weight of CO_2. The compressibility factor Z is calculated according to Eq.(8.2).

The fugacity f of a real fluid represents the effective pressure in the chemical equilibrium calculation, such as CO_2 dissolution in water. The fugacity can be consider as the equivalent ideal gas pressure that has the same chemical potential as the real gas, defined as

$$f = \Phi P \tag{8.5}$$

where the fugacity coefficient Φ relates the ideal gas pressure P and fugacity f and can be determined from the Peng and Robinson EOS:

$$\ln\Phi = (Z-1) - \ln(Z-B) - \frac{A}{2\sqrt{2}B}\left[\frac{Z+(\sqrt{2}+1)B}{Z+(1-\sqrt{2})B}\right] \tag{8.6}$$

If an ideal gas condition is of interest, the fugacity coefficient Φ=1 is generally used. When the environmental pressure is higher (>0.1MPa), the deviation between the fugacity and ideal gas pressure increases. To provide an example, the fugacity coefficient of CO_2 for a pressure of 20MPa and temperature of 60°C is equal to 0.5, which means that a 50% CO_2 dissolution quantity will be overestimated when using the mechanical pressure P in the calculation.

Curriculum Vitae

CHAO LI

Chinese, born 21.10.1987

Rue de Bassenges, 2
1024 Ecublens VD, Switzerland
Mobile : +41 78 728 2105
E-mail : chao.li@epfl.ch

EDUCATION

2012-*present*	Thesis title: "Geomechanical modelling of CO_2 injection in deep aquifers" Ecole Polytechnique Fédérale de Lausanne (EPFL) - Soil Mechanics Laboratory (LMS) Supervisor: Prof. L. Laloui
2011	Engineer diploma (M.Sc.) Institut National des Sciences Appliquées (INSA) de Rouen, France
03-06.2011	Master thesis, LMS-EPFL: "Study of the possible seismically triggered landslide in the region of Valley, Switzerland"
2010-2011	Erasmus European Exchange Program in EPFL Specialization in geotechnical engineering and construction of infrastructure
2007-2011	Undergraduate student at INSA de Rouen, France - English-French bilingual science section and Department of Civil Engineering and Sustainable Construction

PROFESSIONAL EXPERIENCE

05.2014	Co-lecturer - 2 Day short course "Shale for unconventional energy & CO_2 sequestration" at SINOPEC, China.
2011	Research engineer on energy geostructure and nuclear waste storage at Ecole Polytechnique Fédérale de Lausanne (EPFL) - Soil Mechanics Laboratory (LMS)
06-08.2010	Risk management training period at 'Marine Construction' SOCOTEC International, France
07-08.2009	Airport roadway assessment training period at Rincent BTP, France

LANGUAGES

Chinese	Mother tongue
French	Fluent (working language)
English	Fluent (TOEIC 935 & working language)
German	Level A1

COMPUTER TOOLS

Programming	C/C++, Fortran, Visual Basic, Matlab
Modelling	Plaxis, Zsoil, Audocad, Gefdyn, Lagamine, GID, Gmsh
Operation	Microsoft Office, Adobe Photoshop, Illustrator, Indesign, Première

SCIENTIFIC PUBLICATIONS

C. Li and L. Laloui. Coupled multiphase thermo-hydro-mechanical analysis of supercritical CO_2 injection: benchmark for the In Salah surface uplift problem. *International Journal of Greenhouse Gas Control,* 2016. (accepted with revision)

L. Laloui, A. Ferrari, **C. Li** and J. Eichenberger. Hydro-mechanical analysis of volcanic ash slopes during rainfall. 66, 3, 220-231, *Géotechnique*, 2015.

C. Li, P. Barès and L. Laloui. A hydromechanical approach to assess CO_2 injection-induced surface uplift and caprock deflection. *Geomechanics for Energy and the Environment*, 4, 51-60, 2015.

L. Laloui and **C. Li**. Carbon dioxide injection into deep aquifers: a geomechanical perspective. *Computer Methods and Recent Advances in Geomechanics.* 45-50, 2015

C. Li and L. Laloui. Coupled approach to assess caprock deformation caused by CO_2 injection. *Soil Behavior and Geomechanics*, 651-657, 2014

L. Laloui and **C. Li**. Hydromechanical coupling in CO_2 geological injection processes. *Proceedings of the Seventh International Congress on Environmental Geotechnics, Melbourne, Australia*, *Melbourne*, 43-51, 2014.

F. Dupray, **C. Li**, M. Baehler, C. Schurmann, L. Laloui. Utilisation des geostructures énergétiques pour la régulation thermique et l'optimisation énergétique des infrastructures routières et ouvrages d'art. DETEC Report 1468, 2014

F. Dupray, **C. Li** and L. Laloui. Heat-exchanger piles for the de-icing of bridges. *Acta Geotechnica*, 9, 413-423, 2014.

F. Dupray, **C. Li** and L. Laloui. THM coupling sensitivity analysis in geological nuclear waste storage. *Engineering Geology*, 163, 113-121, 2013.

C. Li, B. Paul and L. Laloui. Coupled semi-analytical solution for CO_2 injection-induced surface uplift and caprock deflection. *Proceedings of the 47th US Rock Mechanics/Geomechanics Symposium.* 2013

F. Dupray, **C. Li** and L. Laloui. Significance of rock THM parameters in geological nuclear waste storage simulation. *Proceedings of the 47th US Rock Mechanics/Geomechanics Symposium.* 2013

INVITED SEMINARS

Atelier - CO2 utilisation "Les enjeux géomécanique de la séquestration du CO_2", Lausanne, Switzerland, April 2016

Geothermal Friday Seminar, ETH Zurich "Carbon dioxide injection into deep aquifers: a geomechanical perspective", Zurich, Switzerland, March 2015